POLY(3-METHYLTHIOPHENE) BRUSHES: STRUCTURE, MORPHOLOGY, AND ELECTRONIC TRANSPORT

Mark Moog

A dissertation submitted to the faculty at the University of North Carolina at Chapel Hill in partial fulfillment of the requirements for the degree of Doctor of Philosophy in the Department of Physics.

Chapel Hill
2018

Approved by:

Frank Tsui

Wei You

Sean Washburn

Joaquin Drut

Jianping Lu

ABSTRACT

Mark Moog: POLY(3-METHYLTHIOPHENE) BRUSHES: Structure, Morphology, and Electronic Transport
(Under the direction of Frank Tsui)

Low charge carrier mobility is a major obstacle that limits the performance of organic electronic devices. For conjugated polymers, increasing the contribution from intramolecular charge transport channels to overall charge transport is expected to increase the mobility of the overall device. This is because the transport of charge carriers along conjugated polymer backbones is expected to be much faster than transport between the polymers. However, designing devices that take advantage of intramolecular charge transport has proven difficult, and in virtually all organic electronic devices charge must travel not only along individual polymer backbones, but must hop inefficiently between polymers as well due to film morphology.

Conjugated polymer brushes are films comprising densely packed conjugated polymers that are tethered to a substrate, causing the polymers to elongate creating a brush-like morphology. Due to their morphology, polymer brush devices are expected to exhibit enhanced intramolecular charge transport. Electronic devices can be made from polymer brush films by growing the polymer from a conducting substrate and attaching a metal electrode to the top of the brush film, forming the vertical electrode-polymer-electrode structure. These devices make it possible to investigate intramolecular charge transport processes, because each polymer which contacts the top electrode is also contacting the bottom electrode (i.e. the substrate).

Polythiophene is a model conjugated polymer that has received extensive research interest as an active layer in organic electronic devices due to their electronic properties and envi-

ronmental and thermal stability. In this work the morphology and electronic properties of poly(3-methylthiophene) (P3MT) brushes are studied using the vertical electrode-polymer-electrode devices. The bulk resistivity of P3MT brush devices was found to be $1.4 * 10^5 \Omega$-cm, two orders of magnitude lower than that of spun cast films of comparable polythiophene films. The resistivity of the brush films has been analyzed on a per-molecule basis, and the resulting "molecular resistivity" value of 180 GΩ/nm is comparable to those obtained from transport studies of molecular wires. The significantly reduced bulk resistivity along with a molecular resistivity on par with molecular wires indicate an enhanced contribution from intramolecular charge transport in conjugated polymer brush devices.

ACKNOWLEDGMENTS

This dissertation is the culmination of years of hard work, not just by me, but by many others as well. In particular, Ian VonWald and Travis LaJoie of the You group at UNC played essential roles in my graduate student career studying polymer brushes. Without their expertise in polymer brush synthesis this work would not have been possible. They have spent countless hours synthesizing brushes and produced hundreds of samples for electronic and morphological characterization. I cannot thank them enough. In addition to Ian and Travis, I would like to thank my advisor, Dr. Frank Tsui, who has guided me through my graduate school career.

TABLE OF CONTENTS

LIST OF TABLES

LIST OF FIGURES

LIST OF ABBREVIATIONS AND SYMBOLS

AFM	Atomic Force Microscopy
cAFM	Conducting Atomic Force Microscopy
CP	Conducting Polymer
CPB	Conjugated Polymer Brush
FWHM	Full-Width-at-Half-Maximum
GIWAXS	Grazing Incidence Wide Angle X-ray Scattering
HOMO	Highest Occupied Molecular Orbital
ILC	Injection Limited Current
ITO	Indium Tin Oxide
IV	Current-Voltage (i.e. current-voltage measurements)
KTP	Kinetic Transfer Printing
LUMO	Lowest Unoccupied Molecular Orbital
μ	Charge Carrier Mobility
MMM	Metal-Molecule-Metal (i.e. metal-molecule-metal junctions)
OSC	Organic Semiconductor
P3AT	Poly(alkylthiophene)
P3MT	Poly(3-methylthiophene)
P3HT	Poly(3-hexylthiophene)
RBS	Rutherford Backscattering Spectroscopy
SAM	Self-assembled Monolayer
SI-KCTP	Surface Initiated Kumada Catalyst Transfer Process
SCLC	Space-charge Limited Current

STM	Scanning Tunneling Microscopy
UPS	Ultraviolet Photoelectron Spectroscopy

CHAPTER 1: INTRODUCTION

On October 10, 2000 the Royal Swedish Academy of Sciences awarded the Nobel prize in Chemistry to Alan J. Heeger, Alan G. MacDiarmid and Hideki Shirakawa for their work in the 1970s on "the discovery and development of conductive polymers."[1] Upon their discovery conducting polymers became an intriguing alternative to traditional inorganic wafer-based technologies which form the bedrock of modern electronics. Conducting polymers belong to a larger class of materials called organic semiconductors (OSCs), which include all carbon based semiconducting molecules and materials. Since the 1970s, researchers have improved the processability, stability, and performance of OSC devices, and worked towards understanding the fundamental mechanisms governing the electronic properties of OSCs. Today, after decades of progress, OSCs see wide commercial use in phone screens and other displays due to their light weight, cheap fabrication, low power usage and potential for high contrast ratios. OSCs have many intriguing properties that distinguish them from inorganic counterparts, which have made them attractive candidates for applications, including transistors, solar cells, and radio-frequency identification devices. Due to both their already realized and potential applications, the global market for organic electronics is expected to grow upwards of $80 billion by 2020.[2]

While OSCs offer many advantages over traditional inorganic materials, and the commercial use of OSC devices continues to grow, commercial applications for OSCs are currently limited.[3] OSC devices tend to have lower charge carrier mobilities than their inorganic counterparts. High mobility is essential to the performance of many electronic devices such as transistors and photovoltaics, and increasing the mobility of these devices is a key objective of the field.[4] Understanding the processes that control charge transport, and therefore device mobility, is essential for future higher performance devices.[5]

Section 1.1: Review of Essential Chemistry

1.1.1: Molecular Orbitals and Conjugation

When atoms come together to form molecules, the electron orbitals of adjacent atoms interact, resulting in new orbitals with different energies and shapes than the atomic orbitals of the constituents. These new orbitals are called molecular orbitals, and are often interpreted as atoms 'sharing' electrons or as bonds which hold the atoms in a molecule together. These orbitals give rise to many of the optical and electronic properties of molecules, and the orbitals which contribute the most to the electronic properties of molecules are the highest occupied molecular orbital (HOMO) and the lowest unoccupied molecular orbital (LUMO). These orbitals correspond to the highest electron energy level that is occupied in the molecule's ground state and the lowest electron energy level that is unoccupied in the molecule's ground state respectively, and are analogous to the conduction and valance bands in crystalline solids.

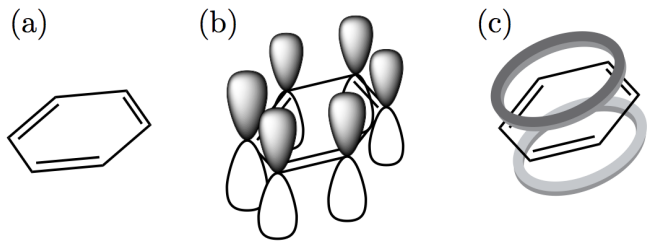

Figure 1.1: Multiple versions of benzene's structural formula are shown. π delocalization occurs along the benzene ring and is indicated by alternating single and double bonds. (a) Benzene's structural formula. (b) The p orbitals of individual carbon atoms in the benzene before they form into delocalized π orbitals. (c) π orbitals resulting from p orbital overlap in benzene.

Molecular orbitals are classified as either σ orbitals or π orbitals (also called σ or π bonds). σ bonds are formed by two adjacent s atomic orbitals, and are localized to the space directly between adjacent atoms. π orbitals are formed by adjacent interacting coplanar p orbitals (and sometimes d orbitals). While σ orbitals involve only two adjacent atoms in a molecule, π orbitals can involve multiple adjacent atoms, resulting in a delocalize orbital

spanning multiple nuclei within the molecule (Figure 1.1). In organic materials π orbitals tend to be higher energy than σ orbitals,[5] and therefore, in conjugated organic materials the HOMO and LUMO levels are often π orbitals.

Figure 1.1 shows the origin of delocalized π orbitals in benzene. These orbitals are delocalized across the entire benzene ring. In structural formulas the presence of π orbitals is indicated by the alternating single and double bonds, as can be seen in the benzene ring. Molecules which form delocalized π orbitals are called conjugated molecules.

1.1.2: Polymers

Polymers are a diverse group of molecules, which display many different mechanical, chemical, and electronic properties, making them a versatile class of materials. For example, DNA and proteins are polymers. Plastic and rubber are made of polymers. Scotch tape's stickiness and Teflon's smoothness both come from the polymers they comprise. The versatility of polymers is further augmented by their tunability, e.g. molecular side chains can be added to a polymer backbone to give the polymer new functionalities (Figure 1.3). A polymer's properties can also be adjusted by adding chemical groups to the polymer molecule through a process called functionalization, e.g. adding chemical groups that contain ferromagnetic metals to allow stronger interaction with magnetic fields. Due to their incredible versatility, low cost, and processability, polymers have become ubiquitous in our society.

Polymers are molecules formed out of smaller molecular units, called repeat units or monomers (Figure 1.2). Monomers are chemically bound together to form larger polymer molecules. The number of monomers which form a polymer is called the degree of polymerization, and can be controlled during polymer synthesis, allowing the molecular weight of the resulting polymer molecule to be tuned. The molecular weight of a polymer can have a large effect on its mechanical, chemical and electronic properties.[7] Polymers with few monomers are called called oligomers, and have names indicating the number of monomers they contain: dimers contain two monomers, trimers contain three, etc. This naming convention is

not used for all polymers, however, as polymers can contain millions of monomers.

Polymers do not generally form rigid, straight structures. Though small polymers tend to behave like rigid rods, above a certain length a polymer's shape, also known as its conformation, becomes non-linear (Figure 1.4). For the theoretical ideal polymer, conformation is modeled as a three dimensional random walk.[8] The length scale on which the polymer maintains its tangent orientation is called the persistence length.[9] Polymers with longer persistence length have higher rigidity. Conformation can have a large impact on the mechanical, electrical and chemical properties of a polymer and polymer materials, and so controlling polymer conformation is desirable.[10]

A polymer's size can be described in multiple ways, the most common being degree of polymerization, molecular weight, contour length, and radius of gyration. The contour length of a polymer describes the distance traced out by the polymer's backbone and is directly proportional to the number of monomers in the polymer. Degree of polymerization, molecular weight, and contour length are equivalent in that they describe the amount of material in the polymer, but do not contain any information about the polymer's spatial extent or conformation. The radius of gyration is the root mean square distance of the polymer from its center of mass, and therefore contains information about both the number of monomers in the polymer and its conformation. Since the conformation of large polymers tend to behave like a random walk, the contour length is generally much larger than any one dimension of the volume enclosing the polymer.

1.1.3: Organic Semiconductors

Organic semiconductors (OSCs) encompass a wide variety of organic materials that display semiconducting behavior. Until the mid 1900s, organic materials were mostly considered insulators, and not viewed as viable semiconducting or conducting materials. In the 1950s and '60s, high conductivity was observed in crystals made of small organic molecules (organic crystals) when a sufficient number of charge carriers were injected into the crystal from

electrodes.[12] Building on the semiconducting properties of organic crystals, a new class of OSCs were discovered in the 1970s: conducting polymers. Small molecules and conducting polymers each have their own advantages as active materials in electronic devices. Conducting polymers offer better flexibility and solution processability, while small molecules offer high crystallinity.

Conductivity (σ) is a property of materials that relates the current density (J) produced within a material to the electric field (E) is applied to the material. Conductivity is given by

$$J = \sigma E, \tag{1.1}$$

$$\sigma = ne\mu, \tag{1.2}$$

where n is carrier concentration of the material, e is the elementary charge, and μ is the charge carrier mobility. Mobility is discussed further in section 1.2.2. Based on their conductivity, materials fall into one of three general categories: insulators, semiconductors and conductors. Insulators are materials with low conductivity, conductors are materials with high conductivity, i.e. metals, and semiconductors for materials which fall in between. Semiconductors and conductors are used to build a wide array of circuit elements in electronic devices, and OSCs and conducting polymers fall into either the semiconducting and conducting ranges (Table 1.1).

Table 1.1: Conductivities of select materials

Material	conductivity ($\Omega^{-1}\text{cm}^{-1}$)
Metals	$\geq 10^5$
Stretch oriented doped polyacetylene	10^5
Doped polyacetylene	10^3 to 10^5
Undoped polyacetylene	10^{-5}
Insulators	$\leq 10^{-8}$
Teflon	10^{-20}

Conducting polymers are conjugated. In 1949 Kuhn showed that the energy level of π orbitals in conjugated polymers could be determined by modeling conjugated polymers as

one dimensional periodically repeating potentials.[13] Kuhn's model for conjugated polymers draws a parallel to the periodic crystal lattice which gives rise to electronic band structure in solids. Since their discovery in the 1970s, it has been assumed that the delocalized π orbitals along the backbone of conjugated polymers should behave similarly to energy bands in crystalline materials, and result in band-like charge transport along the conjugated polymer backbone.[14]

Conjugation alone is not enough for polymers to conduct, the polymer's carrier concentration needs to be high as well. The intrinsic carrier concentration in undoped polymers (n_i) is given by

$$n_i = N_0 exp(-\frac{E_g}{2kT}), \tag{1.3}$$

where E_g, the energy difference between HOMO and LUMO levels, N_0 is the density of transport states, T is the temperature and k is the Boltzmann constant.[5] Larger band gaps result in lower intrinsic carrier concentration due to the exponentially decreasing probability of electrons thermal excitation from the HOMO to LUMO states as the gap grows larger. Adding a small amount of dopant can greatly increase the carrier concentration of polymer material, similar to doping inorganic semiconductors.[15] Dopants in conducting polymers work by oxidizing or reducing the polymer, adding or removing electrons from its HOMO or LUMO levels.[15] Carrier concentration can also be increased by injecting charge into the OSC from an electrode,[5] or through photogeneration.[16] Atmospheric doping is prevalent in many OSCs where exposure to atmosphere allows oxygen and water to permeate the material, resulting in oxidation or reduction of molecules within.[17]

Adding or removing a charge from a molecule can cause a local change in the molecule's conformation.[5] When a charge moves through a polymer, or between polymers, this local deformation moves with it. The charge carrier and the local deformation around it are often modeled as a quasi-particle called a polaron,[5] which behaves much like an electron or hole but has a higher effective mass due to interacting with the local 'lattice'.

The conformation of conducting polymers can have an impact on their conductivity.[18] π conjugation occurs due to the planar nature of monomers in the polymer. If monomers lie in the same plane, their p-orbitals can overlap and delocalized π-orbitals can form. Torsion defects in longer polymers can cause breaks in the coplanarity of monomers and therefore delocalized π orbitals tend not to extend along the entirety of the conjugated polymer backbone. Instead, the polymer is segmented into discrete conjugated sections, each with its own delocalized π-orbitals. The size of these segments is called the conjugation length of the polymer. Increasing conjugation length leads to an increase in the conductivity of conjugated polymers[19], likely due to longer conjugation lengths resulting in smaller band gaps and larger stretches of delocalization. Stretch oriented polymers, where the polymer's conformation has been altered by stretching a bulk polymer film along one axis, have shown some of the highest conducting polymer conductivities.[20]

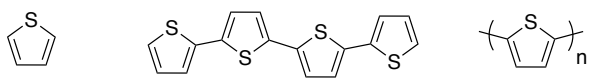

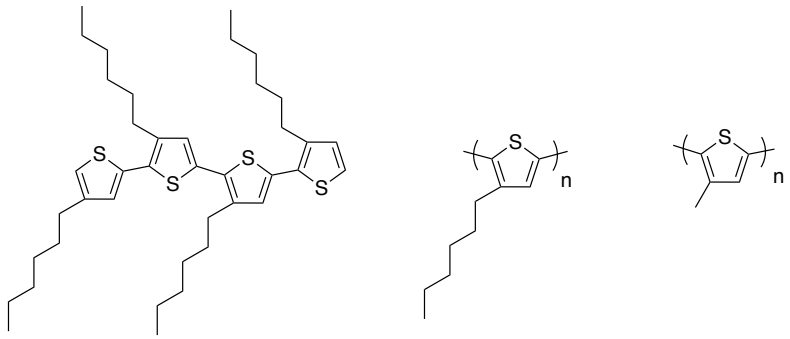

Figure 1.2: (a) A thiophene monomer. (b) A thiophene oligomer, containing four monomers (tetrathiophene). (c) A polythiophene polymer, containing n monomers.

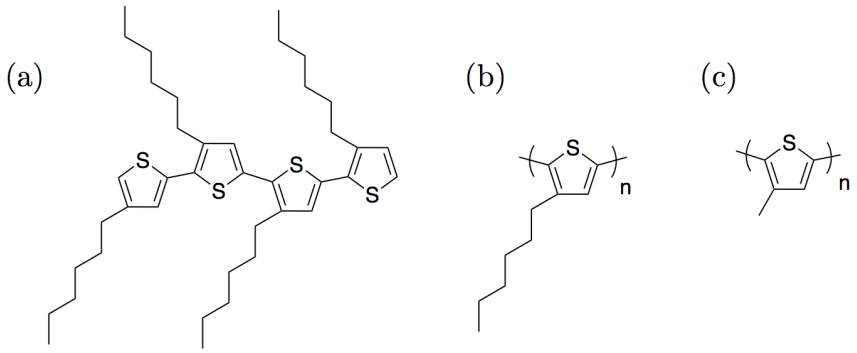

Figure 1.3: Polythiophene can be modified with the addition of side chains. (a) Poly(3-hexylthiophene) (P3HT) tetramer, a polytiophene derivative with a hexyl group attached to each monomer. The alternating side chain placement is called regioregularity. The large hexyl side chains result in an increase in solubility.[6] (b) P3HT polymer. (c) Poly(3-methylthiophene) (P3MT), a polythiophene derivative with a methyl group attached to each monomer. Smaller side chains allow denser packing of the polymer, but reduces solubility.

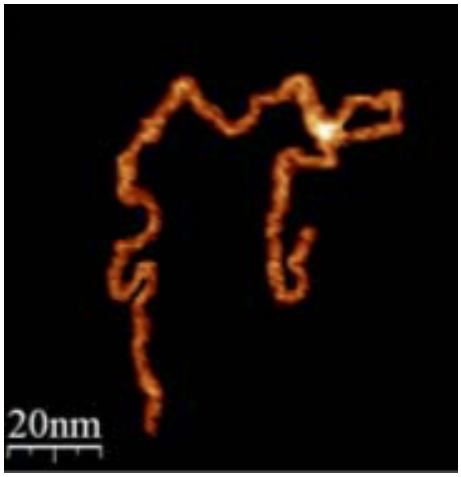

Figure 1.4: An AFM image of poly(2-vinylpyridine). Figure S2 in Ref [11], reproduced with permission.

Section 1.2: Organic Electronics

1.2.1: A Brief History and Overview of Organic Electronics

The field of organic electronics encompasses the study of films consisting of conjugated polymers or small organic molecules. In devices, film thickness is generally much greater than the length of the individual molecules within the bulk, so the study of organic electronics is focused on the bulk properties of OSCs and less focused on the properties of individual molecules. The morphology of organic electronic films range from isotropic and amorphous to oriented and crystalline. Due to their wide range of realized and potential uses, organic electronics continue to attract academic and commercial interests.

The first conducting organic material was discovered by Henry Letheby in 1862, and called the "blue substance."[21] The blue substance was later found to be a polymer, polyaniline, but in 1862 the concept of polymers would not be developed for over half a century. Organic electronic devices were first studied in the 1950s. These devices were crystals made of small organic molecules, and demonstrated the feasibility of organic materials as active elements in electronic devices. Conjugated polymers were discovered in the 1970s, introducing a new class of OSCs that allowed for solution processing and greater flexibility for fabricating organic electronic devices. By the late 1980s, the first practical OLEDs were made,[22] paving the way for future commercialization of organic electronics (Figure 1.5). The first OFETs were reported in the 1980s as well, utilizing polythiophene as the active semiconducting material in a traditional thin film field effect transistor (TFT) geometry (Figure 1.5).[23] While OLEDs matured over the following decades into a commercialized technology that now sees widespread use, OFETs are still an academic research topic and have not yet achieved commercial use. The first organic photovoltaics (OPV) were made in the mid 1990s, initially achieving efficiencies of only $\sim 3\%$ (Figure 1.5).[24] OPVs continue to be an active area of research, offering potentially cheaper solar cells than inorganic counterparts.

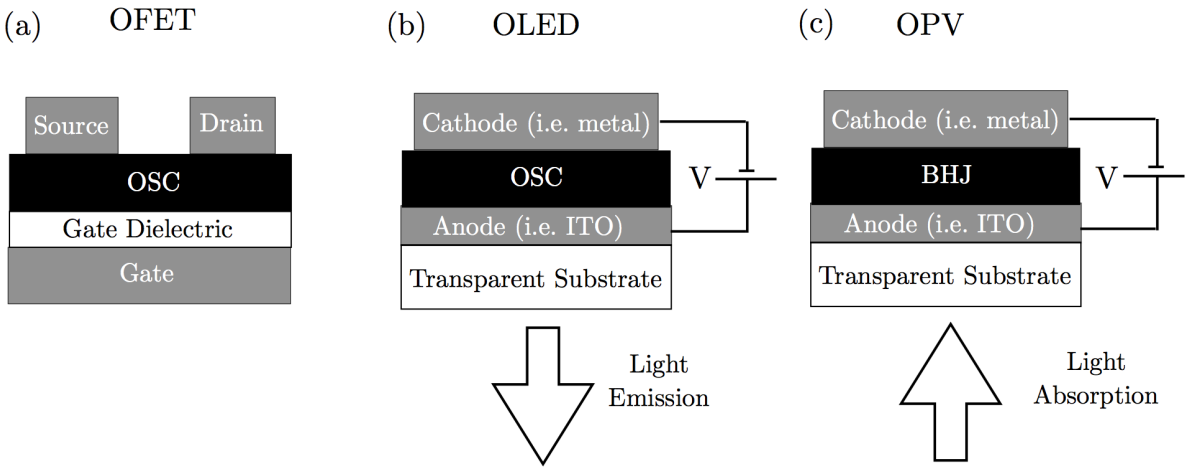

Figure 1.5: (a) OFETs function identically to traditional TFTs. In OFETs the inorganic semiconductor has been replaced by an organic semiconductor. The low mobility of organic semiconductors makes the switching speed of OFETs much slower than traditional transistors. (b) A simple OLED is constructed by placing an an emitting active layer between two electrodes. By applying a bias across the active layer, holes and electrons are injected by the cathode and anode which recombine within the film and emit photons. (c) Photovoltaics operate on very similar principles as OLEDs, except they absorb light rather than emit it. A bias is applied creating an electric field across the active layer. Then when an incoming photon can excite an electron in the active layer from the HOMO to the LUMO creating an electron-hole pair. The electron and hole are drawn to opposite electrodes due to the electric field, and create a current. High mobility helps prevent the electron and hole from recombining within the active layer. The most common design for OPVs uses a bulk heterojunction as the active layer. In BHJ two conducting polymers are used, one which accepts electrons and on one which donates electrons, called the donor and accepter. The electrons travel to the electrode through the acceptor and the holes travel through the donor.

1.2.2: Charge Transport and Mobility in Organic Semiconductors

Mobility relates the drift velocity of charge carriers within a material to the electric field applied to the material. Holes and electrons can have different mobilities within the same material. When considering multiple charge carriers, the relationship between mobility, electric field and current density is given by

$$J = \rho_e \mu_e E + \rho_h \mu_h E, \tag{1.4}$$

where ρ is the charge carrier density of electrons and holes, μ is the mobility of electrons

and holes, and E is the applied field. Since the intrinsic carrier concentration for OSCs are very low, in many devices extrinsic charge carriers are injected from electrodes to increase carrier concentration.[5] In these devices carrier concentrations are largely controlled by the electrode-OSC interface.[25] In order to simplify the interpretation of electronic measurements, electrodes are often selected such that unipolar transport occurs, where one charge carrier has a significantly higher concentration than the other. Interfaces are described in more detail in section 1.2.3. By allowing one predominant charge carrier, the relationship between current density, electric field, and mobility can be expressed using equations 1.1 and 1.2. Though the SI units for mobility are m^2/V-s, mobility is conventionally measured in units of cm^2/V-s.[25]

Charge carrier mobility is the natural benchmark for describing and comparing organic electronic materials.[3,26–28] In many active devices such as OPVs and OFETs, high mobility is essential for device performance. A driving force of the field is to find materials and build devices with mobilities approaching their inorganic counterparts. A comparison of mobility for select organic and inorganic semiconductors is shown in Table 1.2.

Table 1.2: Mobilities of select materials

Material	Mobility $\mu(\frac{cm^2}{V-s})$
Single crystal Si	450 (hole) to 1400 (electron)
Highest mobility organic single crystal devices[29]	40
Amorphous Si	1
Highest mobility CP devices[29]	~ 10
Spuncast Poly(3-methylthiophene)[17]	0.004

Organic electronic devices can often have performance reproducibility issues due to device-to-device morphological fluctuations[30,31] and sensitivity to fabrication and post treatment procedures.[31] Different measurement techniques used on the same device can also produce drastically different mobilities, and the same data can result in very different extracted mobilities depending on who is analyzing the data.[32] Despite this, mobility remains an essential benchmark for the field, and understanding the mechanisms underlying charge

transport in organic electronic devices is essential for building high performance devices.

In organic electronic films, transport occurs not only along the backbone of individual polymer chains (intramolecular) but also between polymers (intermolecular) (Figure 1.6). Transport is a combination of band like drift through conjugated segments of polymer backbone interspersed with hopping between conjugated segments both along a single polymer, and between adjacent polymers.[33] Hopping between polymers typically occurs through π-stacks (Figure 1.6).[25] π stacking is the result of attractive interactions between π orbitals on aromatic rings which cause them to align (Figure 1.6). π stacking can occur in films made of polymers which contain conjugated aromatic rings, such as polythiophene. Hopping typically refers to a thermally activated process, characterized by an activation energy, where charges are excited over a potential barrier separating molecular orbitals.

Both experimental and theoretical reports show that increased intramolecular transport results in increased bulk mobility in organic electronic devices.[34–36] The mobility of intramolecular charge transport through conjugated segments on ordered polymer chains is expected to be on the order of a few hundred $\frac{\text{cm}^2}{\text{V-s}}$), but these mobilities have not been observed due to the inherent disorder in conducting polymer films.[37] In particular, device geometry often necessitates intermolecular charge transport and charge transport across grain boundaries, which are both significantly slower than intramolecular transport.[37] Additionally, disorders in films can limit the conjugation length of conducting polymers, creating additional transport barriers.[37] Designing devices to take advantage of the intramolecular transport in order to achieve higher mobility is a common practice.

Directly probing mobility requires transient measurement techniques that often require specialized instrumentation such as extremely high gain-bandwidth product amplifiers to detect small and fast signals, or restrictive device and material properties, such as minimum device thicknesses, or materials with conductivities that meet certain thresholds.[32] Since direct mobility measurements are difficult and not possible for all materials and device geometries, mobility is often extracted from current-voltage (IV) measurements.[32] In these

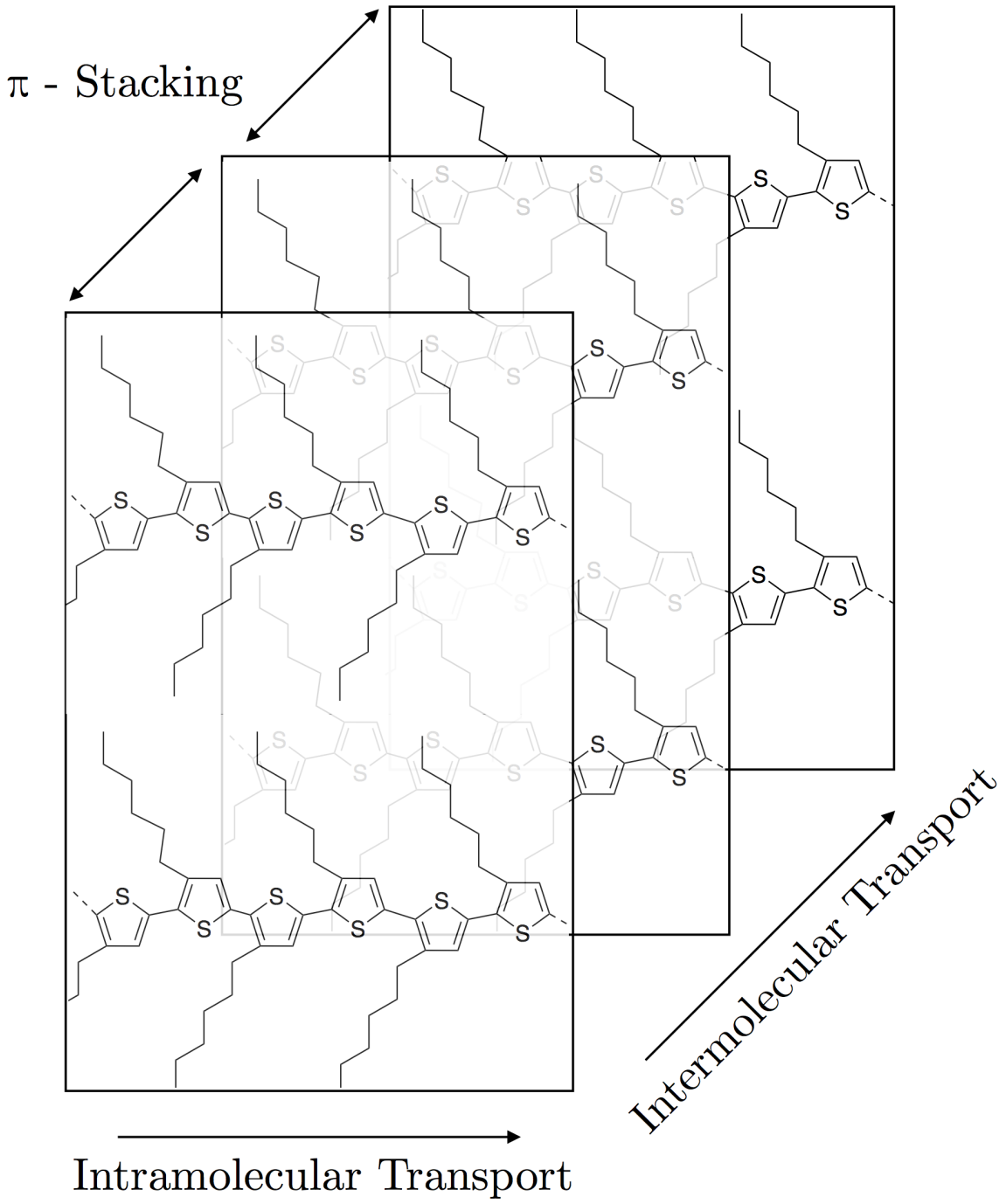

Figure 1.6: Charge transport through a P3HT film. Intramolecular transport occurs along the conducting polymer backbone, while intramolecular transport occurs between adjacent polymers through π stacks.

measurements a bias is applied across a device and the current response is observed. The measured current response is a result of both inter- and intramolecular transport, and it is difficult or impossible to deconvolute the contribution of each effect.

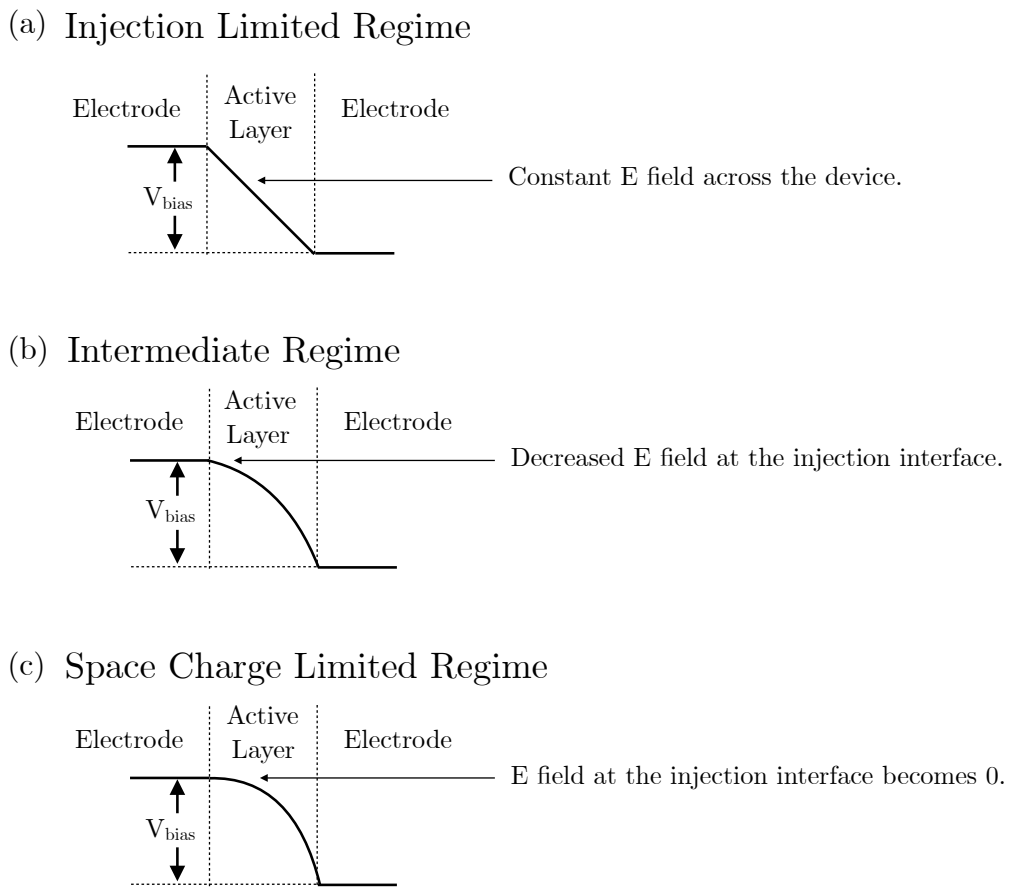

Figure 1.7: (a) When a bias is applied across devices with a uniform dielectric constant and no net charge density, the net field is constant across the device. In this regime, current is limited only by the rate at which charge can be injected into the active layer. For materials with high mobility, this is often the case since charges can travel through the active layer more quickly than they are injected into it. For materials with low mobility, this can occur due to large injection barriers at the injection interface, or very small fields being applied to the device. (b) If charge carriers are injected into the active layer at a higher rate than they can travel through the device, a net charge density will form within the device. This net charge density will create a field that opposes the field created by the applied bias at the injection interface, reducing the net field at the injection interface. This reduces the rate of charge carrier injection. In this regime, both the rate of charge carrier injection and space charge buildup contribute to limiting current through the device. (c) In the SCLC regime, space charge within the active layer builds up to such a degree that the field at the injecting contact interface becomes 0.

Common techniques used to study charge transport in organic electronics include space-charge limited current (SCLC) methods, field-effect transistor measurements, and current extraction through linearly increasing voltage (CELIV).[38] SCLC is one of the most widely used models for extracting mobility from IV curves. SCLC is an attractive model because it requires a simple experimental setup ans is easy to implement.[32] Like most models employed to probe mobility in organic electronics, the technique was originally developed for inorganic systems. The model assumes that charge carriers are injected into the device much faster than they can move through the device and therefore a net charge density (space-charge) builds up within the material. This space-charge generates an electric field which opposes the field at the injecting contact. As charge builds within the material, the opposing electric field builds, until the net field at the injecting contact is 0 (Figure 1.7). The equation for SCLC is given by

$$J = \frac{9}{8}\mu\epsilon_r\epsilon_0\frac{V^2}{L^3}, \tag{1.5}$$

where J is the current density, ϵ_r is the dielectric constant of the material, ϵ_0 is the vacuum permittivity, V is the applied bias, and L is the distance between electrodes. Mobility is extracted when a quadratic relationship between J and V is observed, which often occurs at high biases. However, simply observing a quadratic relationship is not enough to determine if SCLC is occurring and if the model is correct.

The erroneous application of the SCLC model to systems which do not satisfy SCLC's underlying assumptions can result in extracting incorrect mobilities (Figure 1.8).[39] If the resulting injection barrier of the injecting electrode is too large, or the applied bias is too small, the space-charge limited transport regime will not be reached and mobility will be underestimated.[39] The characteristic $J \sim V^2$ relationship is often observed even outside of the SCLC regime,[39] so goodness of fit is not sufficient to justify the SCLC model. Tuning the injection barrier to be small, or 'ohmic', is essential for SCLC measurements. Generally, understanding the electrode-OSC interface is essential for interpreting charge transport

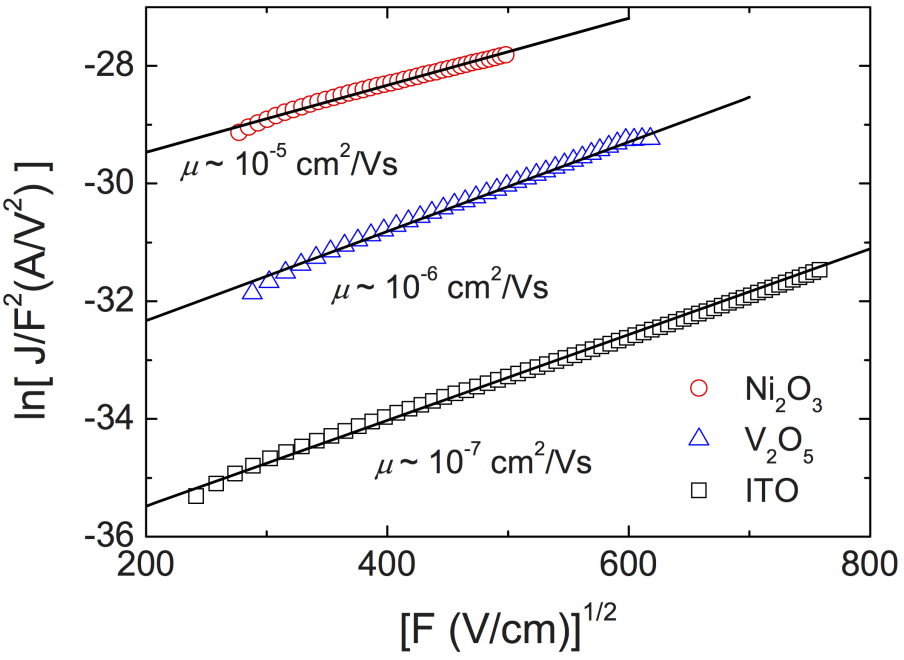

Figure 1.8: Linearized data and SCLC fit for mobility extraction. Three electrodes made of different metals were deposited on a single OSC film. Extracted mobility spans two orders of magnitude and depends on the work function of the metal electrode (i.e. the size of the injection barrier), indicating that the SCLC model is inadequate to describe transport for these devices. Figure 2 in Ref [39], reproduced with permission.

measurements.[27,39]

1.2.3: Metal - Organic Semiconductor Interfaces

For many OSC devices, electrodes are used to extract and inject charge carriers into the active layer. The interfaces between the electrodes and the OSC have a large effect on the electronic characteristics of a device.[27,39] For conducting polymers, understanding the electrode-polymer interface is essential in order to interpreting electronic measurements of the polymer.

In many organic electronic devices charge carriers are injected from metal electrodes into molecular orbitals within the active layer.[5] Generally, electrode work function falls between the HOMO and LUMO levels of the OSCs, resulting in a potential barrier which the injected

charge carrier must overcome (Figure 1.9). This requires thermal excitation, or tunneling through the barrier. The larger the injection barrier and the lower the temperature, the harder it is for charge carriers to be injected.[40] The size of the injection barrier for electrons (holes) is determined by the energy difference between the electrode work function and the LUMO (HOMO) energy level at the polymer-electrode interface.[40] The majority charge carrier is determined by the carriers with the lowest injection barrier.

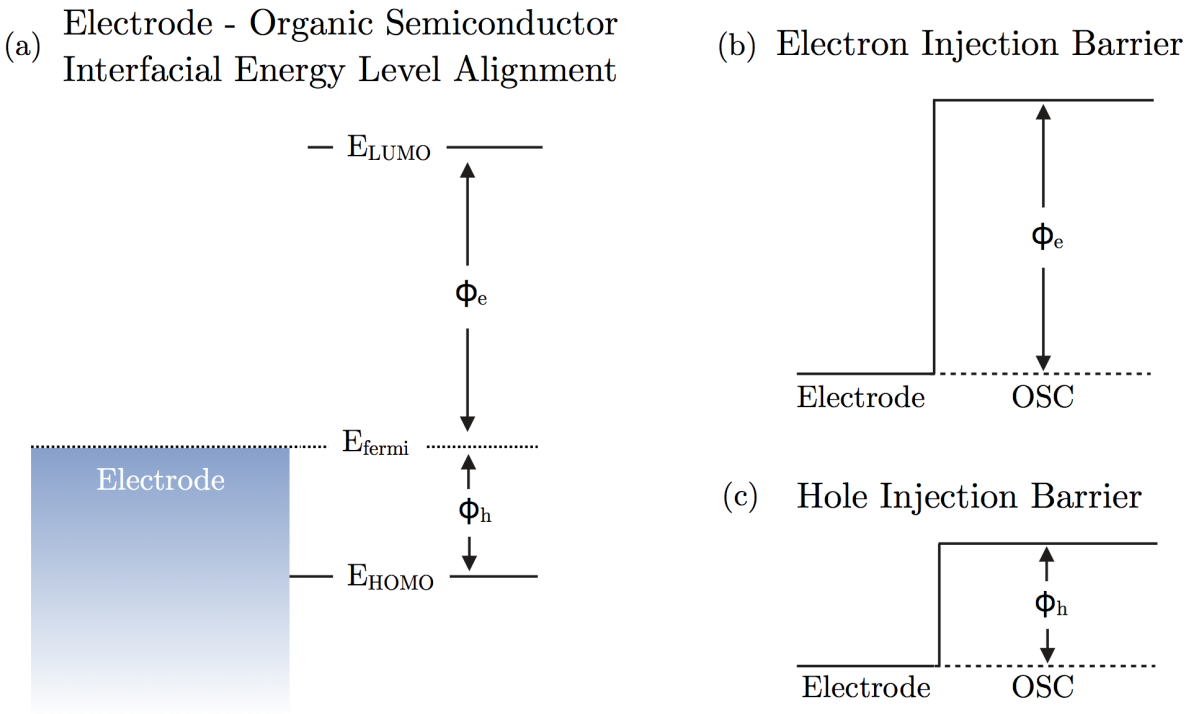

Figure 1.9: Charge injection from electrodes into polymer must occur at the electrode-polymer interface. (a) The energy level alignment of a metal electrode and an organic semiconductor at the interface. (b) The resulting injection barriers for holes and electrons. The size of the injection barrier is determined by the distance between the metal's fermi level and the HOMO (holes) or LUMO (electrons) levels.

When OSCs and electrode come into contact, deformation of the HOMO and LUMO levels can occur, much like band bending in inorganic semiconductors. However, a naive, but attractive model for the resulting barrier at the OSC-electrode interface is the vacuum level alignment, or Schottky-Mott rule.[41] In this model, the fermi level of the OSC moves freely to align with the fermi level of the metal without affecting the vacuum, HOMO, and

LUMO levels of the OSC.[41] The resulting injection barrier is just the difference between the metal work function and the HOMO level for holes, or the metal work function and the LUMO level for electrons (Figure 1.9). In this model, the injection barrier can be made arbitrarily small for the charge carrier of choice by picking electrodes whose work function matches the HOMO or LUMO level of the OSC.[41] In practice, low injection barriers are generally desired,[38] leading to 'ohmic contacts', contacts with an injection barrier small enough that the current through the device is not limited by the injection barrier, but by other processes such as charge carrier scattering or space-charge buildup. Ohmic contact are required for SCLC.[39]

In general energy level alignment at electrode-OSC interfaces is more complicated than the vacuum level alignment model. When the fermi level of the electrode is far from the HOMO or LUMO levels of the OSC, vacuum level alignment is an accurate model, and the interfacial behavior is well described by the Schottky-Mott rule.[42] However, when the electrode fermi level is close to the HOMO or LUMO level of the OSC, charge transfer can occur between the electrode and the OSC causing a dipole to form and vacuum level alignment to no longer be an accurate model. For a given material the onset of charge transfer appears to occur at a constant energy relative to the HOMO and LUMO levels, often referred to as the pinning energies or charge transfer onset energies (λ_+ and λ_-).[42] There are many competing theories for why this charge transfer occurs, and why pinning occurs at specific energies for a given material. Some explanations include the formation of polaron states forming at energies close to the HOMO or LUMO level,[43] or metal induced gap states (MIGS) due to the electronic states of the metal electrode interacting with the OSC and inducing states around the HOMO and LUMO levels near the interface,[44] among other models.[42] The cause of the phenomena is debated,[42] but there is a consensus that charge transfer begins to occur at these pinning levels due to localized states. As charge transfer occurs at the interface to align the fermi levels of the OSC and electrode, band bending occurs as well. This is different than the vacuum level alignment limit, which occurs far from the

HUMO and LUMO level where there are no electronic states in the OSC, and therefore no charge transfer or band bending occurs (Figure 1.10). The phenomenon is well documented both experimentally (Figure 1.11) and theoretically,[41,42,45] and results in a minimum energy barrier for the HOMO and LUMO injection barriers that cannot be reduced by matching the work function of the metal with the HOMO or LUMO energy of the OSC. The presence of a minimum injection barrier can make building OSC devices with ohmic contacts difficult or impossible.

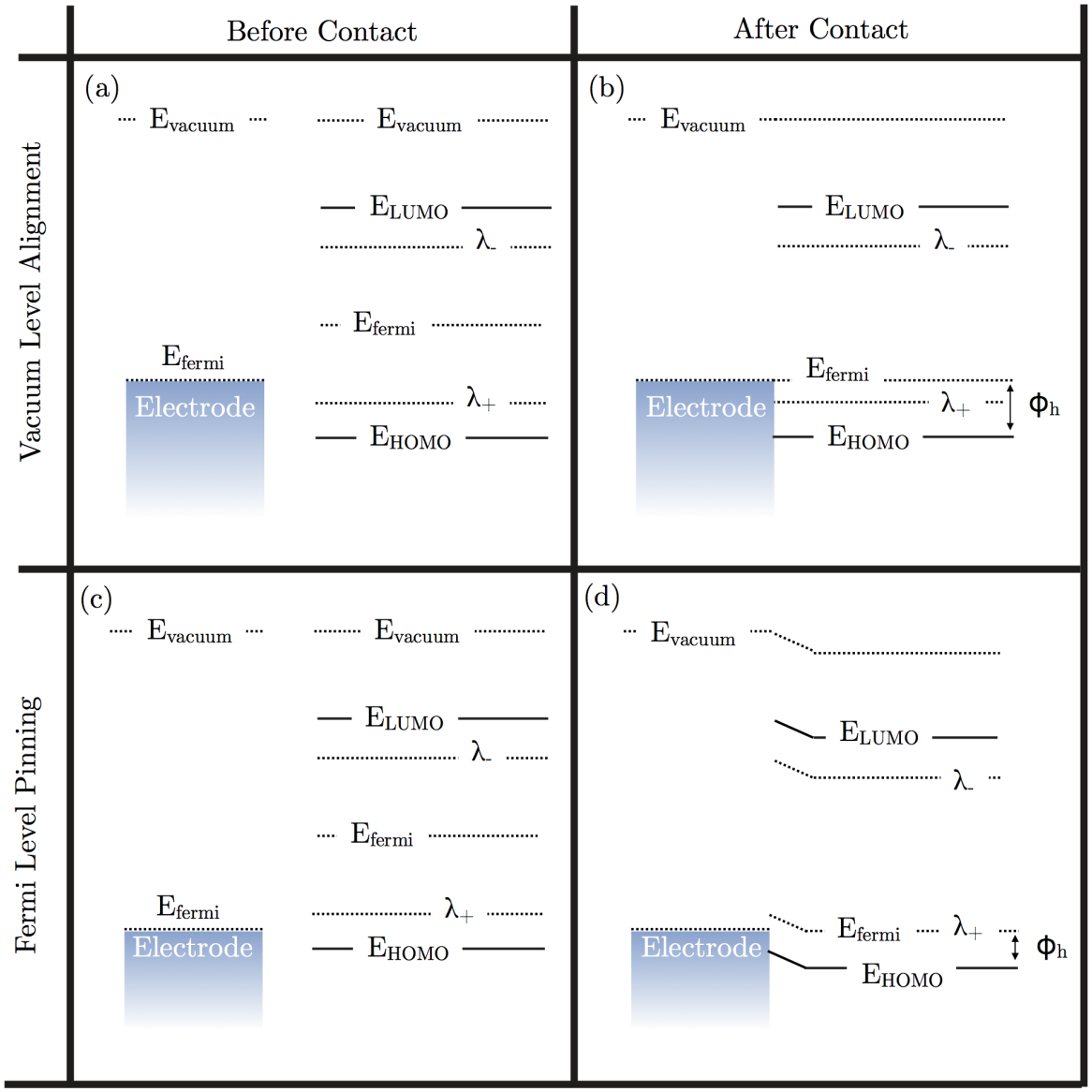

Figure 1.10: (a) and (c) show the energy level diagrams for a metal electrode and an OSC before they come into contact. The fermi level of metals is generally between the HOMO and LUMO levels of most OSCs. The λ levels represent pinning energies for the HOMO and LUMO level. (b) The energy level alignment of a metal electrode and OSC when the metal's fermi level falls between the OSC's pinning levels. No charge transfer or band bending occurs, and the injection barrier is determined by the difference between the metal's work function and the OSC's HOMO level ($\phi_h = W_{metal} - E_{HOMO}$) and the work function of the OSC equals the work function of the metal. (d) The energy level alignment for a metal electrode and OSC when the metal's fermi level falls between the OSC's pinning level and the HOMO level. Electronic states exist at these energies, allowing charge transfer to occur at the interface which results in band bending. The injection barrier cannot be reduced to less than $\lambda_+ - E_{HOMO}$ and the work function of the OSC is pinned to λ_+, and is constant.

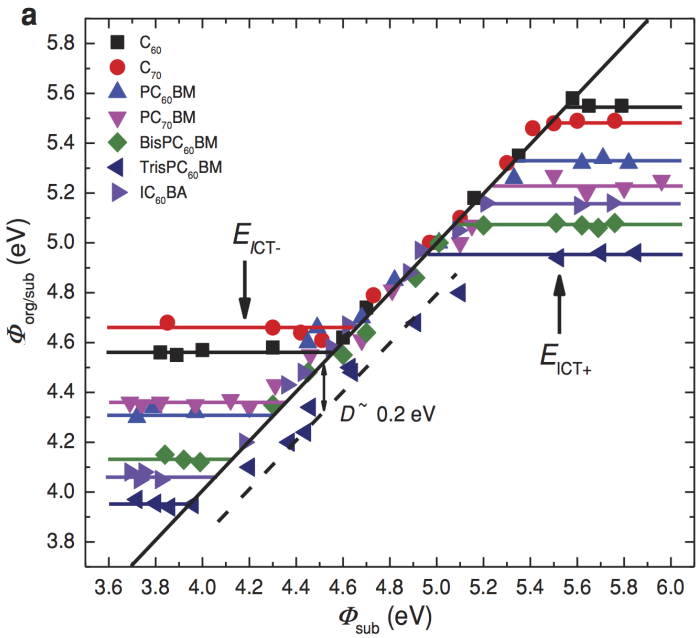

Figure 1.11: Transition between vacuum level alignment and fermi level pinning at metal-OSC interfaces. In this figure E_{ICT+} and E_{ICT-} correspond to λ_+ and λ_- in Figure 1.10. The work function of many OSCs was measured on different substrates by ultraviolet photoelectron spectroscopy (UPS). The work function of the OSCs is equal to the work function of the work function of their substrates in the middle part of the graph, consistent with vacuum level alignment as shown in (b) of Figure 1.10. When the substrate's work function becomes close to the HOMO or LUMO levels of the OSC and hits the pinning energies (λ_+ or λ_-) the work function of the OSC becomes pinned, which results in a constant OSC work function when the substrate work function is above (below) λ_+ (λ_-). When the OSC work function becomes pinned the injection barrier cannot be further reduced as shown in (d) of Figure 1.10. Figure 1 in Ref [45], reproduced with permission.

Section 1.3: Molecular Electronics

1.3.1: A Brief History and Overview of Molecular Electronics

Molecular electronics is the study of molecules as individual electronic components, as opposed to the properties of OSCs.[46] Molecular electronics includes the study of both single molecules and ensembles of parallel molecules. Molecular wires are often presented as the ultimate nanoscale building block,[47] and the smallest conceivable stable structures which can be integrated into an electronic circuit.[48] Potential uses for molecular wires include memory storage and transistors,[48] but commercial devices incorporating molecular wires are currently a distant goal.

Self-assembled monolayers (SAMs) are one of the most common molecular wire ensembles studied. SAMs consist of a single layer of aligned molecules on a substrate. Molecules in SAMs often have a 'head' group on one end that interacts strongly with the substrate, and a 'tail' group which orients away from the substrate at some tilt angle relative to the normal. SAMs can be covalently bound to the substrate, or interact with the substrate through weaker Van der Waals forces. Functional groups can be attached to the end of the tail on SAMs to tune the properties of the monolayer, such as making the SAM interact more strongly with a top electrode.

The electronic properties of molecular wires were first probed in the early 1980s after the development of the STM.[49] Measurements on single molecules with an STM tip are transient in nature. In these measurements a conducting tip is brought into contact with one end of a molecular wire that has been grown from or attached to a conducting substrate.[49] A temporary metal-molecule-metal (MMM) junction is formed with the conducting tip acting as one electrode and the substrate acting as the other electrode. After the measurement is over the tip moves on to a new molecule to form a new junction. The transient nature of the STM-based junction is a common in MMM junctions.[49]

MMM junctions consist of five components: two electrodes, the molecule, and two metal-

molecule interfaces. Each part of the MMM can be tuned individually to affect the performance and properties of the junction. Different metals can be used for the electrodes. Different linker groups can be used in the interfaces to attach the molecule to the electrodes, or the linker groups can be foregone completely. Different molecules can be put inside the junction. MMM junctions can contain a single or multiple molecules,[47] but every molecule must touch both electrodes. The electronic properties of single molecule junctions can be difficult to measure for larger molecules. The resistance of individual molecules is quite large, and so the current response for large single molecules can be immeasurably small at low biases. Multiple molecular wires act as parallel resistors, so adding more molecules to a junction lowers its resistance.[47] Junctions containing multiple molecular wires are usually necessary for measurements on longer molecules.

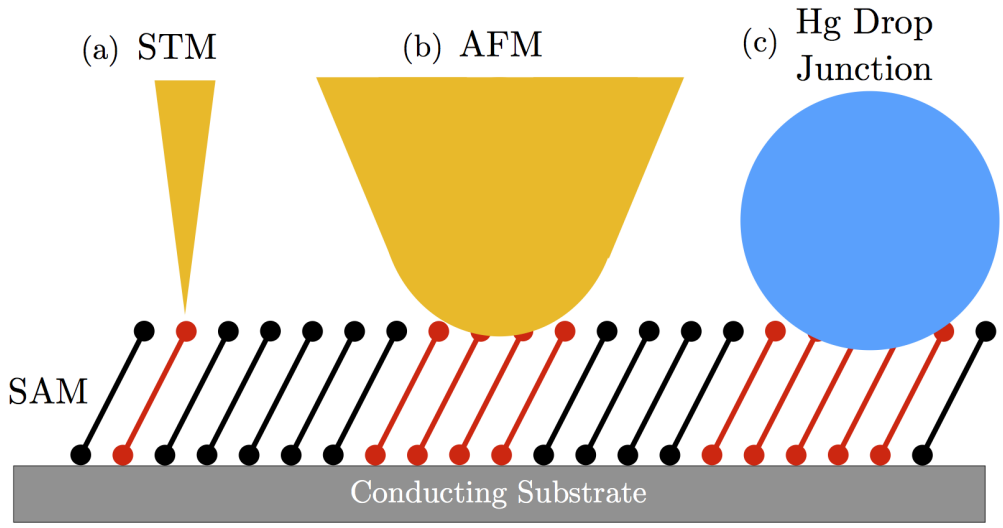

Figure 1.12: Schematics for some common MMM junctions are shown. (a) An STM MMM junction. STMs have the resolution to address single molecules with their conducting tips, allowing the electronic properties of single molecular wires to be probed. (b) AFM tip contacting a SAM. AFM tips are much larger than STM tips and address hundreds of molecules simultaneously. (c) Hg drop junction. In these junctions a liquid Hg drop is put on the end of a wire and brought in contact with a SAM. These junctions address 10^{10} to 10^{11} molecules.

Though many device geometries and measurement techniques have been devised, most

MMM devices are transient and permanent molecular electronics devices are not widely used. Creating permanent contacts is difficult for single molecule junctions since their locations must be precise on an atomic scale.[47] For devices which include multiple molecular wires, the contact locations do not need to be as precise as for a single molecule, but the monolayers used in molecular electronics tend to be very thin (<20 nm) and depositing contacts without shorting through the monolayer is difficult.[47] Some techniques, such as transfer printing, do allow permanent contacts to be made on top of SAMs, but these permanent contacts still can only be addressed by AFM or similar techniques.[48]

1.3.2: Charge Transport in Molecular Wires: From Tunneling to Hopping

Unlike organic thin films, the concept of mobility is often not applicable to molecular electronics. Mobility is a measure of a charge carrier's drift velocity, and molecular wires are usually not long enough for the concept of a drift velocity to make sense.[40] For short molecular wires the charge carrier never directly enters the material, instead tunneling directly from electrode to electrode. Tunneling current can be modeled using the Simmons model[50]

$$I = \frac{qA}{4\pi^2\hbar d_0^2}\left[(\phi - \frac{qV}{2})exp\Big[-\frac{2(2m)^{\frac{1}{2}}}{\hbar}\alpha(\phi - \frac{qV}{2})^{\frac{1}{2}}d_0\Big] - (\phi + \frac{qV}{2})exp\Big[-\frac{2(2m)^{\frac{1}{2}}}{\hbar}\alpha(\phi + \frac{qV}{2})^{\frac{1}{2}}d_0\Big]\right], \tag{1.6}$$

where I is the current, q the electron charge, A is the area of the junction, $\hbar$ is the reduced Planck constant, d_0 is the tunneling distance, ϕ is the tunneling barrier height, V is the applied bias, and m is the charge carrier's effective mass. While the full current voltage dependence of devices is often probed for molecular wires, one essential benchmark is the relationship between a molecular wire's length and its zero-bias resistance.[51] The zero-bias resistance behavior for short devices which exhibit tunneling can be derived from equation 1.6, and is given by

$$R = R_0 e^{-\beta d_0} and \tag{1.7}$$

$$\beta = 2(2m\phi)^{\frac{1}{2}}/\hbar, \tag{1.8}$$

where R is the resistance, R_0 is a contact resistance, d_0 is the molecular length, m is the effective mass of the charge carrier, ϕ is the height of the tunneling barrier, and β is the tunneling decay coefficient which describes the efficiency charges tunnel through a material.[51] β is measured by plotting log resistance vs length and measuring the slope of the line.[52] Since the tunneling probability depends exponentially on length, the semilog plot should be linear. The β parameter is widely used across the field as a benchmark for characterizing molecular wires.[51]

Tunneling usually only occurs in molecular wires less than 5 nm in length,[51] and in this length regime the resistance of the molecule depends exponentially on the molecule's length. As the molecule gets longer a transition is observed in the length dependence of molecule's resistance (Figure 1.13).[51] The relationship between a molecular wire's resistance and length transitions from exponential to linear as the molecule becomes longer, indicating a transition in charge transport mechanism.[51] For longer molecules, charge is injected into the molecular wire (or wires) instead of tunneling through them, and band-like or hopping transport occurs through molecular orbitals along the molecule or molecules.[51]

Molecular junctions are expected to exhibit some finite contact resistance, which is determined by extrapolating the resistance of the device at 0 length. However, for molecular electronics, extrapolating the resistance at 0 length using the linear regime of the resistance vs. length plot will result in a negative resistance.[51] This phenomenon occurs in both single molecule and SAM devices. When charge carriers are injected into a device, they tunnel a finite distance into the molecular wire (or wires), on the order of 2-5 nm. They are also extracted from the molecule(s) a finite distance away from the extracting contact (roughly

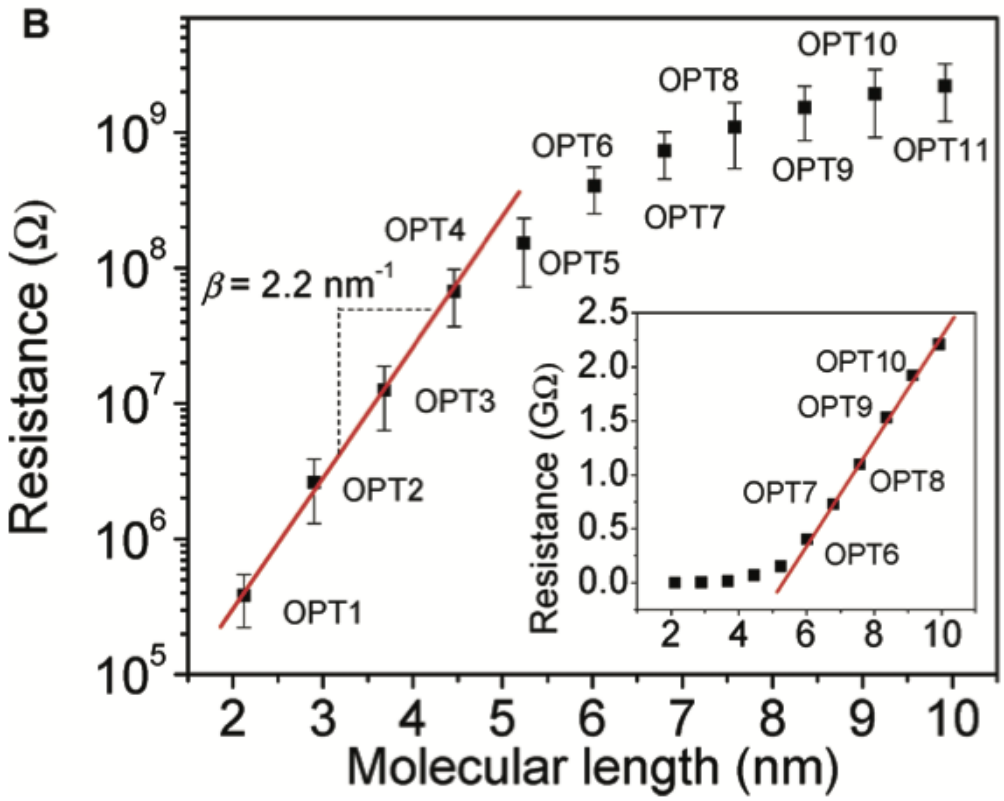

Figure 1.13: A transition between exponential and linear relationship between molecular length and resistance is shown. The transition indicates a change from direct tunneling between electrodes to hopping transport within the molecule. Figure 3 in Ref [53], reproduced with permission.

2-5 nm as well).[40] Because of this, the distance that the charge carriers travel through the active layer is less than the total molecule length and the total thickness of the device.

While covalent linkage of molecular wires to one or both electrodes in molecular electronics devices has allowed the study of transport along single molecules, the strategy is not scalable to longer molecule lengths due to synthetic and technical limitations.[54] Molecular wires over 20 nm in length have not been studies experimentally, which limits the potential of SAMs and single molecules to study intramolecular transport. Developing a system that can combine the advantages of the metal-molecule-metal geometry of molecular electronic devices with the device thickness and permanent contacts of organic electronics would offer a unique opportunity to study intramolecular charge transport.

Section 1.4: Polymer Brushes

Polymer brushes are microstructures made of densely packed polymer chains which are immobilized at one end, i.e. attached to a substrate surface or fluid interface.[55] This immobilization of one end of the polymer coupled with dense packing forces polymer-polymer interactions which causes the polymers to 'stretch out' into a 'brush' conformation.[55] Halperin *et al.* suggest that polymer brushes grow predominantly perpendicular to the surface on which they are immobilized. The thickness of a brush film, L, is given by

$$\frac{L}{b} = N(\frac{b}{d})^{\frac{2}{3}}, \tag{1.9}$$

where N is the number of monomers in the polymer, b is the length of a monomer, and d is the spacing between adjacent polymer chains.[55] For a given molecular weight, more densely packed brushes (i.e. brushes with low d) should result in longer, less isotropic, polymer brush films. Thus, the grafting density of polymer brushes has a very large impact on the conformation on polymers within the brush.[55]

Like SAMs, polymer brushes are grafted to a substrate; however, they can be grown much longer than SAMs.[54] Electronic devices comprising polymer brushes can be made by grafting the brush from a conducting substrate and subsequently applying a top electrode to the brush film. Because of the covalent bond between polymer chains and the substrate, polymer chains contacting the top electrode in a vertical device may enhance the contribution of intramolecular charge transport processes to and from the bottom electrode.[54]

CHAPTER 2: EXPERIMENTAL METHODS

Section 2.1: P3MT Brush Synthesis and Device Fabrication

P3MT brush growth occurs in solution. There are two main mechanisms by which solution polymerization can occur: chain growth and step growth.[56] Chain growth polymerization describes the sequential addition of single monomers to a propagating polymer chain, while step growth polymerization corresponds to monomers forming dimers, then larger oligomers, then oligomers coming together to form larger polymers. For P3MT brushes, greater control over brush length and packing density is desired, so chain growth polymerization techniques are used.[57] The reactive polymer chain is attached to a surface, and monomers are inserted onto a propagating chain one at a time.

The P3MT brush is grown through a process called Surface Initiated Kumada Catalyst-Transfer Polycondensation (SI-KCTP). A distinguishing characteristic that separates KCTP from other chain growth polymerization techniques is the ability for a catalyst to stay associated with one chain during the course of polymerization. After the addition of each monomer, the catalyst undergoes oxidative addition into the terminal carbon-halogen bond of the chain (Figure 2.1).[58] SI-KCTP has been demonstrated to produce P3MT films with some degree of vertical orientation from a conductive substrate.[57] The SI-KCTP growth mechanism follows living chain growth kinetics, meaning it is sensitive to parameters such as monomer concentration and temperature, and that the degree of polymerization of polymers within the brush is expected to increase linearly with reaction extent, resulting in low polydispersity (i.e. polymers have a fairly uniform length.)[59]

Previous reports have shown SI-KCTP from ITO using phosphonic acid functional groups (Figure 2.2a).[60–63] Phosphonic acid covalently bonds to surfaces which can undergo hydroxy-

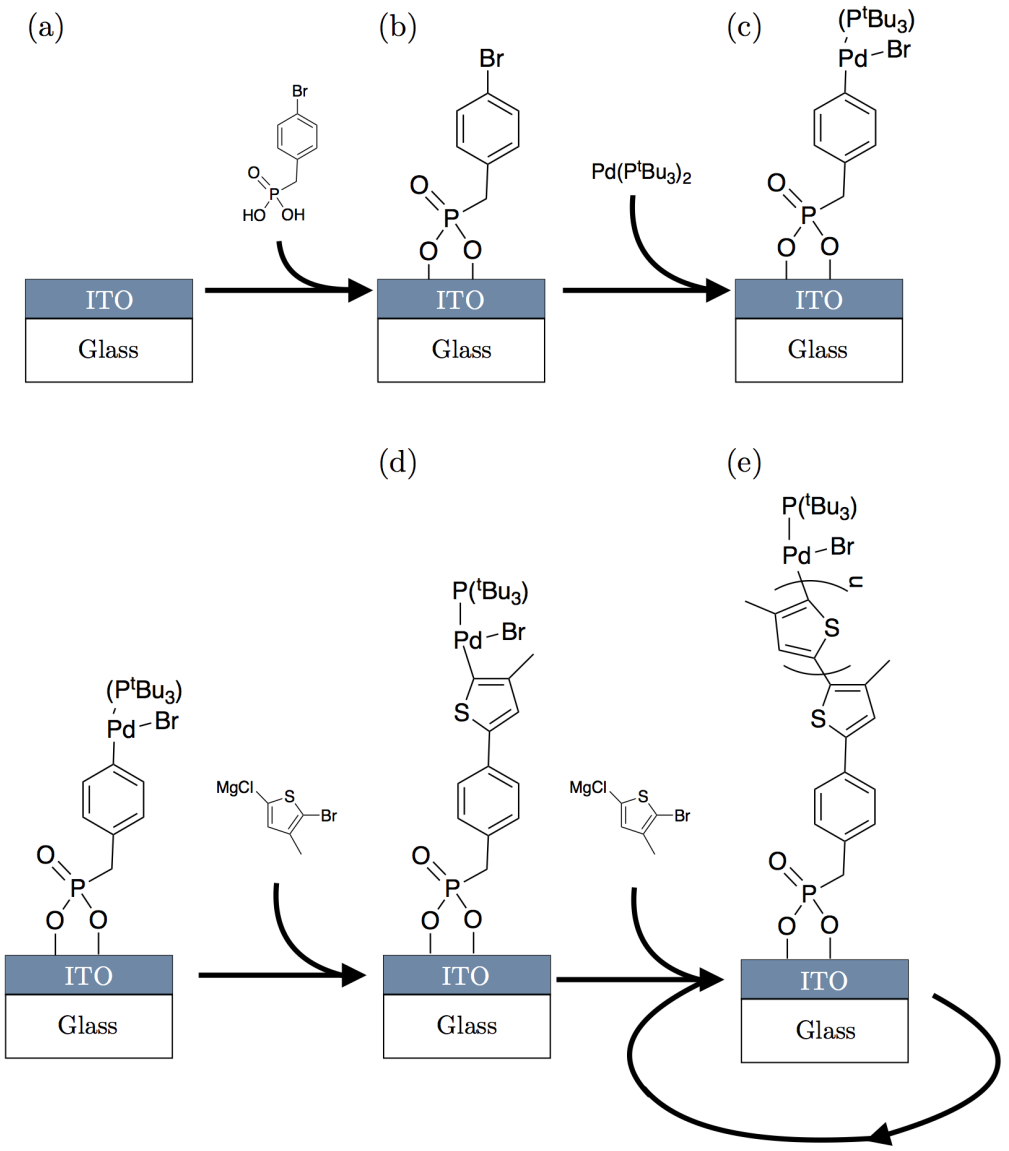

Figure 2.1: (a) A clean ITO substrate. (b) The substrate is functionalized with a seed monolayer. (c) The monolayer is initiated with Pd catalyst. (d) An initial monomer is grafted to the seed monolayer and polymerization (e) begins.

lation, such as indium tin oxide (ITO) or SiO_2, forming a monolayer on the substrate surface (Figure 2.1b). Different substrates are chosen for different device and measurement goals. ITO is a transparent conducting oxide, and is often used as the bottom electrode in electronic devices, but cannot be used as a substrate for certain measurements (e.g. Rutherford backscattering spectroscopy) since the ITO signal can obscure the brush signal. For these measurements, SiO_2 substrates are used.

(a) **Monolayer** (b) **Catalyst** (c) **Monomer**

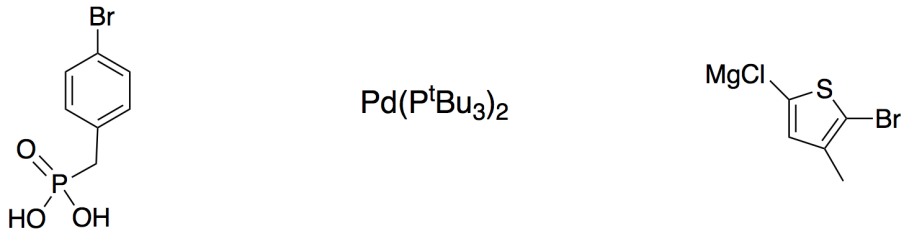

Figure 2.2: The essential molecules used in brush growth. (a) Brominated phosphonic acid, (b) catalyst, and (c) monomer.

Each phosphonic acid molecule acts as a potential anchor site from which P3MT chains can grow, and is referred to as a seed monolayer. After the substrate surface is functionalized by the phosphonic acid monolayer, a catalyst initiator (Figure 2.2b) is added. The catalyst allows SI-KCTP to occur. While multiple catalysts have been previously reported for SI-KCTP, Pd was chosen over Ni to reduce disproportionation[61] (the tendency of intermediate products in a chemical reaction to form into undesired compounds) and because polymer brushes grown using a Ni catalyst require prohibitively insulating monolayers to achieve vertical anisotropy.[54,64] Molecules within the monolayer must be initiated by the Pd catalyst in order to grow polymer chains, and not all molecules in the seed monolayer are initiated.[57]

Once the seed monolayer has been initiated, the substrate is submerged in a solution of monomers and polymerization begins. The monomers are 3-methylthiophene rings functionalized with MgCl on one end and Br on the other (Figure 2.2c). The MgCl end can be grafted onto phosphonic acid that has been initiated by the catalyst. The MgCl is removed from the monomer in the process and dissolves in the growth solution. When the monomer is grafted onto the seed molecule, the catalyst moves to the Br side of the monomer. As synthesis continues further, monomers are grafted onto the chain, and after each monomer is added the catalyst moves to the top of the chain. Growth can continue until the catalyst falls off of the chain, the polymerization process is quenched, or the substrate is removed from the growth solution.

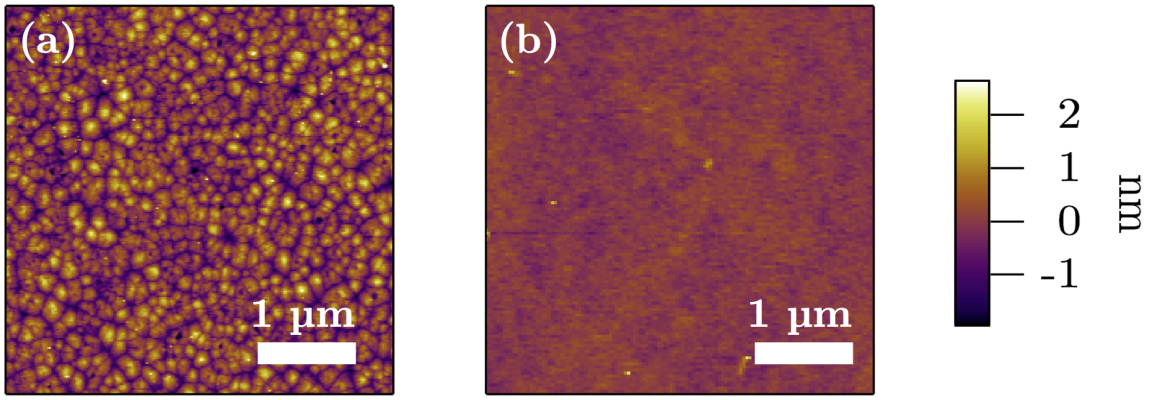

Figure 2.3: AFM images of two substrates used for brush growth. Both images are 5μm x 5μm. (a) ITO has characteristic grains and an RMS roughness of 0.6 nm. (b) SiO_2 has an RMS roughness of 0.2 nm.

3-methylthiophene monomers were selected for brush synthesis, to produce a Poly(3-methylthiophene) (P3MT) brush. P3MT is a derivative of polythiophene, a model conducting polymer, and exhibits high grafting density in Pd-catalyzed SI-KCTP.[57] Polythiophene is a widely studied conducting polymer, and the polythiophene derivative P3HT has received a large amount of interest due to the increased solubility conferred by its long hexyl side chains which allow it to be solution processed.[65] Solution processablity refers to the capacity for soluble polymers to be deposited on substrates from solution by inkjet printing, spin-coating, or other solution-based methods.[66] These techniques allow for scalable device fabrication due to the ability to uniformly coat substrates with very large areas.[62] Conjugated polymers tend to have low solubility due to the strong interaction between the π orbitals between chains,[62] and often can grow no longer than a few monomers before precipitating. Adding long alkyl side chains to conjugated polymers can increase their solubility.[67] While the long hexyl side chains make P3HT attractive for solution processing techniques, the long side chains prevent efficient brush growth.[68]

After the brushes are grown to the desired length, the catalyst is removed from all

remaining active chains, and the brush is thoroughly washed to remove excess catalyst, solvent and solutes such as left over monomer, Mg, and Cl. In this work, brushes were grown to thicknesses up to 100 nm. An "edge-view" SEM image of a grown brush is shown in Figure 2.4. The brush has an interesting morphology, much different than a solution processed films which tend to have a smooth surface and uniform film thickness. The brush is covered with "tall" features, termed as "columns".

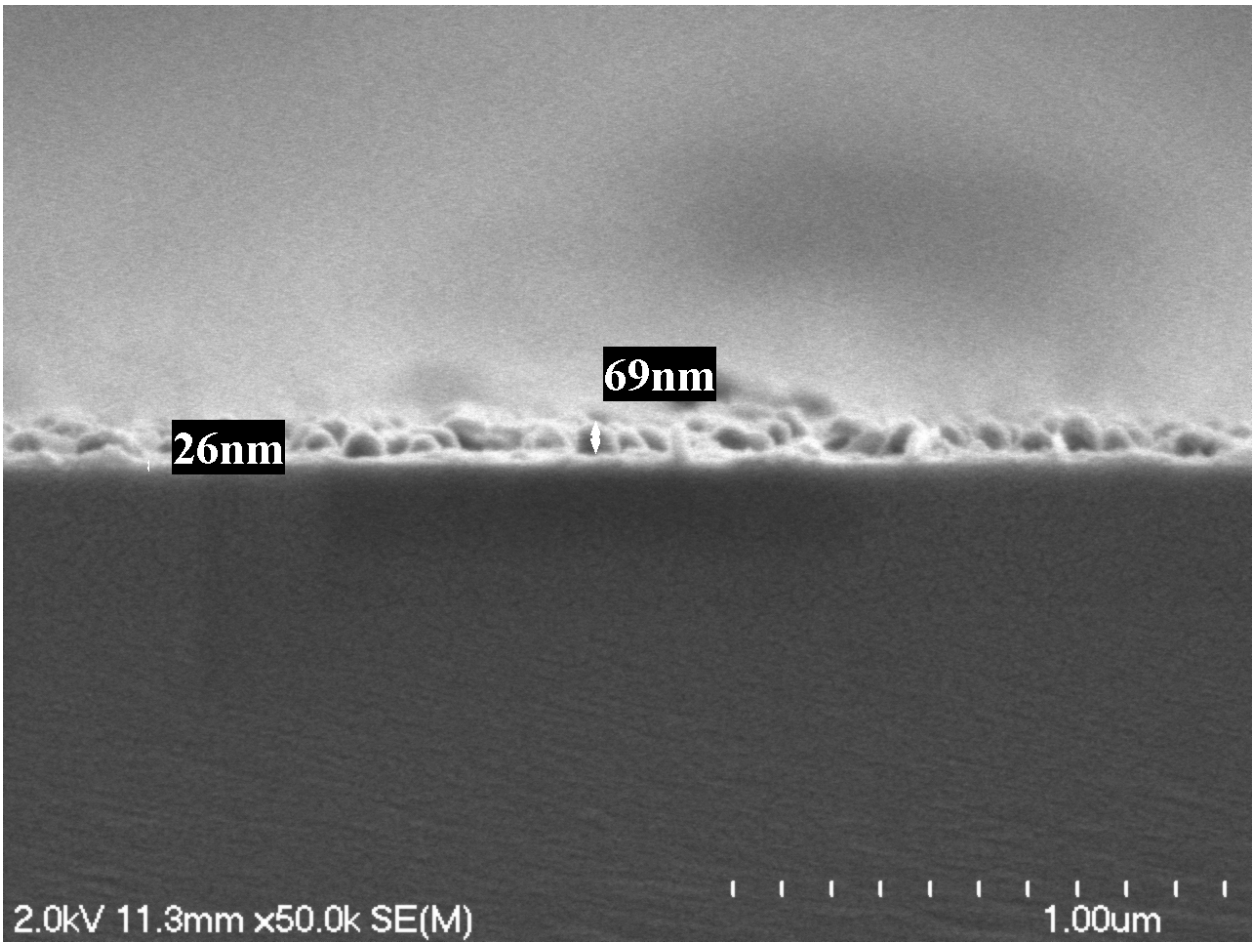

Figure 2.4: An SEM image of a P3MT brush grown on an Si/SiO_2 substrate

2.1.1: Experimental Procedure

Materials. All chemicals, reagents, and solvents were purchased from commercial sources (Sigma Aldrich, Acros, VWR, etc.) and used without further purification unless

otherwise noted. Dry THF was purified by distillation, and dry toluene (Fisher Chemicals) was used without further purification. Indium tin oxide (ITO) slides (1 inch x 1 inch, 145 nm sputtered ITO, sheet resistance 20 Ω/sq) and Si wafers (300 nm wet thermal oxide) were purchased from Thin Film Devices, Inc. and University Wafer, respectively. Au targets for sputtering were purchased from Kurt J. Lesker. 2-bromo-3-methyl-5-iodothiophene, 2-ferrocenyl-5-bromothiophene, (4-bromobenzyl)phosphonic acid, and magnessiated 2-bromo-3-methyl-5-iodothiophene were synthesized using established procedures.[60,61]

Preparation of ITO Substrates. ITO slides were sonicated in 18 MΩ deionized water, acetone, and isopropanol for 15 minutes each, then placed in RCA cleaning solution (5:1:1 H_2O:H_2O_2:NH_4OH) for an hour. After rinsing with water, isopropanol and drying under a stream of N_2, the slides were cleaned with UV/ozone (Jelight Company Inc., model 42A) for 15 minutes. They were then immersed in an 8-slot staining dish with 30 mL absolute ethanol containing (4-bromobenzyl)phosphonic acid (75 mg, 0.3 mmol) overnight. They were quickly dried under a stream of N_2 and heated in a glovebox at 150° C overnight. Lastly, the slides were cleaned with water and ethanol and dried under N_2 to yield monolayer-functionalized ITO.

Surface Initiated Kumada Catalyst Transfer Polycondensation (SI-KCTP) Methodology. SI-KCTP was adapted from a previous report.[61] Pd-catalyzed SI-KCTP was chosen over Ni to reduce disproportionation[61] and because polymer brushes grown using a Ni catalyst require prohibitively insulating monolayers to achieve vertical anisotropy.[64] Monolayer-functionalized ITO slides were initially placed in a staining dish containing a 10 mM solution of $Pd(P^tBu_3)_2$ in dry toluene at 70° C for 3 hours in a glovebox without stirring. The slides were then washed with excess toluene and THF, then immersed in a 0.15 mM solution of the magnesiated 3-methylthiophene monomer in dry THF at 40° C without stirring. At desired time intervals (longer growth time corresponding to thicker films), slides were removed from the glovebox and sonicated briefly in chloroform, water, and isopropanol. The resulting P3MT CPB films were stored in the dark under inert atmosphere.

Kinetic Transfer Printing (KTP) Process. This procedure was used to produce electrode-conjugated polymer brush-electrode devices for electrical measurements. A crosslinked poly(dimethylsiloxane) (PDMS) stamp (mixed 3.5:1 by weight with cross-linker, approx. 1 cm x 1 cm, Sylgard 184 Elastomer Kit, Dow Corning) was brought into conformal contact with the donor substrate. The stamp was quickly removed from the surface of the donor using pressure applied with a glass slide (rate of removal $>$ 10 cm/s), transferring the Au features onto the stamp. The "inked" stamp was brought into conformal contact with the receiving substrate (e.g. the brush film) with approximately 1 N of applied force, and removed very slowly ($\sim$0.5 mm/s), transferring the Au features onto the receiving substrate. The PDMS stamp was cleaned to remove particulates between each transfer using scotch tape.

Section 2.2: Bulk Structure Measurements

2.2.1: Cyclic Voltammetry

CV is an electrochemical measurement where a potential is applied across a device, linearly increasing from an initial potential to a maximum potential then decreasing to the original potential. The response current is measured as a function of potential. CV is generally conducted in solution, with the material being probed deposited on a conducting substrate which acts as one electrode, and the solution acting as the other electrode.[69] Peaks in the current vs potential plot form at potentials where oxidation and reduction occur, giving rise to the characteristic "duck" shape of cyclic voltammograms (Figure 2.5).[69] The area under these peaks corresponds to the amount of material undergoing the reaction.[69]

Films for CV measurements of Pd initiator density were prepared similarly to those used to grow conjugated polymer brush films. After oxidative insertion of $Pd(P^tBu_3)_2$ into monolayer-functionalized ITO slides, the samples were placed in a 0.02 M solution of magnesiated 2- ferrocenyl-5-bromothiophene (prepared identically to the 3- methylthiophene

monomer for SI-KCTP) overnight without stirring, then sonicated in chloroform, water, and isopropanol to yield ferrocene-capped monolayers with a density equal to the Pd initiator density. CV was performed in a custom 3-electrode electrochemical cell with the ITO substrate of the ferrocene-modified films acting as the working electrode, a platinum wire counter electrode, and Ag/AgCl reference electrode.[63] Tetra(n-butylammonium hexafluorophosphate) was the electrolyte (0.1 M) in thoroughly deoxygenated dichloromethane. Scans of ferrocene-capped monolayers on ITO were performed using a BASi Epsilon potentiostat, scanning from 0 to +1.2 V at 100 mV/s with several scans to allow for equilibration. The integrated oxidation peak was then used to calculate the surface density of the capped monolayer.

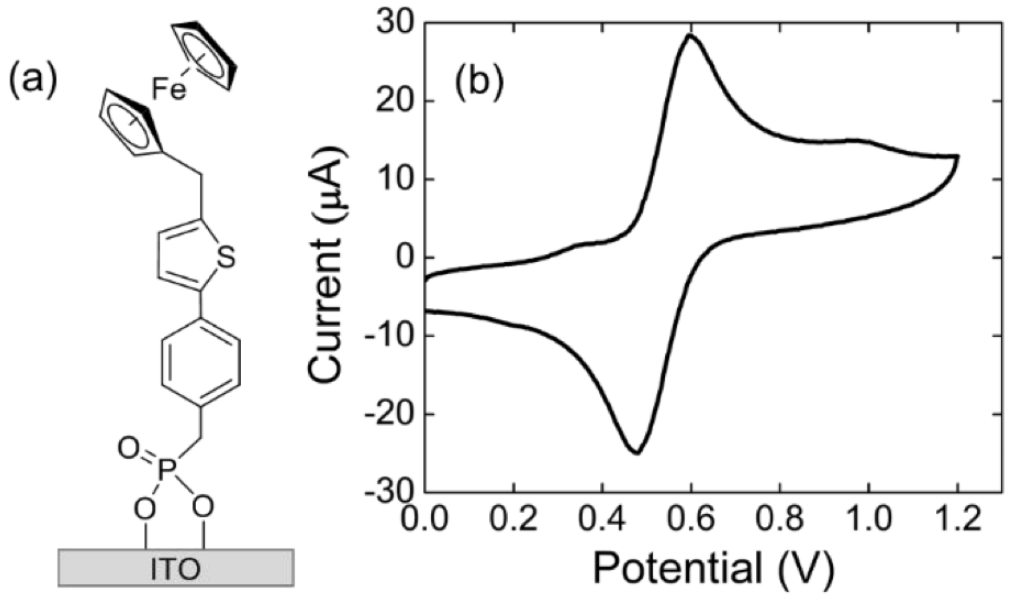

Figure 2.5: (a) structure and (b) cyclic voltammogram of ferrocene-capped bromobenzyl(phosphonic acid) monolayer. The oxidation peak area (80 μA) corresponds to $1.3 * 10^{14}$ initiators/cm^2. Figure S2 in [54], reproduced with permission.

Cyclic voltammetry is used to measure the HOMO level of polymer brush thin films which is combined with the optical bandgap to estimate the LUMO level of the polymer film (Figure 2.6). Poly(3-methylthiophene) brush films are electrochemically probed by

cyclic voltammetry. The ITO substrate the films are grown from is used as the working electrode with a platinum counter electrode and silver pseudoreference electrode used as supporting electrodes in dichloromethane tetra(n-butylammonium hexaflouorophospate) as the electrolyte. Cyclic voltammograms are taken by positively biasing the working electrode to reversibly oxidize the P3MT film. The onset of the oxidation wave corresponds to removing electrons from the film and is associated with the HOMO level of the polymer brush thin film. The HOMO level is calculated by using a ferrocene standard, and the HOMO level for the P3MT Brush is calculated to be -5.02 eV, corresponding closely to the HOMO level of spuncast films of P3HT at -5.1 eV. There were no observable peaks when applying a negative bias to the film, so the LUMO level cannot be measured in this way. This is not uncommon for polymer films, where often only the electrochemical HOMO level is reported.

2.2.2: Rutherford Backscattering Spectroscopy

Rutherford Backscattering Spectrometry (RBS) is a technique used to analyze the composition of thin inorganic films, and can determine the thickness, depth and elemental composition of individual layers within multi-layered films. RBS has also been used to characterize the composition of organic films, but it is not a widely used technique within the organic and molecular electronics communities.[70] The high energy nature of the measurement, which requires bombarding a film with a beam of nuclei, can damage the more fragile organic films.[71] If a significant amount of organic material is ejected from the film by the nuclei, the thickness of the film may change during measurement, making it difficult to interpret data.

Measurement of the density of spin cast P3HT films by RBS has been previously reported.[72] The average density of P3HT films was found to be 1.33 g/cm^3. To calculate this value, first the areal density of S is extracted from RBS spectra. Since each P3HT monomer has one S, the areal density of S is also the areal density of the monomer. The number of monomers per unit volume is then found by dividing areal density by average film thickness, as measured by atomic force microscopy (AFM).[72] Finally the number of monomers per unit

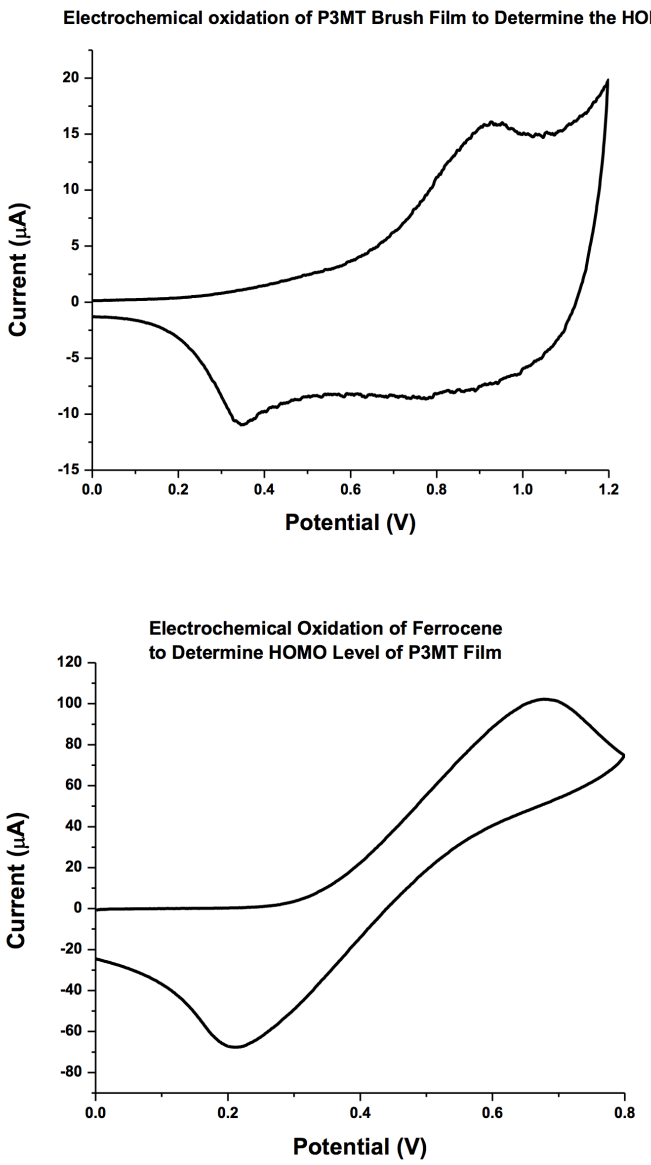

Figure 2.6: Cyclic voltammetry is performed to determine HOMO level of P3MT brushes. Reprinted with Permission from Travis LaJoie's Ph. D. Dissertation.[57]

volume is multiplied by the mass of the P3HT monomer to calculate the density of the P3HT film.

The use of RBS to measure the degree of polymerization in P3HT films has been previously reported.[70] In this report each P3HT is terminated by a Br group, therefore there is one

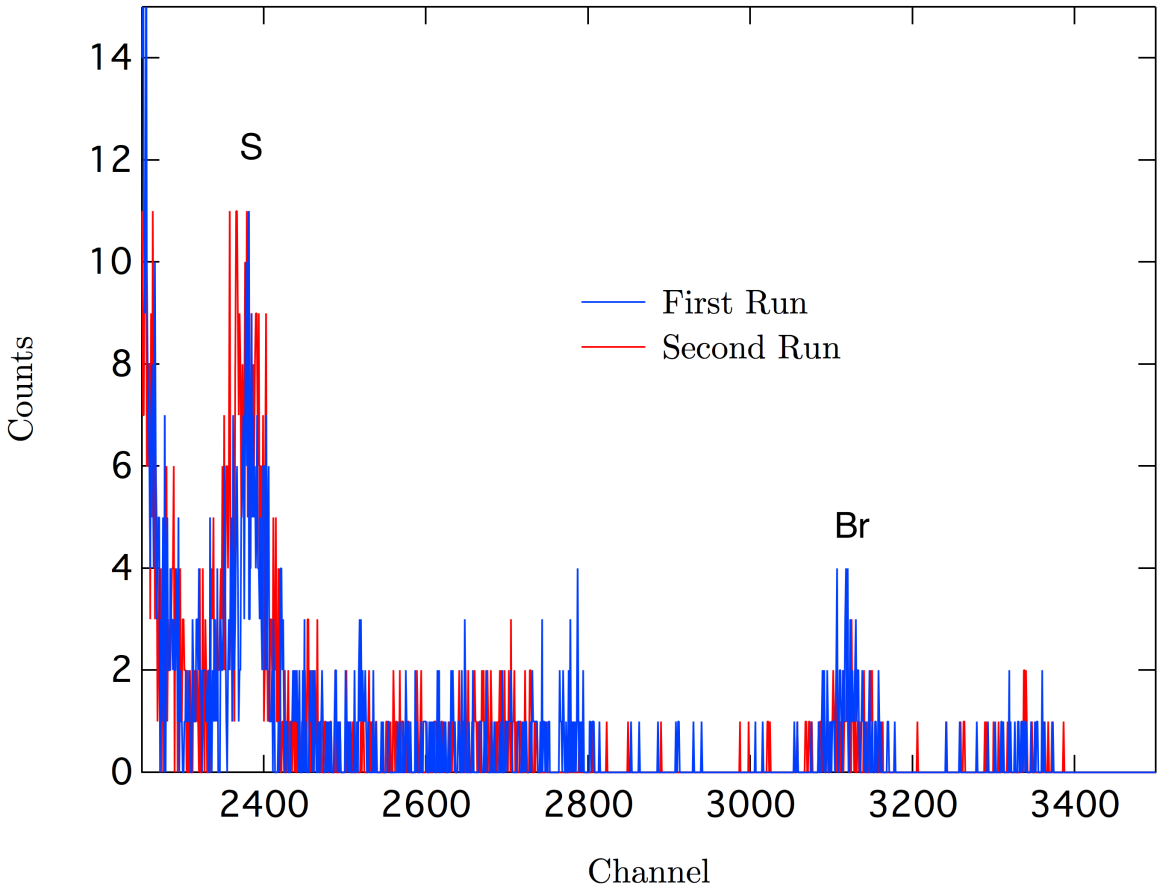

Figure 2.7: Repeated measurements on the same P3MT brush show no loss of sulfur signal, indicating no significant damage was done to the brush during measurement. The integrated S peak contained ∼400 counts in the first run, and ∼425 counts in the second run.

Br per polymer chain and one S for each monomer in the film. The degree of polymerization of the P3HT film is therefore given by the ratio of the areal densities of S and Br.[70]

Experimental Procedures. RBS measurements were performed at the Triangle Universities Nuclear Laboratory (TUNL) where a beam of 2MeV $^4He^{2+}$ particles was provided by the tandem electrostatic accelerator. Films were placed at a 0° angle with respect to the incident beam. Backscattered particles were detected at a scattering angle of 150°. The beam current was held to 30 nA. Repeated measurements of the same spot on the same sample were conducted to determine if the film had been damage during measurement. No loss of signal could be detected within experimental resolution, indicating that film damage

was not significant (Figure 2.7). The program SIMNRA[73] was used to calculate the areal density of sulfur and bromine atoms within the brush by fitting the simulated spectra to the measurement.

2.2.3: Grazing Incidence Wide Angle X-ray Scattering (GIWAXS)

Grazing Incidence Wide Angle X-ray Scattering (GIWAXS) is an X-ray diffraction technique used for probing molecular length-scale structure in thin films. The wide scattering angle collected during measurement correspond to large values of momentum transfer, which correspond to small distances. GIWAXS has been used extensively to determine the crystal structure of polymer films.[36,74–76] For conjugated polymers that have aromatic rings, and therefore exhibit π stacking behavior, the crystal structure is well known.[77] Polymers align in two dimensional planes, or lamellae, which stack on top of each other due to the attractive interaction of π orbital between neighboring polymers (Figure 2.8).[77]

Experimental Procedures. GIWAXS experiments were conducted at beamline 7.3.3 at the Advanced Light Source at Lawrence Berkeley National Laboratory. The collimated 10 keV beam was approximately 300 μm high and 800 μm wide. Its angle of incidence from the surface plane was 0.14°, penetrating the grafted film and experiencing total internal reflection at the glass substrate. A 2 M pixel Pilatus detector was used at a distance of 262 mm, calibrated by the use of a silver behenate standard. Data were reduced using the Nika software package.[78] The q values were converted to d values using $d = 2\pi/q$.

Section 2.3: Surface Morphology

2.3.1: Atomic Force Microscopy (AFM) and Scanning Electron Microscopy (SEM) Imaging

SEM measurements were performed using a Hitachi S-4700 Field Emission SEM (Tokyo, Japan). AFM measurements were performed using an Asylum Atomic Force Microscope (Asylum MFP-3D, Asylum Research). Tapping-mode topography images were taken using

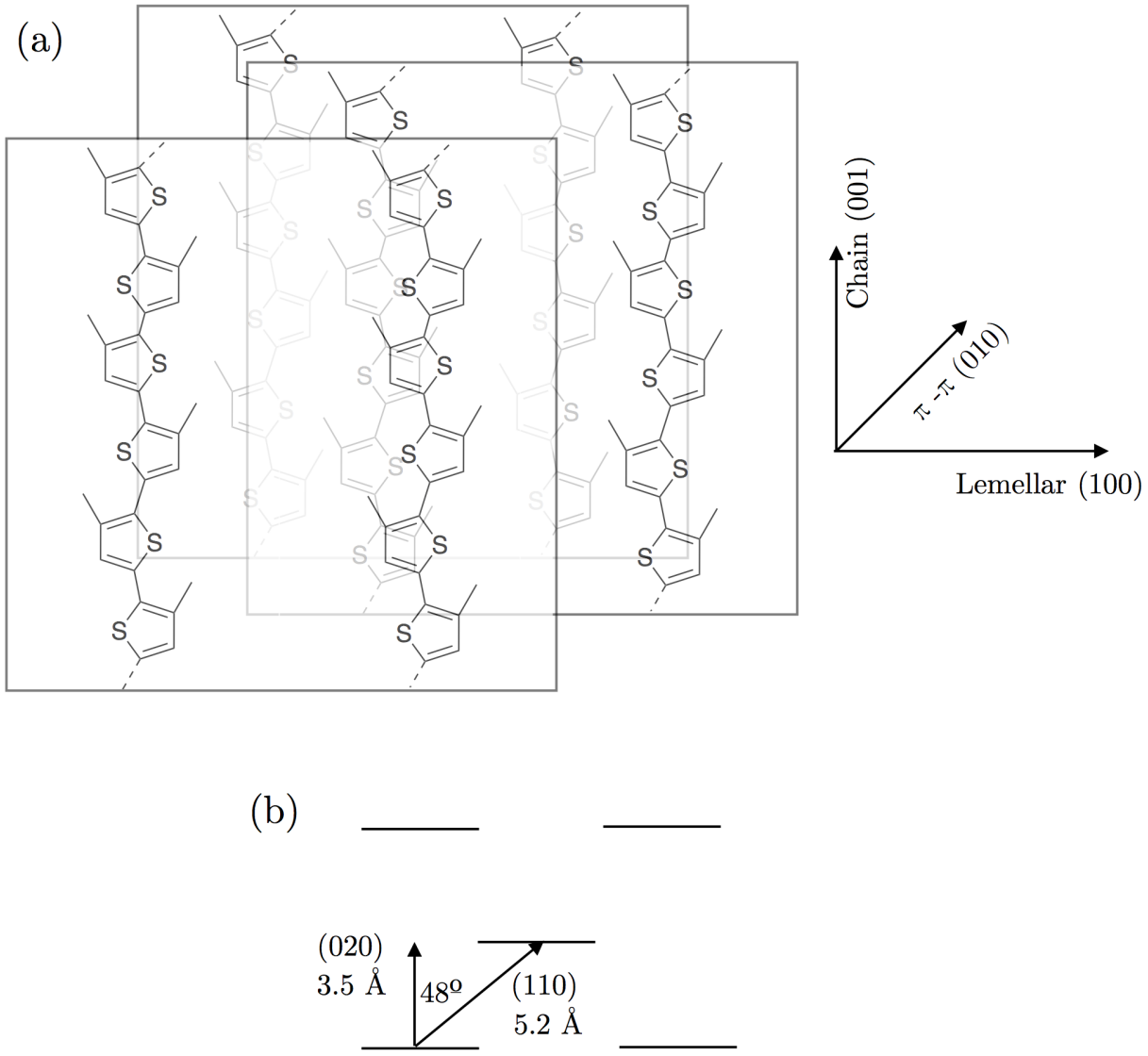

Figure 2.8: (a) The crystal structure of P3MT. The lattice vectors are defined along the chain axis (001), the π-π axis (010), and the lamellar axis (100). (b) A top down view of the P3MT lattice along the chain axis in real space. The reciprocal space vectors detected by GIWAX are the (020) and (110) vectors, which are 3.5 Å and 5.2 Å respectively (see Morphology section).

silicon cantilevers (Tap300Al-G, BudgetSensors) with a force constant of 40 N/m and resonance frequency of 300 kHz. To determine the nominal film thickness, P3MT films were

scratched using a 20 gauge steel needle and the scratched step was imaged using the AFM. The film thickness is defined as the peak-to-peak height difference between the respective height histograms of the ITO surface and brush film surface. The I-V measurement circuit is shown in Figure 2.9.

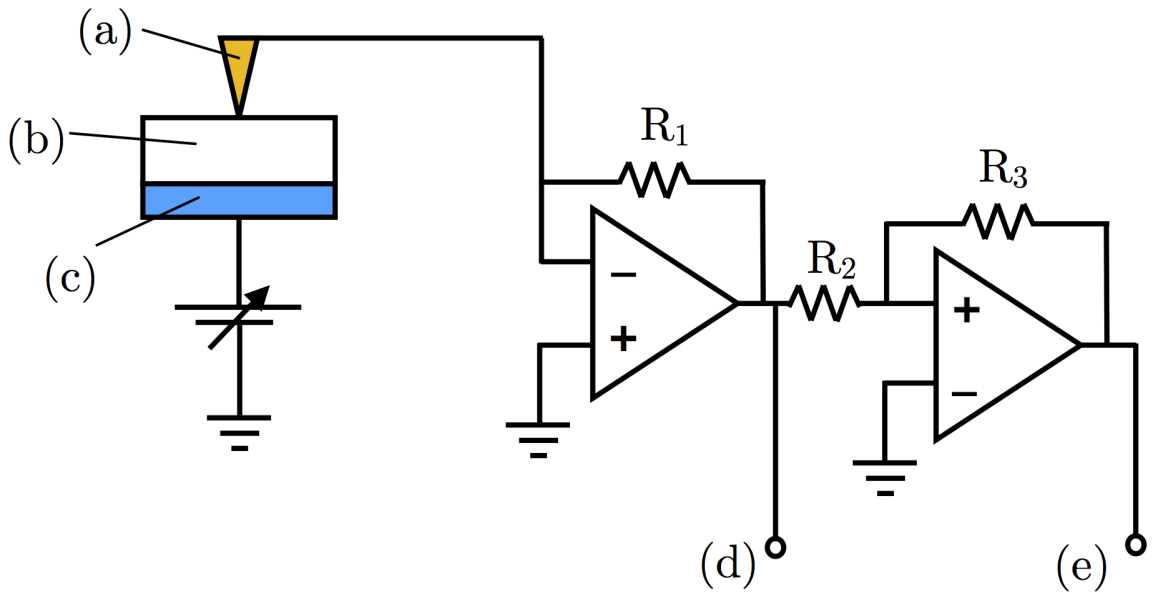

Figure 2.9: The circuit diagram for cAFM used in CPB device measurements. (a) The conducting tip, held at ground. (b) The CPB film. (c) The conducting substrate. (d) The low gain current channel. (e) The high gain current channel. Having a low and high gain current channel allows a larger range of currents to be detected with high precision. The gain of (d) and (e) could be adjusted by changing resistors R_1, R_2 and R_3.

2.3.2: Height-Height Correlation Function

The height-height correlation function, $g(r)$, was used to probe the characteristic length scales of the surface features in the AFM images of the P3MT brush films.[79,80] The $g(r)$ between two points on a surface separated by radius r is given by

$$g(r) =< [h(x,y) - h(x^{'}, y^{'})]^2 >, \tag{2.1}$$

$$r = \sqrt{(x-x')^2 + (y-y')^2}, \tag{2.2}$$

where$h(x, y)$ is the height at position (x, y). The $g(r)$ functions were first calculated from the AFM topography images and then fit using the phenomenological form

$$g(r) = 2\sigma^2(1 - e^{-(r/\xi)^{2\alpha}}), \tag{2.3}$$

where ξ is the correlation length, α is the Hurst parameter (corresponding to a measure of short-range roughness), and σ is the root-mean-square (RMS) roughness of the surface.

Section 2.4: Electronic Measurements

2.4.1: Conductive AFM (cAFM) Measurements.

Two-terminal current-voltage (I-V) measurements of the P3MT CPB devices fabricated by KTP were performed using the same Asylum AFM system with modified cantilevers of the same model as the tapping mode AFM measurements. The cAFM cantilevers were modified by sputtering alternating layers of Cr and Au (to improve adhesion) using the recipe: 2.5 nm Cr, 5.0 nm Au, 2.5 nm Cr, 10.0 nm Au, 2.5 nm Cr, 35.0 nm Au, 2.5 nm Cr, and 50.0 nm Au, producing conductive tips of radii 30 nm. Conductive measurements were performed in contact mode by applying a minimum force to make electrical contact to the top Au electrode (< 100 nN). The voltage bias was applied across the CPB device between the ITO substrate (positive bias) and the top Au electrode. Voltages were typically swept between -1 V and +1 V over 10 seconds. For each brush film, at least 20 devices were measured. From the I-V measurements, the zero-bias resistance value was obtained from the inverse of the I-V curve slope at zero voltage bias.

CHAPTER 3: P3MT BRUSH STRUCTURE AND MORPHOLOGY

Understanding the morphology of the P3MT brush films is necessary for interpreting the behavior of electronic devices utilizing the films. Here, the structure and morphology of P3MT brush film characteristic surface features and their size and distributions are described and analyzed.

Section 3.1: Bulk Measurements

3.1.1: Brush Density

During brush growth, only the molecules in the seed monolayer which have been initiated by the Pd catalyst are able to grow polymer chains, though a polymer will not necessarily graft to all initiated molecules in the monolayer.[63] An upper limit on the grafting density of polymer chains in the brush film can be determined by measuring the catalyst initiator density. After initiating the seed monolayer, but before polymer growth, the initiated molecules in the monolayer are functionalized with a a ferrocene functional group, which can be detected through cyclic voltammetry (CV).

Using CV measurements, a catalyst initiator density of 1.3 ± 0.2 nm^{-2} was determined,[57] similar to previously reported results.[61,63] However, during polymer growth a color change in the growth solution was observed, with the solution changing from yellow to red and eventually precipitating insoluble P3MT oligomers. This indicates that solution polymerization outside of the desired SCI-KCTP growth occurred. In order for solution polymerization to occur, some of the catalyst must desorb from the seed monolayer before polymerization begins, or transfer from tethered polymer chains to solution during polymer growth, prematurely halting growth for some chains. Therefore, the catalyst initiator density is an upper

limit on the density of polymer chains within the brush.

The density of the polymer near the surface of the substrate can be extracted from the Pd initiator density if it is assumed that all initiated molecules grow polymer chains. Under this assumption, the initiator density corresponds to one chain per 1.3 ± 0.2 nm^2. The spacing between monomers along a P3MT chain is 4 Å.[81] Therefore, near the surface of the substrate, the monomer density (monomers per unit volume) is estimated to be 3.3 ± 0.5 nm^{-3}.

The density of the P3MT brush films was probed using RBS. The summed spectra of repeated RBS runs for a P3MT brush film is shown in figure 3.1. The thickness and composition of the SiO_2 substrate as well as the areal density of the S in the brush were simulated using SIMNRA. An areal density of 100 ± 4 atoms nm^{-2} was found for S, and a thickness of 260 nm and a composition of 1:2 Si:O was found for the SiO_2 layer, in agreement with the substrates specifications. Due to a low number of counts the Br peak was not fit, instead the peak for the expected Br areal density of 4 atoms nm^{-2} (from CV) is shown. Trace amounts of Cl appear in the RBS spectra, which is a byproduct of polymerization that was not fully removed during post-polymerization cleaning of the film. Trace amounts of Pd are also present.

The average brush film thickness for the sample, 36 ± 2 nm, was measured using scratch AFM profilometry (determining brush thickness by AFM is discussed in detail below). A P3MT brush density of 0.36 g/cm^3 was determined. For the RBS result shown in Figure 3.1, the monomer density (number of monomers per unit volume) was found to be 2.8 ± 0.4 nm^{-3}, compared to a monomer density of 5 nm^{-3} previously reported for the P3HT films.[72]

The degree of polymerization of P3MT brushes can not be estimated by measuring the ratio of the areal densities of S and Br as has been reported previously for P3HT films. Br atoms are not only present at the terminated end of individual polymer chains in P3MT brushes, but are also present on the uninitiated molecules in the seed monolayer, and so there is not one Br per polymer chain.

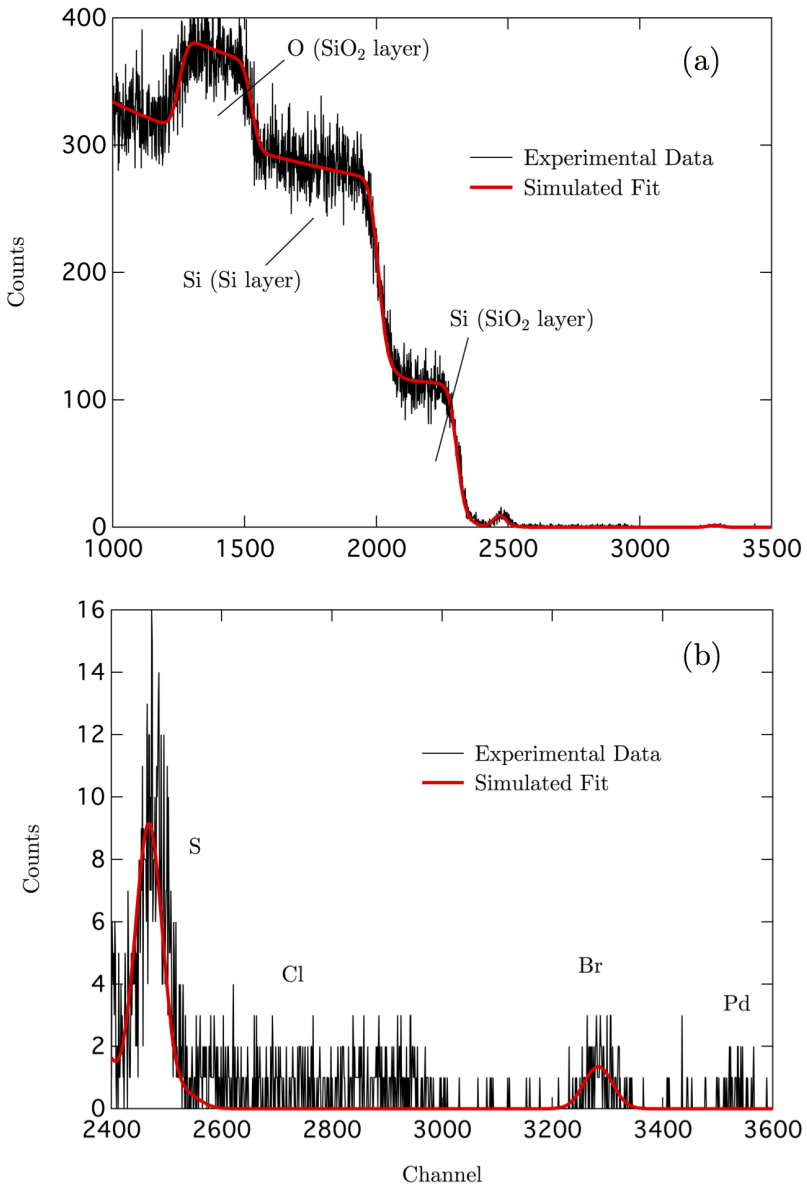

Figure 3.1: (a) The summed spectra of two RBS runs on the same 36 nm sample is shown, along with the SIMNRA fit for elemental composition on the brush and substrate. A thickness of 260 nm and a composition of 1:2 Si:O was found for the SiO_2 layer, in agreement with the substrates specifications. (b) The RBS spectrum zoomed into the channels corresponding to elements found in the brush. An areal density of 100 $\pm$ 4 atoms nm^{-2} was extracted for S. The Br peak was not fit due to low statistics, instead the expected areal density of 4 atoms nm^{-2} is shown. Trace amounts of Cl and Pd are present. Cl is a byproduct of P3MT polymerization, and Pd is present in the catalyst used for polymerization.

GIWAXS measurements on P3MT conjugated polymer brush (CPB) films of 30 and 120 nm thickness detected polycrystalline diffraction arcs at reciprocal space vectors q = 1.2

and 1.8 $Å^{-1}$, while the measurement of thinner films yielded negligible diffraction intensities (Figure 3.2). The two arcs can be assigned to the (020) and (110) reflections respectively, based on a crystal structure with staggered sheets (π-π and lamellar lattice spacing of 3.5 and 7.7 Å, respectively).[77] The π-π and lamellar lattice spacings extracted from GIWAXS agree with previously reported values.[77] The two lattice vectors are orthogonal to the chain axis and exhibit a nearly isotropic distribution with a small amount of horizontal texture (Figure 3.3).

The lattice spacing of thiophene along the chain axis is 4 Å.[81] Together with the π-π and lamellar lattice spacing a monomer unit cell volume can be calculated for crystalline P3MT within the brush. The monomer unit cell has a volume of 0.11 nm^3, and correspondingly, the monomer density of crystalline P3MT within the brush is 9.3 nm^{-3}.

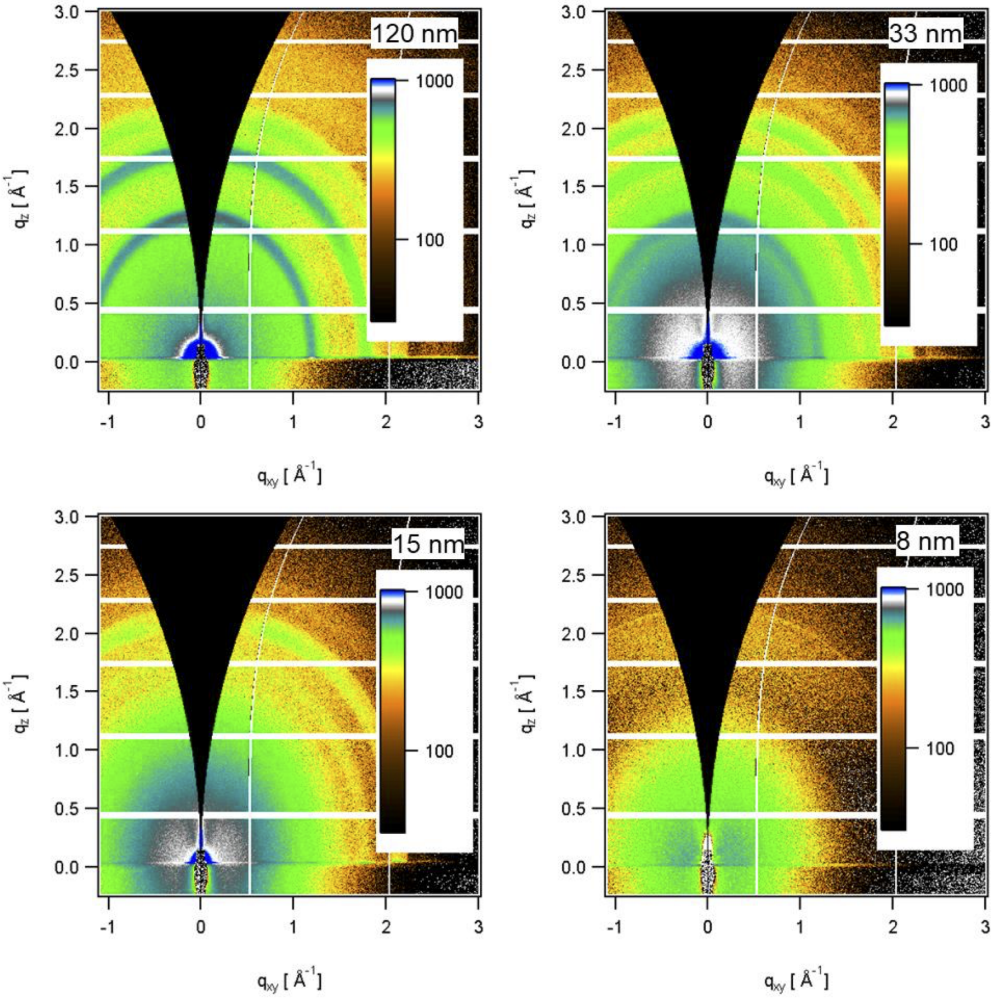

Figure 3.2: GIWAXS images of 120, 30, 15, and 8 nm thick P3MT CPB films grown on ITO. The black region is the "missing wedge" that arises due to kinematic constraints in the GIWAXS geometry. White bars are missing data due to the structure of the detector. Features at 1.2 and 1.8 Å^{-1} are attributed to diffraction from the respective (110) and (020) reflections of P3MT. Other features are attributed to diffraction from ITO, e.g. (222) reflection at 2.1 Å^{-1}.[77] Figure S4 in Ref [54], reproduced with permission.

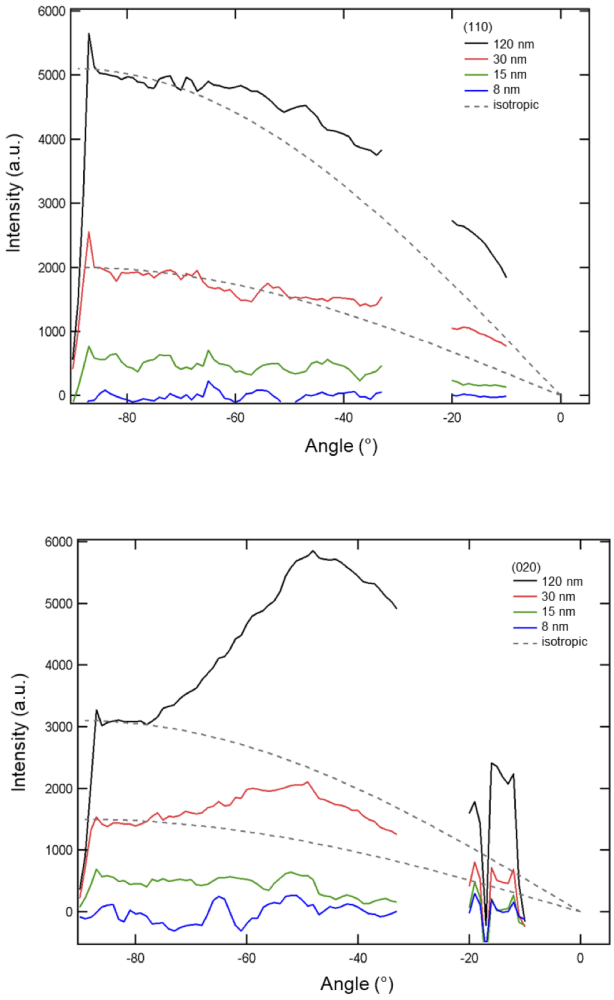

Figure 3.3: (a) Pole figure ($\sin(\omega)$ weighted integral) for the (110) diffraction feature of P3MT CPB films at 1.2 Å^{-1}. Gaps are due to detector structure. Diffraction intensities are detected for films $\geq$ 30 nm thick. Dashed lines indicate the expected behaviors of isotropic systems. The 33 and 100 nm thick films exhibit light textures for orientation $\sim 30°$ from the surface normal. (b) Pole figure ($\sin(\omega)$ weighted integral) for the (020) diffraction feature of P3MT CPB films at 1.8 Å^{-1}. Diffraction intensities are detected for films $\geq$ 30 nm thick. Dashed lines indicate the expected behaviors of isotropic systems. The 33 and 100 nm thick films exhibit textures for orientation $\sim 50°$ from the surface normal. Figures S5 and S6 in Ref [54], reproduced with permission.

3.1.2: Polymer Chain Orientation within the Brush

Using the angular preference for the two lattice vectors (020) and (110) from GIWAXS, a preferred orientation for chains within crystalline regions of the brush can be obtained. The pole figures show a slight preference for the (020) and (110) reciprocal vectors at 50° and 30° relative to the surface normal. The angle between (020) and (110) for a crystalline structure with staggered sheets is 42° in reciprocal space. Additionally, the (001) lattice vector, which points along the chain's backbone in real space, is perpendicular to both (020) and (110) in reciprocal space. These constraints generate the following system of equations

$$\hat{z} \cdot \hat{p} = \cos(50°), \tag{3.1}$$

$$\hat{z} \cdot \hat{l} = \cos(30°), \tag{3.2}$$

$$\hat{p} \cdot \hat{l} = \cos(42°), \tag{3.3}$$

$$\hat{c} = \hat{p} \times \hat{l}, \tag{3.4}$$

$$\hat{c} \cdot \hat{z} = \cos(\phi), \tag{3.5}$$

where $\hat{z}$ is perpendicular to the substrate, $\hat{p}$ is in the (010) direction,$\hat{l}$ is in the (100) direction, $\hat{c}$ is a unit vector in the (001) direction, and ϕ is the angle between the preferred chain direction and the substrate normal. Solving this system of equations gives ϕ of 70°, indicating that polymer chains within the crystalline regions tend to have a slight horizontal preference. For comparison, $\phi = 0°$ corresponds to orientations parallel to the substrate, while $\phi = 90°$ corresponds to orientations perpendicular to the substrate. However, GIWAX indicates that there is a very low degree of crystallinity in the brush, and within the crystalline regions chains have a weak orientation preference, so ϕ is not indicative of average chain orientation within the brush.

Normal incidence UV-vis spectroscopy experiments of the films revealed two features at ∼610 and 490 nm in all films, and a third feature at 415 nm in films ≥30 nm thick (Figure

3.4b).[54] The 610 nm peak corresponds to the onset of vibronic series within the brush, while the 490 and 415 nm peaks correspond to absorption by segments of the brush with distinct conjugation lengths.[54] The higher wavelength absorption corresponds to longer conjugation length segments of the brush. The onset of a peak at 415 nm for brushes $\geq$ 30 nm indicates the appearance of shorter conjugated segments within the brush as it grows longer, likely due to increased disorders as the brush grows further away from the substrate.[54]

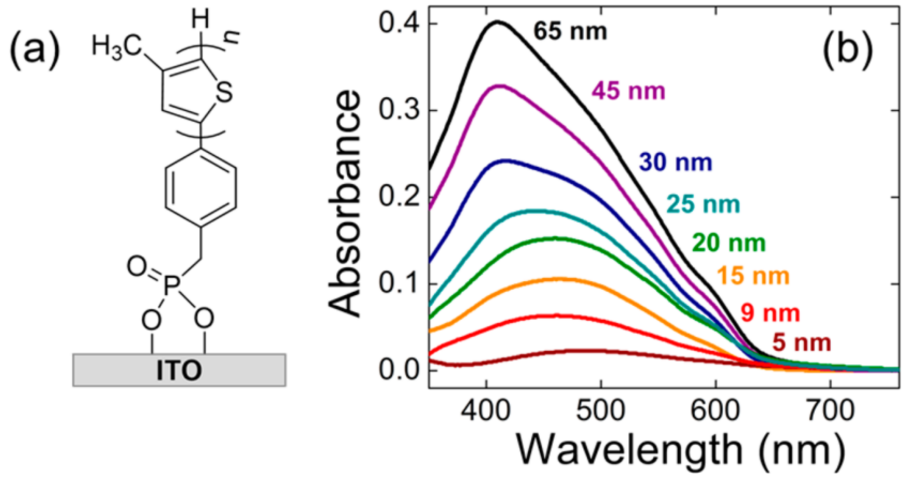

Figure 3.4: (a) Molecular structure of P3MT CPBs grown from ITO. (b) Normal incidence absorption spectra of P3MT CPB films of various thicknesses. Figure 1 in Ref [54], reproduced with permission.

Optical anisotropy in P3MT brush films was investigated using polarized UV-vis measurements at a 60° incident angle.[54] At this angle, the p polarization couples strongly to the transition dipole along the polymer backbone of the vertically oriented polymer chains,[82] while the s polarization couples primarily to the transition dipole of horizontally oriented polymer chains. Thus, the dichroic ratio $DR = A_p/A_s$ where A_p and A_s are the maximum intensity of absorption in the p or s polarization respectively, was determined and used to compare the ensemble average orientation of the polymer chains in CPB films as they grow (average orientation given by the tilt angle θ in Figure 3.5a inset).

A higher DR corresponds to more vertical orientation, i.e. a lower θ. The film thickness dependent values of DR at oblique incidence exhibit three distinct regimes (Figure 3.5a): (i)

a value of ∼0.6 for thickness <10 nm, (ii) an increase in the DR between 10 and 30 nm to a maximum of ∼1.2, and (iii) a decrease in the DR in films >30 nm thick to a value slightly greater than 1. Note that the DR for the P3MT brush films at normal incidence is 1 due to the isotropic nature of the films in the plane of the substrate.

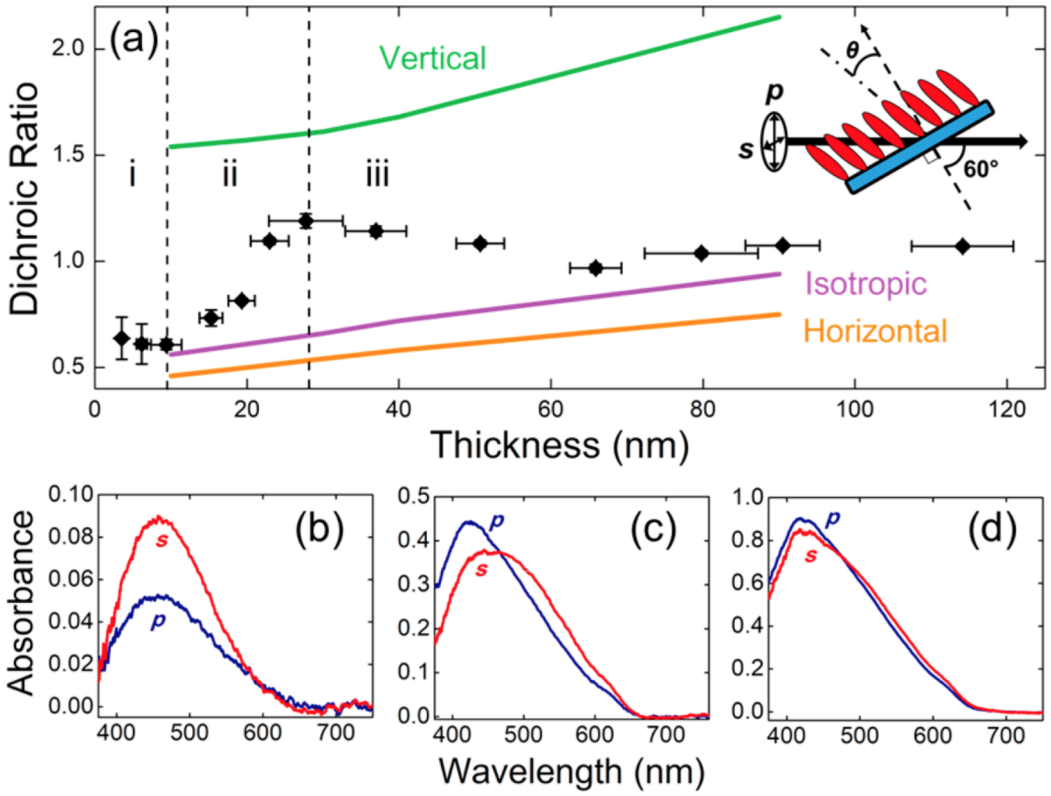

Figure 3.5: (a) Dichroic ratio for P3MT CPB films of various thicknesses, taken at 60° incidence, with distinct growth regimes as labeled. Also shown are modeled spectra for nominally horizontal (orange), isotropic (purple), and vertical (green) orientations. Inset: experimental geometry for the polarized UV-vis measurements at an incident angle of 60°. θ denotes the tilt angle of monomers from the surface normal. (b-d) Polarized absorbance spectra of 10, 30, and 90 nm thick P3MT CPB films, respectively, at 60° incidence. Figure 2 in Ref [54], reproduced with permission.

Section 3.2: P3MT Brush Surface Morphology

3.2.1: Analysis of Surface Structure by AFM and SEM

AFM topography images of P3MT brush films have been analyzed in previous work, primarily for estimating film thickness and qualitative assessment of their surface structures.[60,61] In this work, the surface structure and morphology of the brush films have been examined qualitatively and quantitatively using AFM images, including the size and shape of surface features and their distributions. The surfaces of the P3MT brush films consist of round columns with smooth and rounded tops, rising above a rough polymer network (Figure 3.6). The heights of the columns vary significantly, with the tallest extending well over 100 nm above the surrounding area in the film. Scanning electron microscope images of the films are consistent with the formation of columns and an underlying polymer network (Figure 3.7).

3.2.2: Quantifying Brush Thickness

The surface roughness of thin films is often much smaller than the total thickness of the film, and thus defining the film thickness is straightforward. Thickness can be determined through AFM scratch profilomtery, where the film is scratched, revealing the substrate, and a step height between the substrate and film height can be measured. Figure 3.8 demonstrates the scratch profilomtery technique used on spin cast P3HT film. Histograms of the substrate and film heights are obtained, and film thickness is defined as the distance from the peak of the substrate height distribution to the peak of the film height distribution. For films such as spin cast P3HT, where the surface roughness is much lower than the peak-to-peak thickness determined by scratch profilometry, film thickness is well defined and easily interpreted.

The height distribution of P3MT films is characteristically different than spin cast films. The brush height distribution follows a log-normal shape due to the fundamentally different morphology of the brush (i.e. the presence of columns). A demonstration of scratch profilometry on a brush film is shown in Figure 3.9. The roughness of the brush surface is large

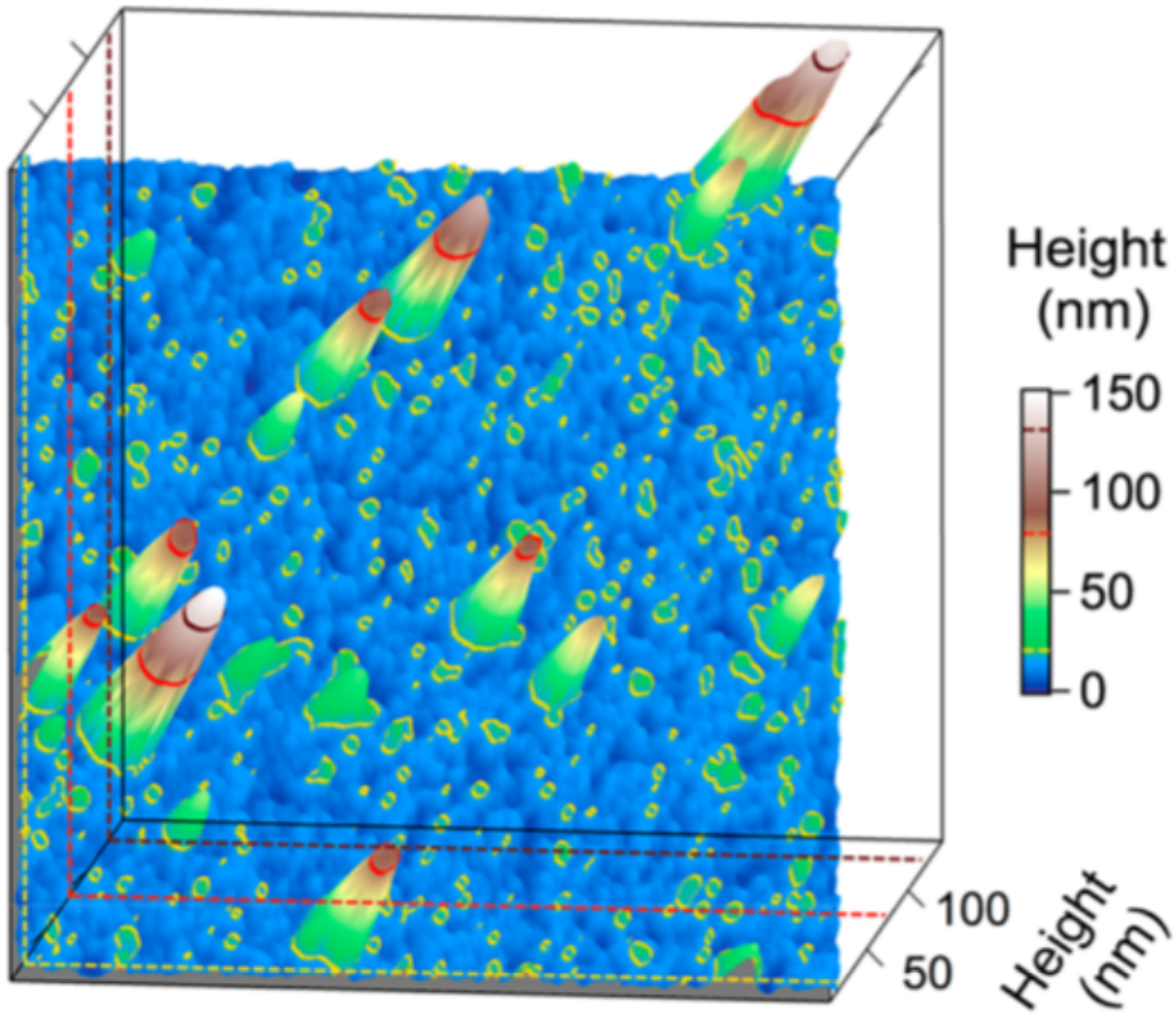

Figure 3.6: Typical 3D rendered AFM topography image of a 15 nm thick P3MT CPB film and its characteristic features. The yellow, red, and brown dashed lines and ribbons correspond to respective heights of 20, 80, and 130 nm. The image dimensions in panel a are 3 μm x 3 μm, taken from a larger, 10 μm x 10 μm AFM image. Figure 3a in Ref [54], reproduced with permission.

compared to the peak to peak separation. The full-width-at-half-maximum (FWHM) of the distributions is very broad, about half of the film thickness (Figures 3.10 and 3.11).

Brush thickness, the peak to peak height determined from scratch profilometry, increases as a function of brush growth time at a rate of $\sim$5 nm per hour. Columns are observed on brush samples regardless of growth time. To determine when columns begin to form, a set of 'short' growth time brushes were synthesized. All of the short growth time brushes

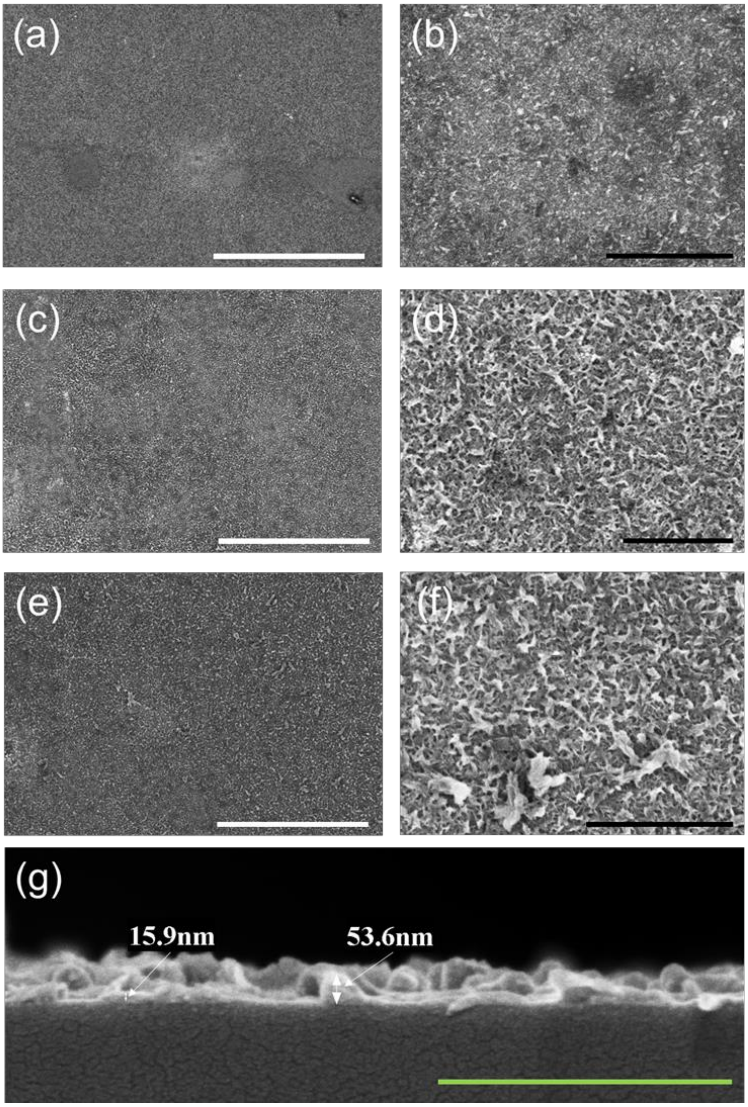

Figure 3.7: SEM images of (a), (b) 15 nm, (c), (d) 30 nm, and (e), (f) 55 nm thick P3MT CPB films. White scale bars are 5 μm, black scale bars are 1 μm. (g) SEM cross-section of a 15 nm thick P3MT CPB film with apparent polymer network and column heights labeled. Green scale bar is 500 nm. Figure S9 in Ref [54], reproduced with permission.

contained columns. The 'shortest' of these brushes underwent growth for 10 seconds and had columns as tall as 50 nm, but also contained areas where little or no apparent growth occurred (Figure 3.12). This implies an initial column growth rate on the order of $\sim$5 nm per second, three orders of magnitude greater than the "average" brush thickness growth rate.

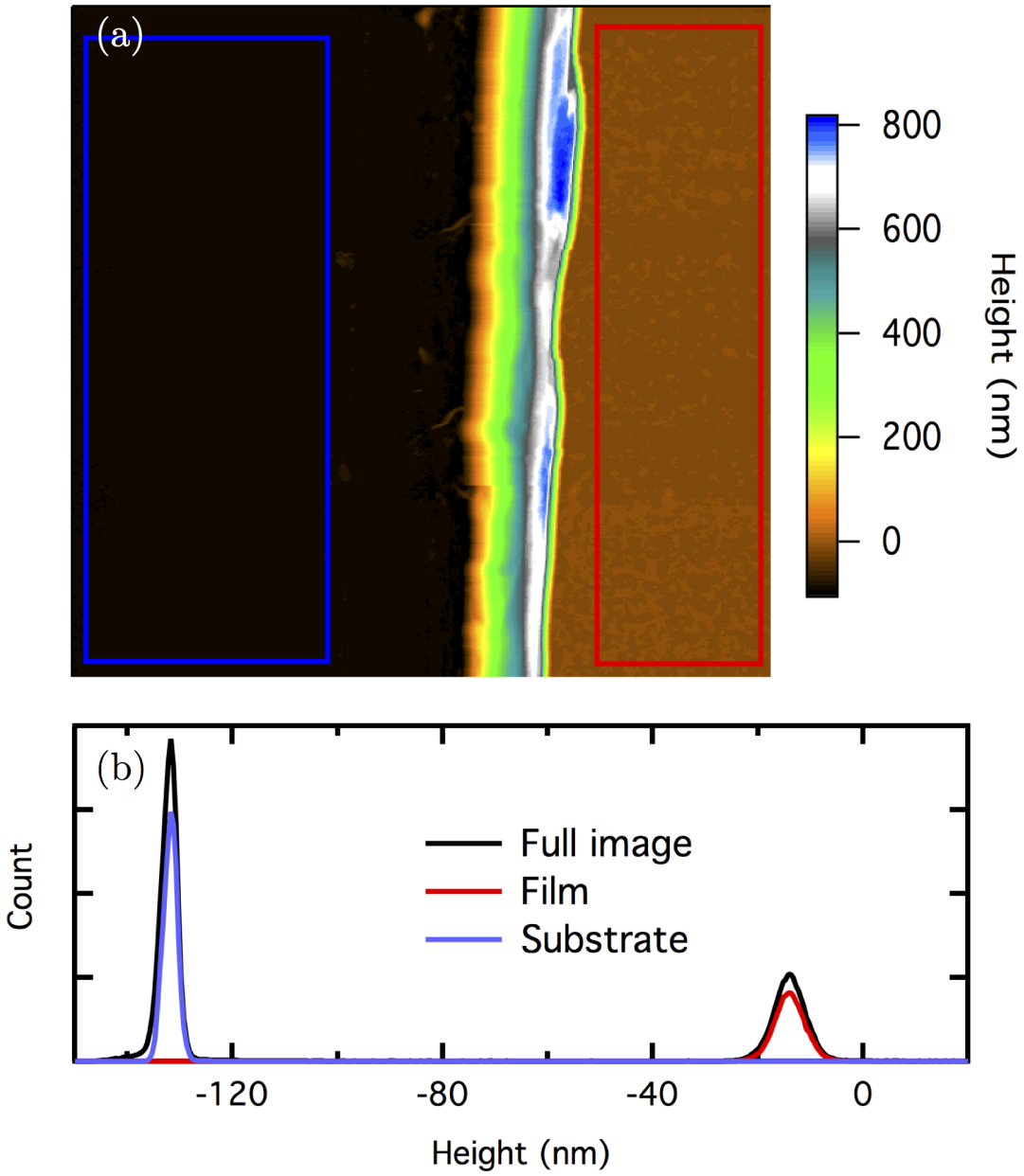

Figure 3.8: Scratch Profilometry on a spun cast P3HT film. (a) AFM topology image of the scratch-exposed and adjacent film. There are three regions in scratch images, a region containing exposed substrate, a region containing undisturbed the film, and a transition region containing residual film and film buildup from the scratching process. The red and blue boxes indicate regions containing only exposed substrate and undisturbed film respectively, excluding the transition region. (b) A height histogram created from (a). The black curve corresponds to the histogram of the entire image, while the red and blue curves correspond to histograms of the regions inside the read and blue boxes in (a). The peak to peak thickness is 117 $\pm$ 2 nm.

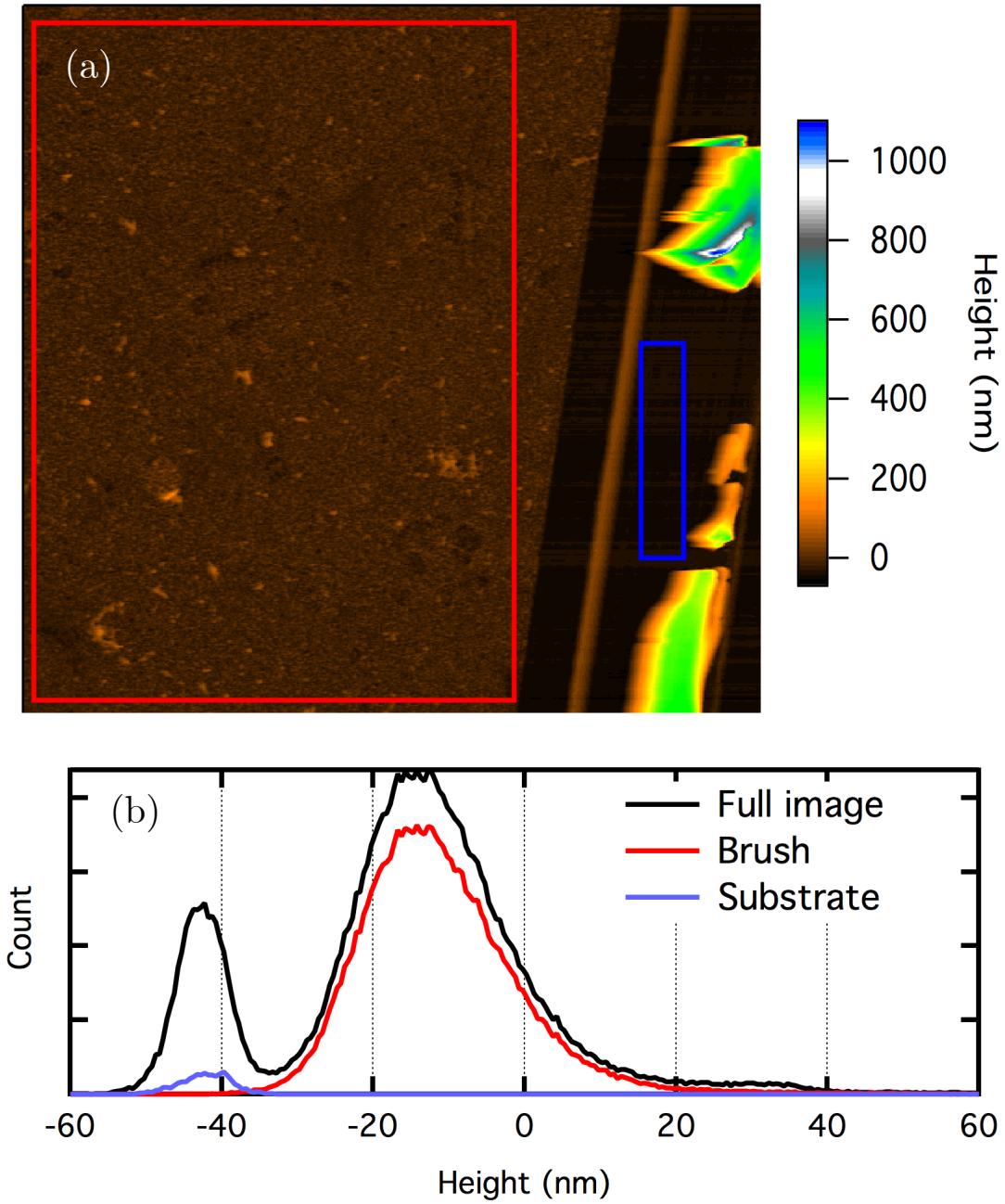

Figure 3.9: Scratch profilometry on a P3MT brush film. (a) AFM topology image of the scratch-exposed and adjacent film. (b) A height distribution created from (a). The full width-at-half-maximum of the height distribution is roughly half of the peak to peak film thickness. The peak to peak thickness is 30 ± 2 nm.

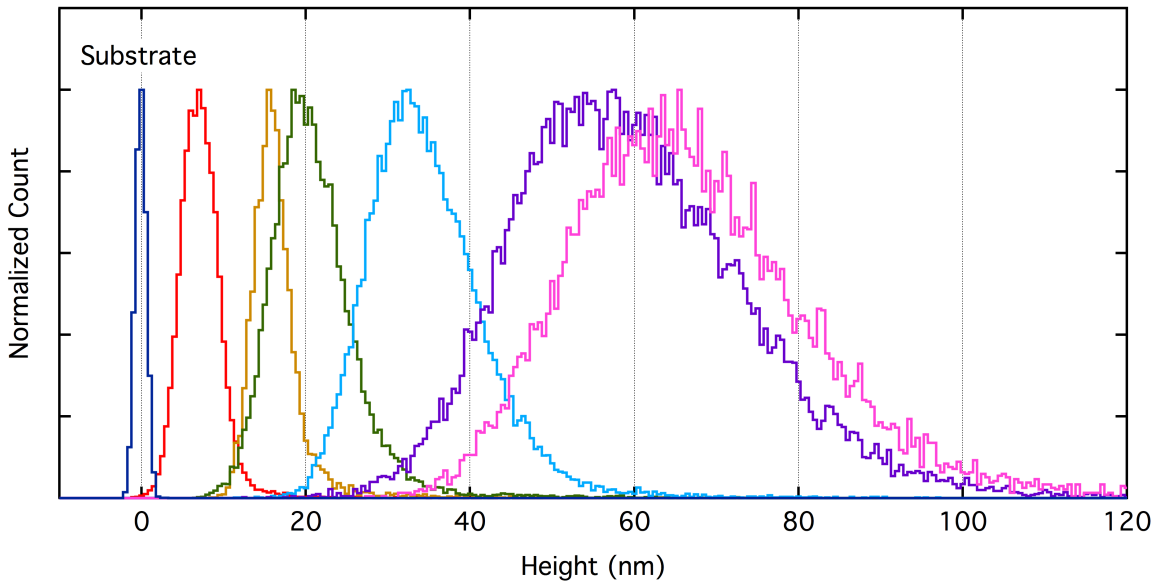

Figure 3.10: Comparison of P3MT height distributions for various brush film thicknesses. The height distributions are log-normal. The width of the distribution increases with film thickness and the FWHM of the distribution is roughly 1/2 film thickness.

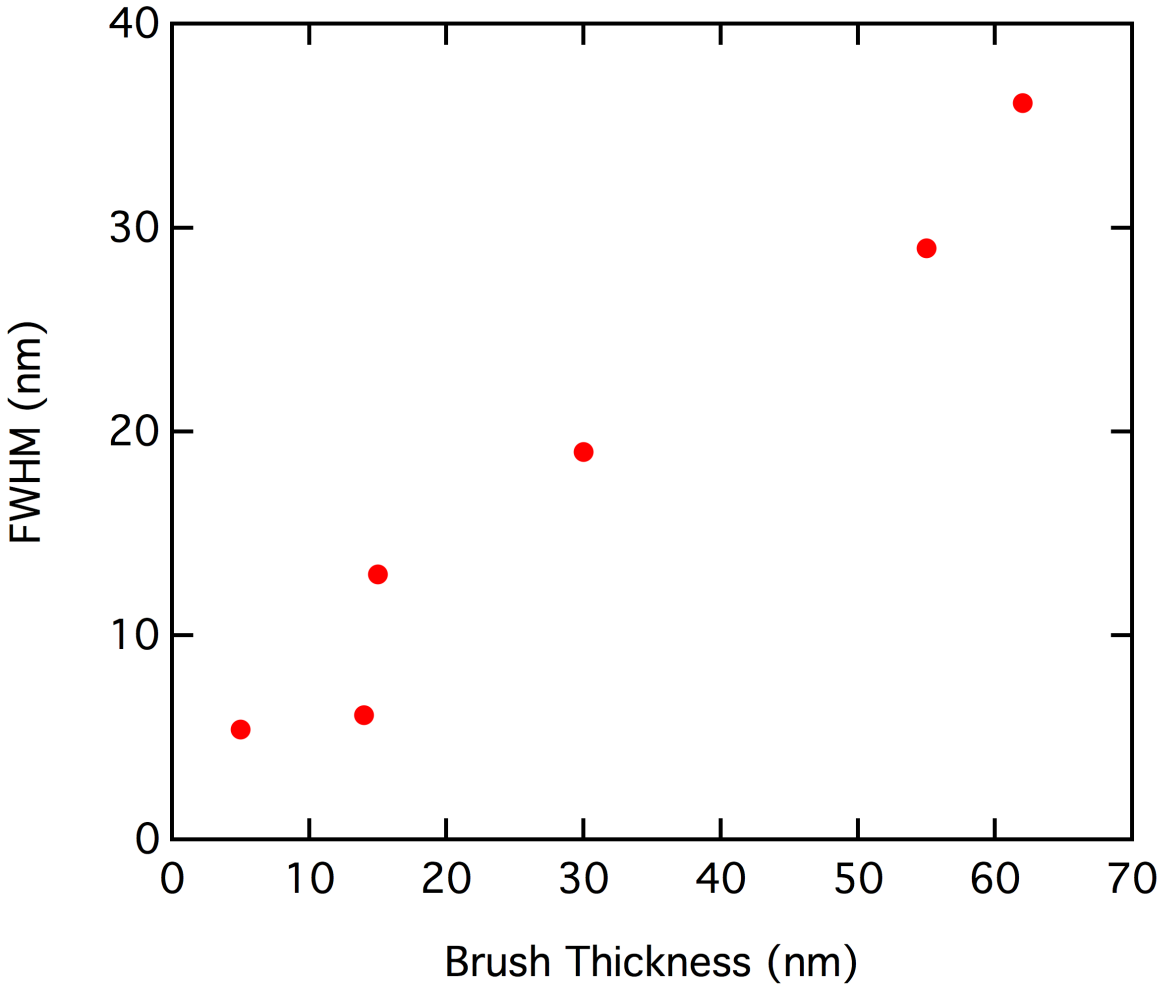

Figure 3.11: Full-width-at-half-maximum of brush height distribution vs. brush thickness. The FWHM increases with thickness, and is roughly half of the brush thickness.

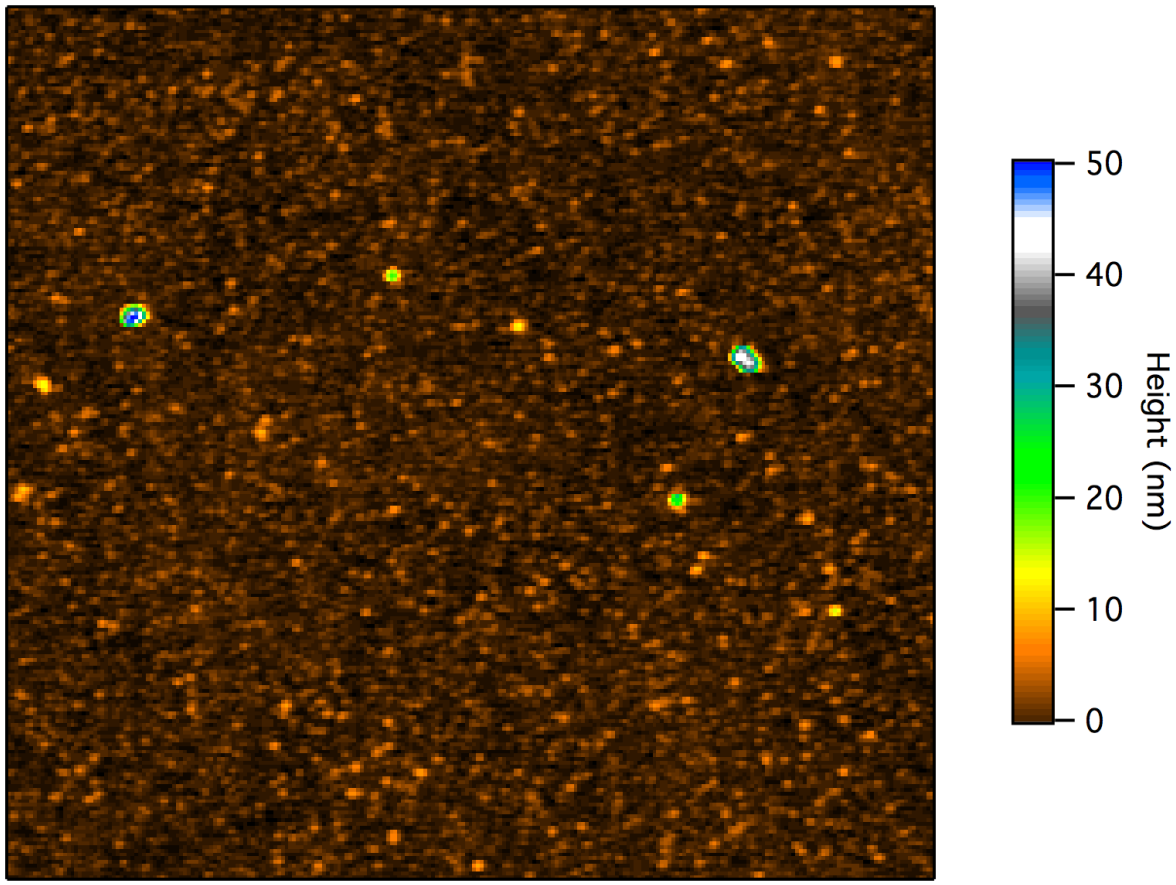

Figure 3.12: AFM image of a very short growth time (10 s) P3MT brush (5μm x 5μm). While much of the substrate appears to have little brush growth, columns as tall as 50 nm have formed in some areas.

3.2.3: Column Analysis

The column areal density and cross-sectional area were analyzed as a function of brush thickness using the AFM images. The tall columns are of particular interest because they are the ones contacting the electrodes in brush devices and thus primarily responsible for the charge transport processes (see Section 4). The columns also provide insight into the growth mechanism of the P3MT brush films, and identifying these columns systematically is necessary for quantifying their properties (i.e. areal density, height distribution, cross sectional area, etc.). A procedure for identifying columns must be defined in order for these properties to be studied systematically.

Columns are identified by taking slices of AFM images at various "threshold heights". For each threshold height, there is a corresponding threshold surface (i.e. the part of the surface above the height), which contains a certain fraction of the film surface area (i.e. pixels in the image), defined as the "area fraction." For example, for the 15 nm thick CPB film shown in Figure 3.6, 0.1% of the surface area is taller than 130 nm (brown ribbons and lines), while 1% (red ribbons and lines) and 10% (yellow ribbons and lines) of the areas are above respective heights of 80 and 20 nm. Each continuous set of pixels within the AFM image above the threshold height corresponds to a column.

Column Identification Algorithm The algorithm for identifying columns at a given threshold height is as follows. Each AFM image consists of a two dimensional array of pixels, each containing a height value. First, a 'column mask' array corresponding to the AFM image is created with the same dimensions as the AFM image and all values initially set to 0, and a column counter variable (which contains the number of columns identified in the image) is created and set to 0. The column mask is a mask that defines which column a pixel belongs to, if it belongs to any column. After the algorithm is complete, the nth column identified by the algorithm corresponds to pixels in the mask which have the value n. Pixels with a value of 0 are not within any column. Once the column mask and column counter have been initialized the main loop of the identification algorithm begins.

In the main loop of the program, each pixel in the column mask is sequentially checked. If the value of the current pixel in the column mask is not 0, and the corresponding pixel in the AFM image already belongs to a column (as explained below), and the algorithm moves on to the next pixel in the mask. If the pixel value is 0 then the algorithm checks the height of the corresponding pixel in the AFM image. If the height is below the threshold value then the current pixel is not part of a column and the algorithm continues to the next pixel. If the height is greater than the threshold height then pixel belongs to a new column, and the column flood-fill subroutine begins.

Given a starting pixel and a threshold height, the column "flood-fill" subroutine of the program finds all connected pixels which are above the threshold height. This group of contiguous pixels belong to the same column. The flood fill algorithm works by examining all the adjacent pixels to the currently observed pixel. If any of the adjacent pixels are above the threshold, but have not yet been determined to be part of the current column their corresponding pixel in the column mask is set to n (the number of the column) and the pixel is added to a queue of pixels that need to be "checked". Each pixel in the queue is checked sequentially, and more pixels are added to the end of the queue when more pixels above the threshold are found. Eventually the edges of the column will be reached, no more pixels will be added to the queue, and the queue will be emptied. Once this happens all pixels within the column have been identified, the column counter is incremented and the algorithm returns to the main loop.

The program finishes once all pixels have been checked. The column counter contains the total number of columns found, and the properties of the nth column can be examined by looking at pixels in the AFM image which correspond to pixels of value n in the column mask. An implementation of the column identification algorithm in the IgorPro scripting language is given in the Appendix (A).

The threshold height given to the column identification algorithm determines which columns are identified. Threshold heights that corresponds to a small area fraction are

used to probe the parameters of tall columns, whereas the larger area fractions are used to analyze the short and the tall columns combined. If the threshold height is too low, columns may connect and the algorithm will start to identify multiple columns as a single column. This problem is compounded by the spatial extent of the AFM tip, because AFM can not resolve valleys in the brush that are smaller than the size of its tip (Figure 3.15). An example of column masks generated at various thresholds for an AFM image is shown in Figure 3.13.

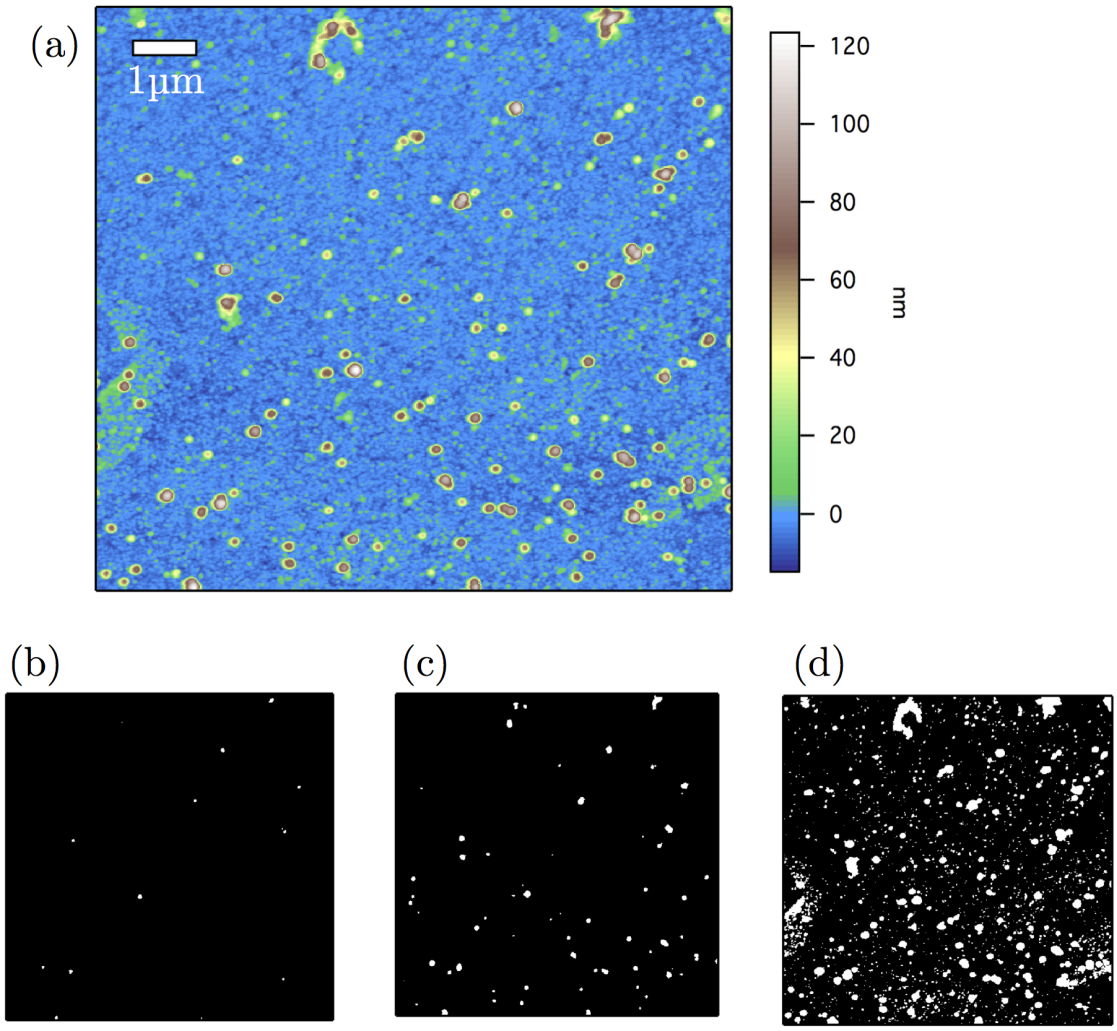

Figure 3.13: Column masks generated by the column identification algorithm at various threshold heights for a 15 nm thick CPB film. Lower thresholds identify more columns, and at the lowest thresholds columns begin to be merged by the algorithm. (a) AFM image. (b) Column mask with a threshold height of 121 nm (0.1% area fraction). (c) Column mask with a threshold height of 86 nm (1% area fraction). (d) Column mask with a threshold height of 22 nm (10% area fraction).

Column Areal Density and Cross Section. Once columns are identified by the column identification program, their areal density (column per μm^2) and cross sectional area are determined. Since the number of columns identified by the identification algorithm depends on the area fraction (threshold height) used, column areal density was measured as function of area fraction. Column areal density was measured at three area fractions for each

AFM image, 0.1%, 1%, and 10%. The areal density of columns found at each area fraction for brushes of various thicknesses is shown in Figure 3.14.

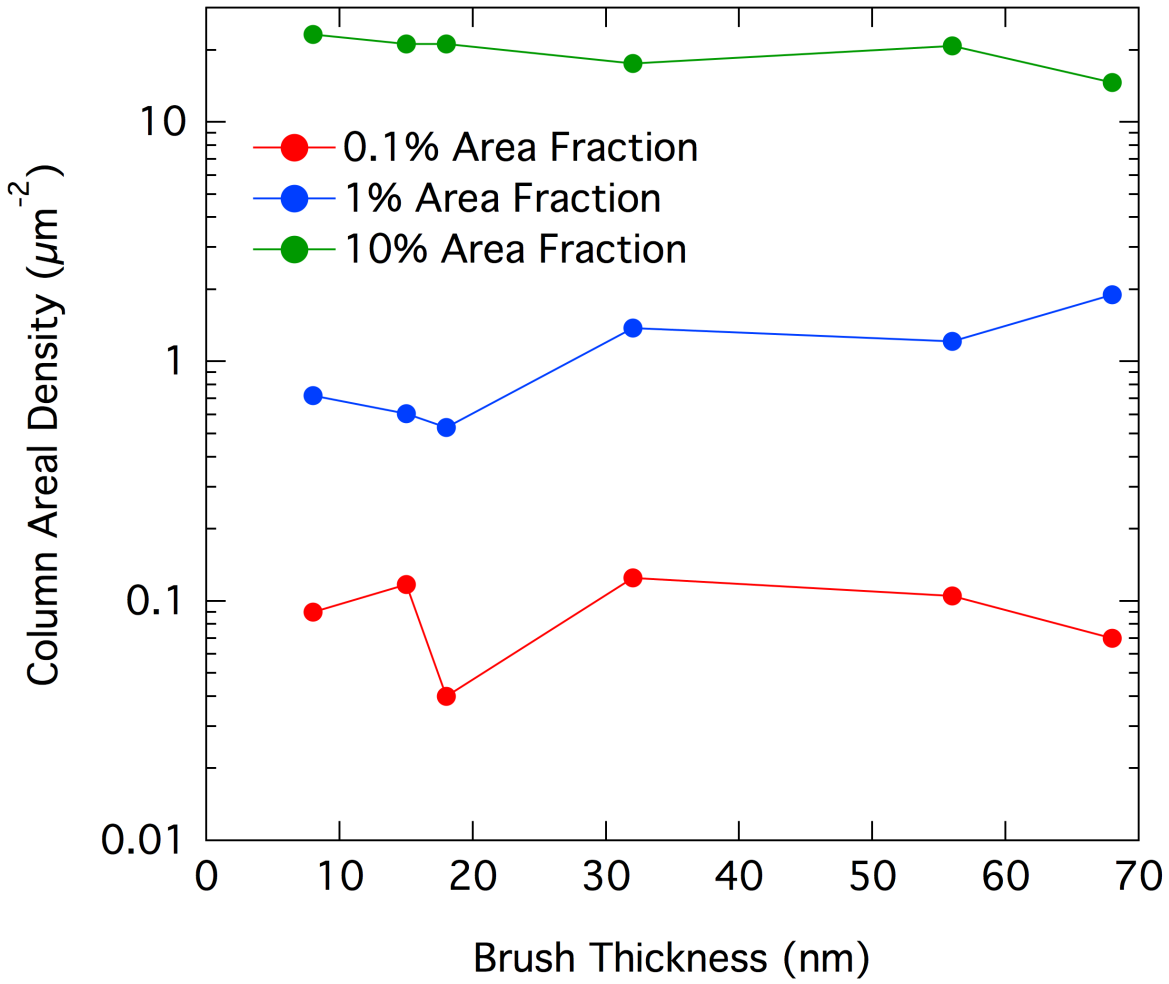

Figure 3.14: Column areal density at various area fractions vs. brush thickness. The areal density for a given area fraction and does not depend on film thickness.

The cross sectional area of columns was also measured as a function of area fraction. The cross-sectional area of columns was measured a fixed height below the highest point of each column. This is done by running the column" flood-fill" subroutine of the program starting with the tallest pixel in each identified column at a threshold height and a fixed height below the tallest point. For the analysis presented here, the fixed height was chosen to be 1/4 of the film thickness. Measurement of the column area much further down the column (e.g. half of the column height) or at the very top of the columns does not yield reliable results

based on several considerations. First, the columns appear to be connected at the bottom of the film by a polymer network that is above the ITO surface, as shown in SEM and AFM images. Because the columns are densely packed and often very tall compared to the average thickness of the film, the base of each column, the heights of the columns above the underlying polymer network, and the spaces between columns, are not completely resolved by the AFM measurements. As a result, when using the height from the ITO surface to the highest point to define the column heights, the half-height for many of the columns is below the resolved height level, causing erroneous estimates of column area.

However, finding the correct threshold to measure column cross-sectional area is difficult. Since the columns have rounded tops, measuring too close to the top would underestimate the area. Due to measurement artifacts such as the AFM tip geometry (Figure 3.15), as the column sides become steep they are no longer fully resolvable by the AFM and so their cross-sectional area is overestimated if measured too far down the columns. If the areas of columns were measured right at the various height thresholds (e.g. along the ribbons in Figure 3.6), the same column may yield different areas at different heights, and columns of significantly different heights may erroneously appear to have different cross-sectional areas only because one is shorter than the other. Therefore, a reasonable choice to normalize the comparison of columns in the same or different films would be to identify columns above a certain height threshold using area fractions, then use a fixed height below the column peaks to measure the column cross-sectional area between the heights that would result in over/underestimation of the area (Figure 3.16). 1/4 of the film thickness is a natural choice for this height, as it corresponds to roughly the half-width of the distribution for films of all thicknesses. Other similar heights were used, and they do not qualitatively change the results of the analysis. The choice of this definition is primarily due to the convolution between the AFM tip and the columns, which causes increasing overestimation of the column cross-section area as the tip moves further down the sides of the columns.

The AFM topography measurements indicate that the columns form nearly instanta-

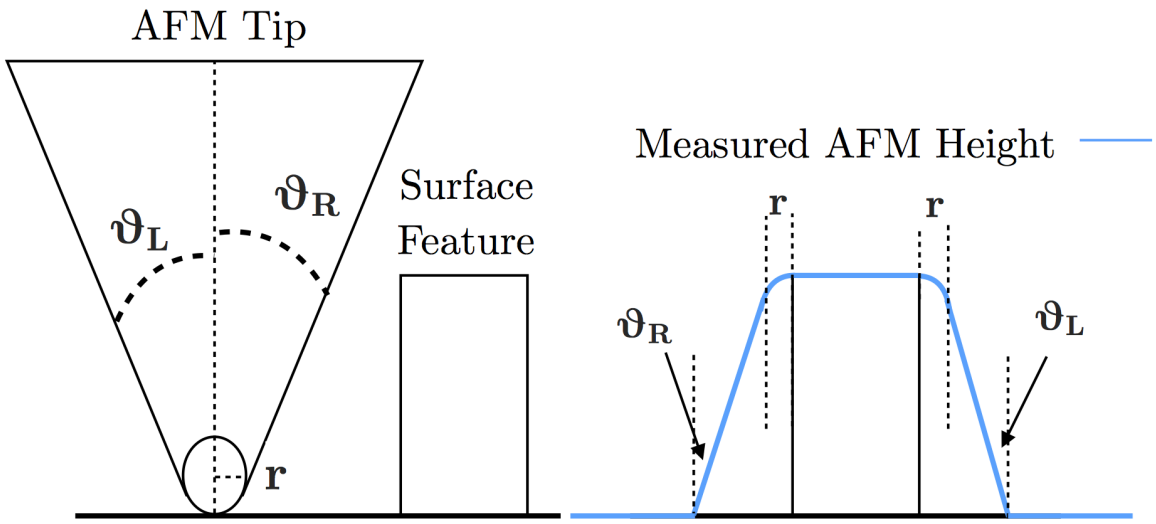

Figure 3.15: AFM tip convolution with surface features. Tip shape is defined by two half-cone angles (θ_R and θ_L) and a tip radius (r). The size of features that are 'sharper' than the tip is overestimated.

neously in the film growth and exhibit a characteristic size and distribution. Specifically, taller and shorter columns have the same characteristic area. For the 15 nm thick film shown in Figure 3.17a, the peaks of the column area distributions at various area fractions are all about 2.1 x 10^{-3} μm^2 with FWHM values of ~1 x 10^{-3} μm^2. Analyses of 32 and 55 nm thick brush films are also shown in Figures 3.18 and 3.19.

Comparing between columns in films of different thicknesses, the characteristic column area and its distribution are nearly independent of the film thickness (≥6 nm), with an average value of (2.3 ± 0.6) x 10^{-3} μm^2 (Figure 3.17b). The height-dependent column areal density exhibits a linear dependence on the area fraction over several orders of magnitude and is also independent of film thickness (open symbols in Figure 3.20), consistent with the observation of a characteristic column area described above. The column density can be extrapolated to 100% area (i.e. the entire topography image) to yield a value of 200 ± 50 μm^{-2}, corresponding to a characteristic areal density of columns in the P3MT brush films. Note that the spread of density values for films of different thicknesses at low area fractions (≤1%) is likely the result of low sampling statistics of columns.

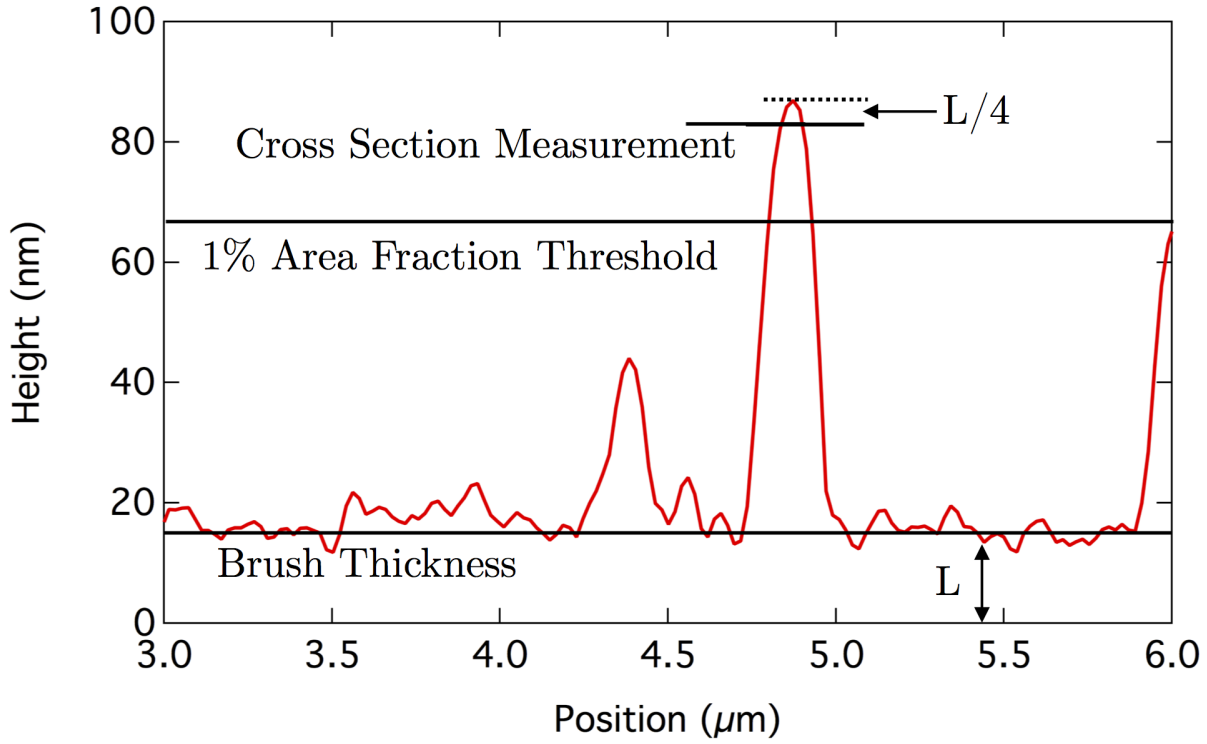

Figure 3.16: Visualization of the column cross section measurement. A height profile from an AFM image of a 15 nm brush is shown. Columns are identified with the column identification algorithm at a given threshold (1% area fraction). The cross sectional area is not determined by the cross section at the given threshold, but a fixed distance from the top of the column (1/4 brush thickness).

Height-height correlation function analysis has been preformed on the AFM topographical images. Results show the thickness independent values for the correlation length and Hurst parameter, with respective values of 70 ± 20 nm and 0.71 ± 0.08, and roughness values that depend linearly on film thickness (consistent with the result shown in Figure 3.11). The correlation length directly probes the characteristic size or separation of surface features;[80] as such, the inverse square of the correlation length corresponds to an areal density of surface features for the entire image. The densities from this analysis (closed symbols in Figure 3.20c) coincide with the extrapolated values from the column density analysis described above, indicating quantitative consistency between the two analyses.

The value of the Hurst parameter (a measure of short-range surface roughness) corre-

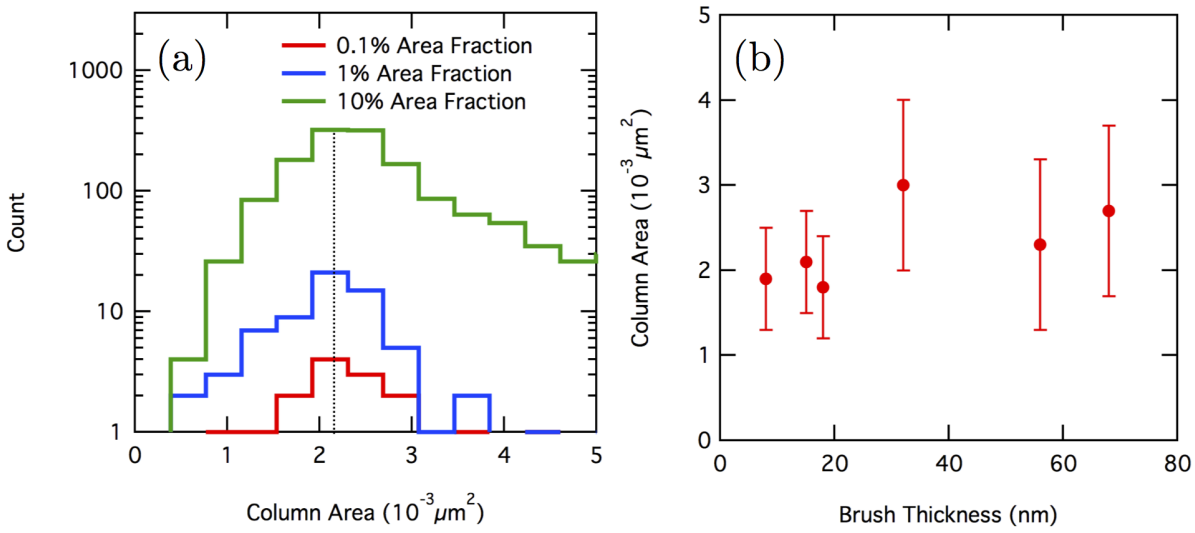

Figure 3.17: (a) The distribution of column cross sectional area for columns at 0.1%, 1%, and 10% area fractions for a 15 nm sample. The peak of the distribution is independent of area fraction used to identify the columns, indicating both large and small columns have the same cross sectional area. The long tail for the 10% area fraction cross section distribution is due to the identification algorithm beginning to pick up merged columns. (b) The peak of the column cross sectional area distribution for films of different thicknesses. Column cross sectional area is independent of brush thickness.

sponds to a relatively smooth surface on short length scales, also consistent with the observed smooth, rounded column tops.[83] A typical height-height correlation function, corresponding fit, and parameters for films of various thicknesses are shown in Figure 3.21 and Table 3.1. The agreement between the column analysis and height-height correlation function analysis indicates that the parameters extracted by both originate from the same features on the surface of the P3MT brush films. The columns therefore do not just account for the long tail in the height distribution of the films but instead comprise a significant portion of the surface area in P3MT brush films. Therefore, it is reasonable to interpret that the height distribution of columns resembles the surface height distributions of the films, with column heights ranging from well above to below the nominal film thickness.

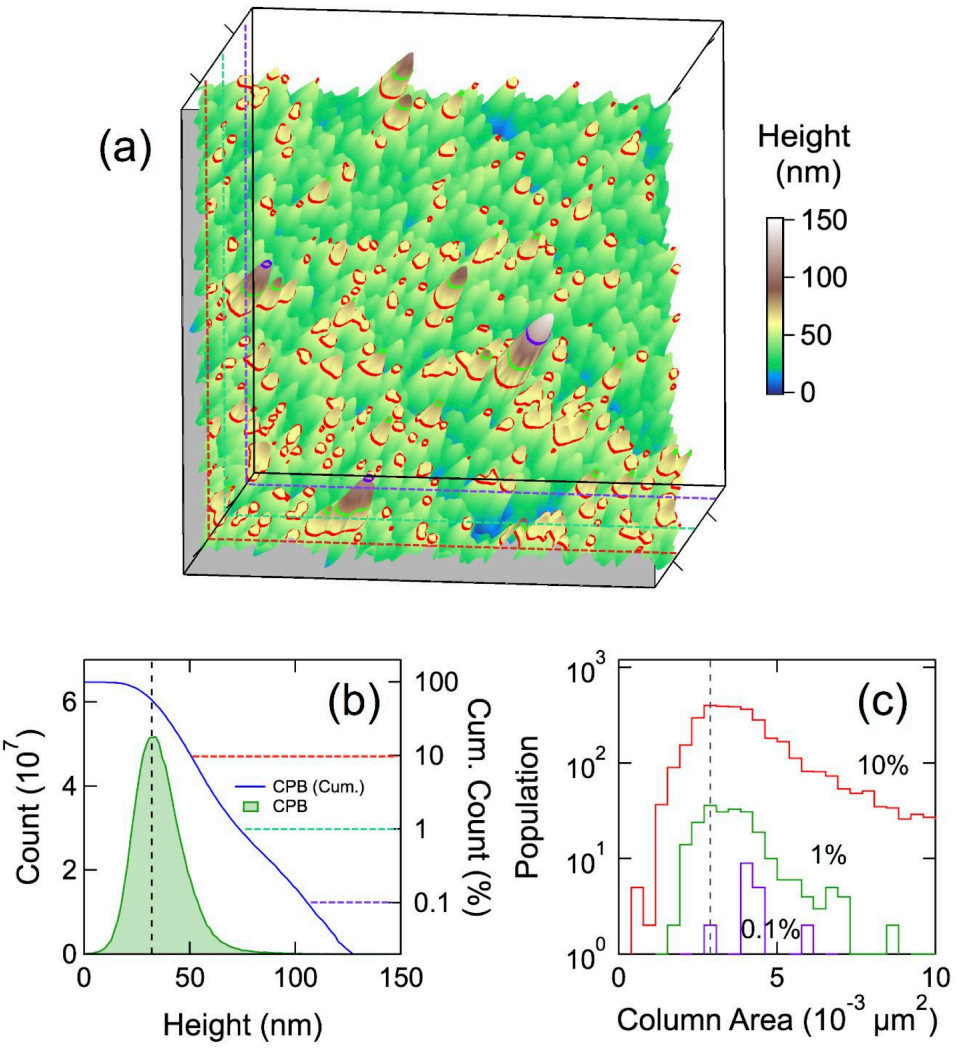

Figure 3.18: Typical AFM topography image of a 32 nm thick P3MT CPB film and its characteristics features. (a) 3D rendered AFM image, with ribbons corresponding to 10% (red, 50 nm height), 1% (green, 73 nm), and 0.1% (purple, 105 nm) area fractions. The image dimensions in (a) are 3 μm x 3 μm, taken from a larger, 10 μm x 10 μm AFM image used to produce (b) and (c). (b) Histogram (green) of an AFM image of the film, and the corresponding normalized cumulative histogram (blue) from the highest point in the image. (c) Distributions of cross-sectional area of columns at several area fractions. Figure S10 in Ref [54], reproduced with permission.

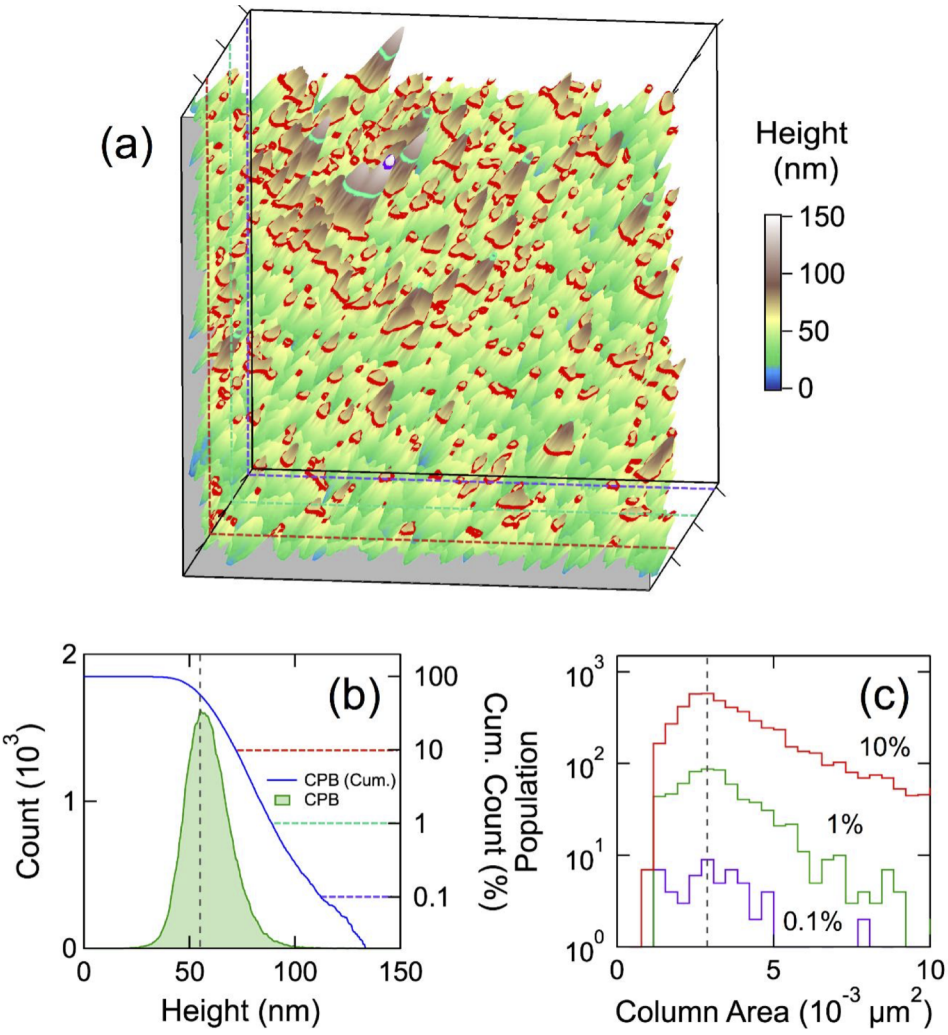

Figure 3.19: Typical AFM topography image of a 55 nm thick P3MT CPB film and its characteristics features. (a) 3D rendered AFM image, with ribbons corresponding to 10% (red, 72 nm height), 1% (green, 89 nm), and 0.1% (purple, 110 nm) area fractions. The image dimensions in (a) are 3 μm x 3 μm, taken from a larger, 10 μm x 10 μm AFM image used to produce (b) and (c). (b) Histogram (green) of an AFM image of the film, and the corresponding normalized cumulative histogram (blue) from the highest point in the image. (c) Distributions of cross-sectional area of columns at several area fractions. Figure S11 in Ref [54], reproduced with permission.

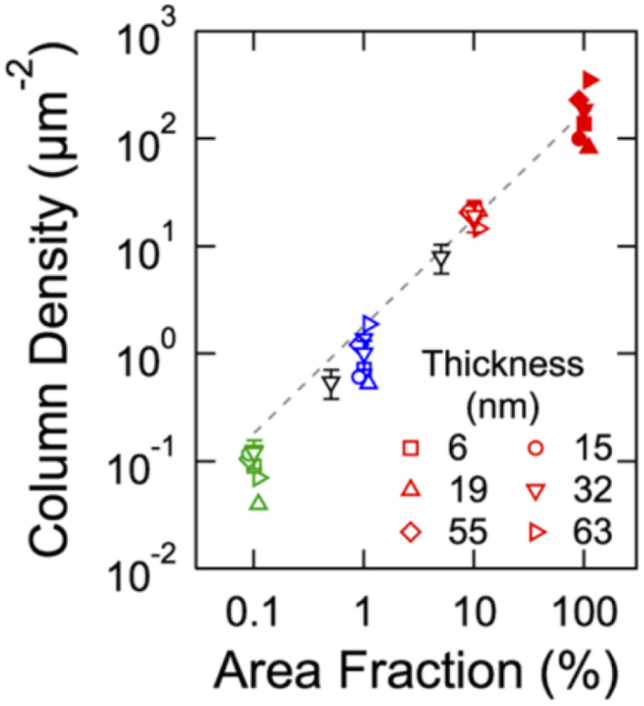

Figure 3.20: Log plot of column density measured at various area fractions (open symbols) and that obtained from the height-height correlation function analysis (closed symbols). Films of different thicknesses are distinguished by symbols. The dashed line is a guide to the eyes to show linearity between the column density and the area fraction. Figure 4c in Ref [54], reproduced with permission.

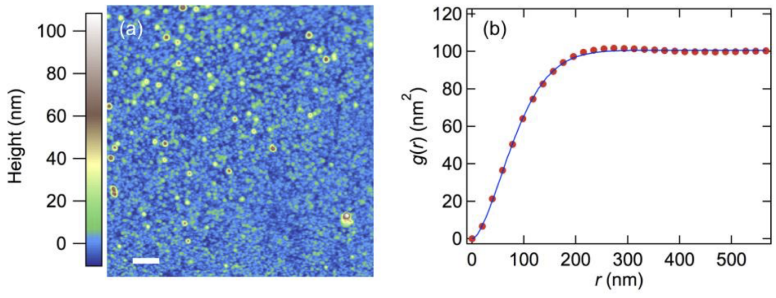

Figure 3.21: (a) AFM topography image (white scale bar is 1 μm) and (b) calculated HHCF in red circles with the empirical fit as the blue line for a 15 nm thick P3MT CPB film. Fit parameters for the film are listed in Table 3.1. Figure S12 in Ref [54], reproduced with permission.

Table 3.1: Representative height-height correlation function results for P3MT CPB films.

Brush Thickness	Correlation Length (nm)	Hurst Parameter	RMS Roughness (nm)
8	85 ± 1	0.73 ± 0.04	5 ± 1
15	90 ± 1	0.82 ± 0.01	7.1 ± .1
18	66 ± 1	0.69 ± 0.01	7.1 ± .1
32	66 ± 1	0.68 ± 0.01	10 ± 1
56	66 ± 1	0.59 ± 0.03	15 ± 2
68	66 ± 1	0.74 ± 0.01	17 ± 1
Average	70 ± 20	0.71 ± 0.08	-

Section 3.3: Summary

The monomer density of P3MT brush films was probed with a variety of techniques. The volume density of the monomer at the surface of the substrate during initial growth is determined from the initiated monolayer areal density. The monomer volume density of obtained from RBS measurements agrees with the density at the substrate surface obtained from cyclic voltammetry measurements, indicating that the density of the film does remains constant as the film gets thicker. The crystalline monomer density of P3MT brushes was found to be three times higher than that of the bulk brush, indicating a very low degree of crystallinity within the film, though some crystalline regions are observed by GIWAXS. The monomer densities determined from the experiments are compared in Table 3.2.

Table 3.2: Monomer volume density extracted from various measurements.

Measurement	Monomer Volume Density (monomers nm^{-3})
CV (volume density near substrate)	3.3 ± 0.5
RBS (bulk volume density)	2.8 ± 0.4
GIWAXS (crystalline volume density)	9.3

The polymer chains within the brush have a slight vertical orientation on average as indicated by the polarized UV-vis. This average orientation is observed in brushes of all thicknesses. The surface of the brush films follows a log-normal height distribution due to the presence of tall columns. Columns appear nearly instantaneously during brush growth, and rise many times higher than the average brush thickness. The columns exhibit a characteristic cross-sectional area and areal density that is independent of film thickness.

The presence of a characteristic density and cross-sectional area of the columns in the films is likely the result of the specific set of synthetic conditions used. The characteristic P3MT brush structures may be tunable by varying synthetic parameters, such as temperature, stirring rate, catalyst, monomer regioregularity and substitution, solvent and/or thermal annealing, and monolayer structure/density. The findings presented here therefore provide the means and impetus for future explorations into the interplay between the synthetic

conditions and controlled structure and morphology in brush films.

CHAPTER 4: ELECTRONIC PROPERTIES OF P3MT BRUSHES

Due to the morphology of polymer brushes, electronic devices utilizing conjugate polymer brushes are expected to exhibit enhanced intramolecular transport. Here, P3MT brush devices are fabricated, and their electronic properties are studied primarily using conducting AFM. However, the top electrode of P3MT brush devices contacts the top of the columns of the brush film, and thus does not contact the majority of the columns in the film. Therefore, the interface between the columns and the electrode must be examined in order to interpret the observed I-V behavior.

Section 4.1: Characterization of Charge Transport through CPB Devices.

To effectively study the charge transport through the P3MT CPB (conjugated polymer brush) films, the KTP process is used to print noncovalently attached Au electrodes onto the CPB films, producing arrays of ITO-CPB-Au trilayer devices (called CPB devices below) for I-V measurements using conductive AFM (Figure 4.1).[84] Hundreds of KTP devices can be simultaneously printed on a single CPB sample. The resulting electrodes are not conformal with the brush surface (Figure 4.2).

For cAFM I-V measurements, a conducting tip is brought into contact with the printed electrode, allowing a bias to be applied between the printed electrode and the ITO substrate, and the current response to be measured. A schematic of the device measurement setup is shown in Figure 4.2. The conducting tip is grounded, and the bottom substrate is biased. When a positive bias is applied to the device it is referred to as forward bias, and when a negative bias is applied it is referred as reverse bias. A more detailed circuit diagram is shown in the experimental methods section (Figure 2.9 in Chapter 2).

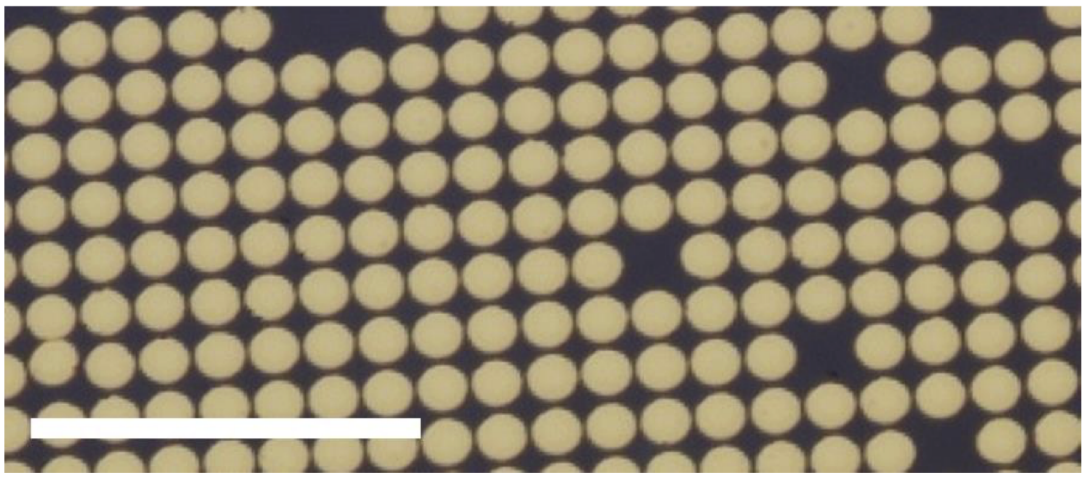

Figure 4.1: Microscope image of gold electrodes printed on a 15 nm thick P3MT CPB film. electrodes have a 12 μm radius. The white scale bar is 100 μm. Figure S12 in Ref [54], reproduced with permission.

The device thickness d is generally greater than the nominal CPB thickness L_0, which is determined through the scratch profilomtery as described in Chapter 3. Therefore, the device thickness d is greater than the film thickness L_0 (Figure 4.2). Electrodes are sometimes deformed vertically during the printing process, resulting in multiple regions with different device thicknesses. This deformation is indicated by Δd in Figure 4.2. Electrodes contact a small percentage of the CPB film, only touching the tall columns (see discussion below).

Two types of I-V curves are observed in CPB devices (Figure 4.3). The "s-shaped" I-V curves show the characteristic nonlinear behavior typical of narrow gap semiconductors (Figure 4.3a). The "duck curves," or ducks for short, have eponymous hysteresis reminiscent of a duck's head (Figure 4.3b). The hysteresis in ducks is caused by contaminants within the brush which act as long lifetime charge traps, creating a coulomb blockade effect that limits current. CPB synthesis produces Cl, Mg and I byproducts, and requires Pd catalyst, and failure to clean the CBP properly after synthesis leaves residual metal contaminants in the film. These containments act as charge trapping sites that cause the coulomb blockade effect. The duck I-V behavior is not intrinsic to CPBs, and so the ducks are ignored for this

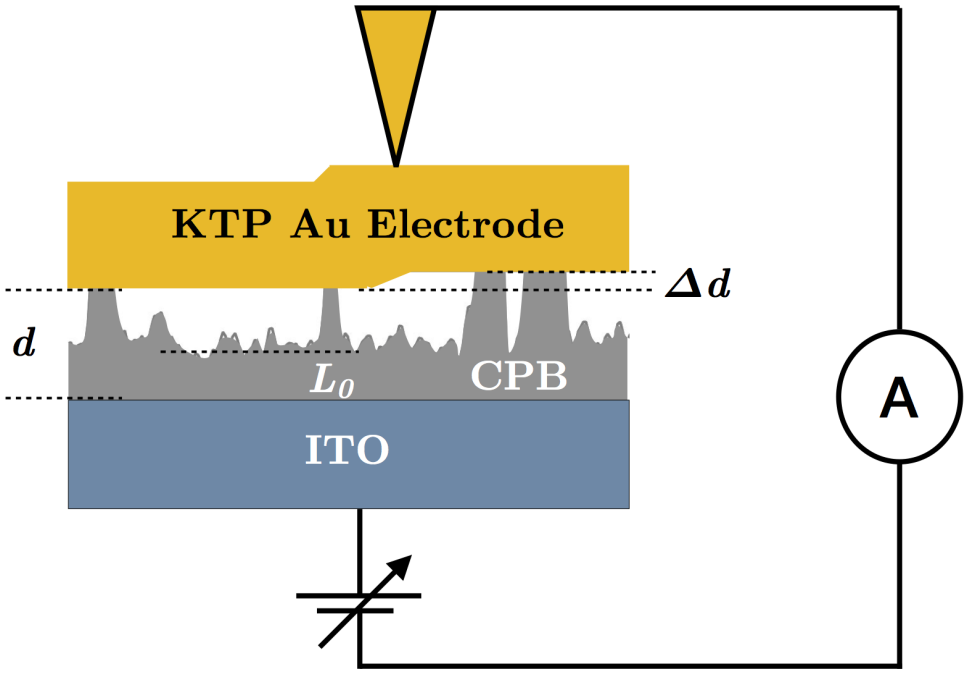

Figure 4.2: The schematic for cAFM measurements of CPB devices with KTP electrodes. The conducting tip contacts the printed electrode, allowing the device to be biased and a current response to be measured. The brush thickness L_0, device thicknesses d, and electrode deformation Δd are indicated.

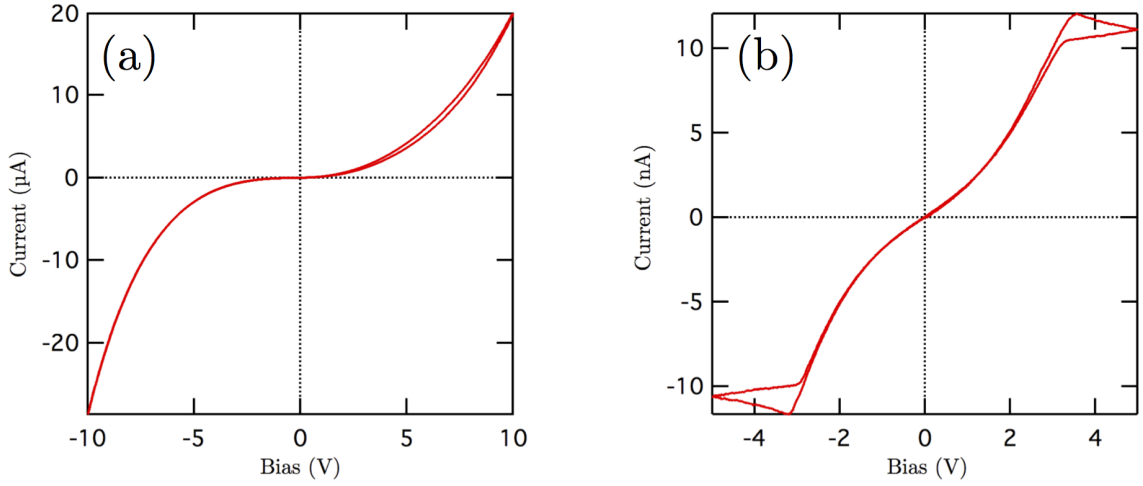

Figure 4.3: Two types of I-V curves are observed. (a) An "s-shaped" I-V curve obtained from cAFM on KTP devices. (b) A "duck" I-V curve. The characteristic duck shape is due to the presence of contaminants within the brush.

work. If ducks are observed, subsequently washing the CPB and printing new electrodes can result in "clean" s-shaped I-V behavior.

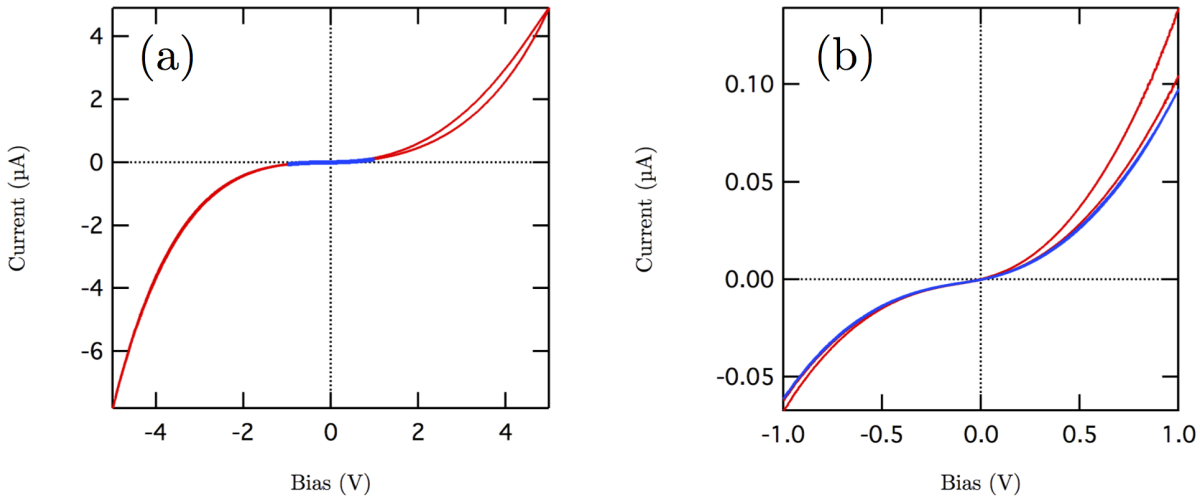

Figure 4.4: Repeated I-V measurements on a single device at different biases. (a) The blue curve is the initial measurement to ±1 V, and the red curve is a subsequent measurement up to ±5 V. (b) The behavior of the two curves between -1 V and 1V. The two measurements overlap, with the ±5 V curve exhibited some hysteresis at forward bias.

For each CPB sample, I-V curves were acquired for 10 to 20 devices. The I-V characteristics of each device were measured up to ±1 V, and on some device additional measurements to ±5 V and ±10 V were performed. The curves exhibit little to no hysteresis when biased to ±1 V, but can exhibit significant hysteresis for higher bias measurements (Figure 4.4). The size of the hysteresis depends on the magnitude of the maximum bias applied and the bias direction, with the forward bias exhibiting larger hysteresis than the reverse bias (Figure 4.3a). The hysteresis is most likely due to charging effects (discussed below) are likely due to various extrinsic effects, and so this work focuses on analyzing the low bias ±1 V measurements.

Typical I-V curves for CPB samples with brush thickness L_0 ranging from 5 to 91 nm are shown on the linear, log, and semi-log scales. For some samples the I-V behavior of devices falls into two distinct shapes or magnitudes, and a typical curve is chosen from each group. This grouping is likely due to deformation on some electrodes which can cause a change

in effective contact area and device thickness (discussed below). The typical curves in the linear and log-log plots correspond to the blue and green curves in the semi-log plot.

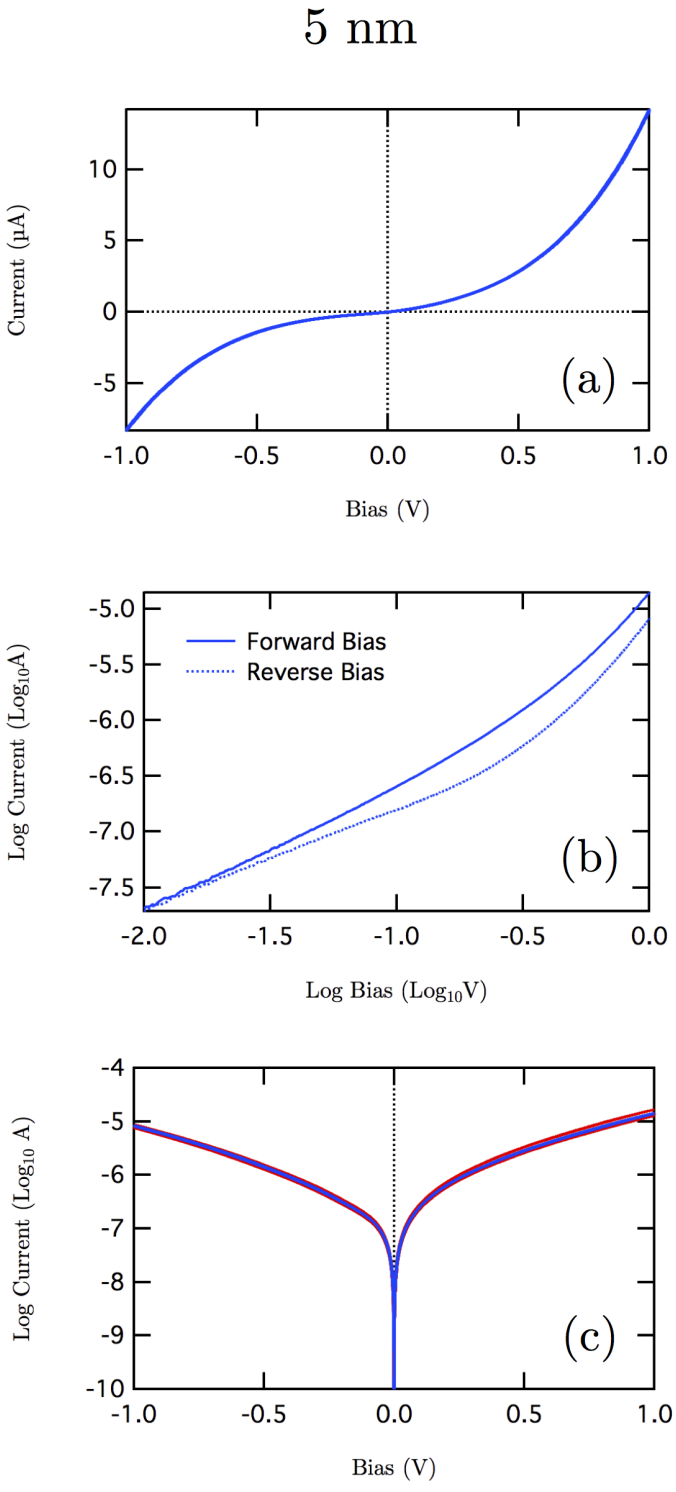

Figure 4.5: I-V curves of CPB devices with L_0 of 5 nm. A typical I-V curve in (a) linear and (b) log-log scale. (c) I-V curves for 10 devices on semi-log scale.

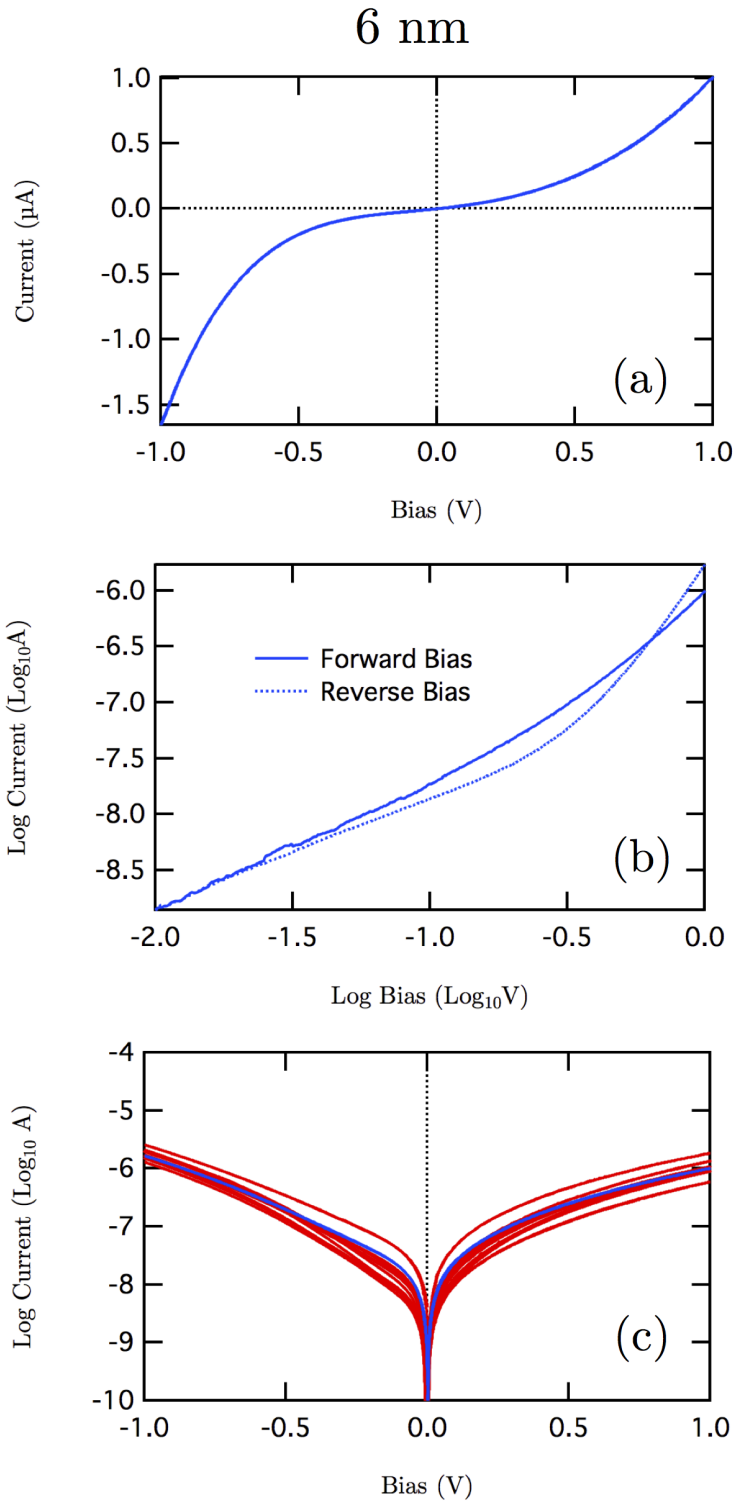

Figure 4.6: I-V curves of CPB devices with L_0 of 6 nm. A typical I-V curve in (a) linear and (b) log-log scale. (c) I-V curves for 11 devices on semi-log scale.

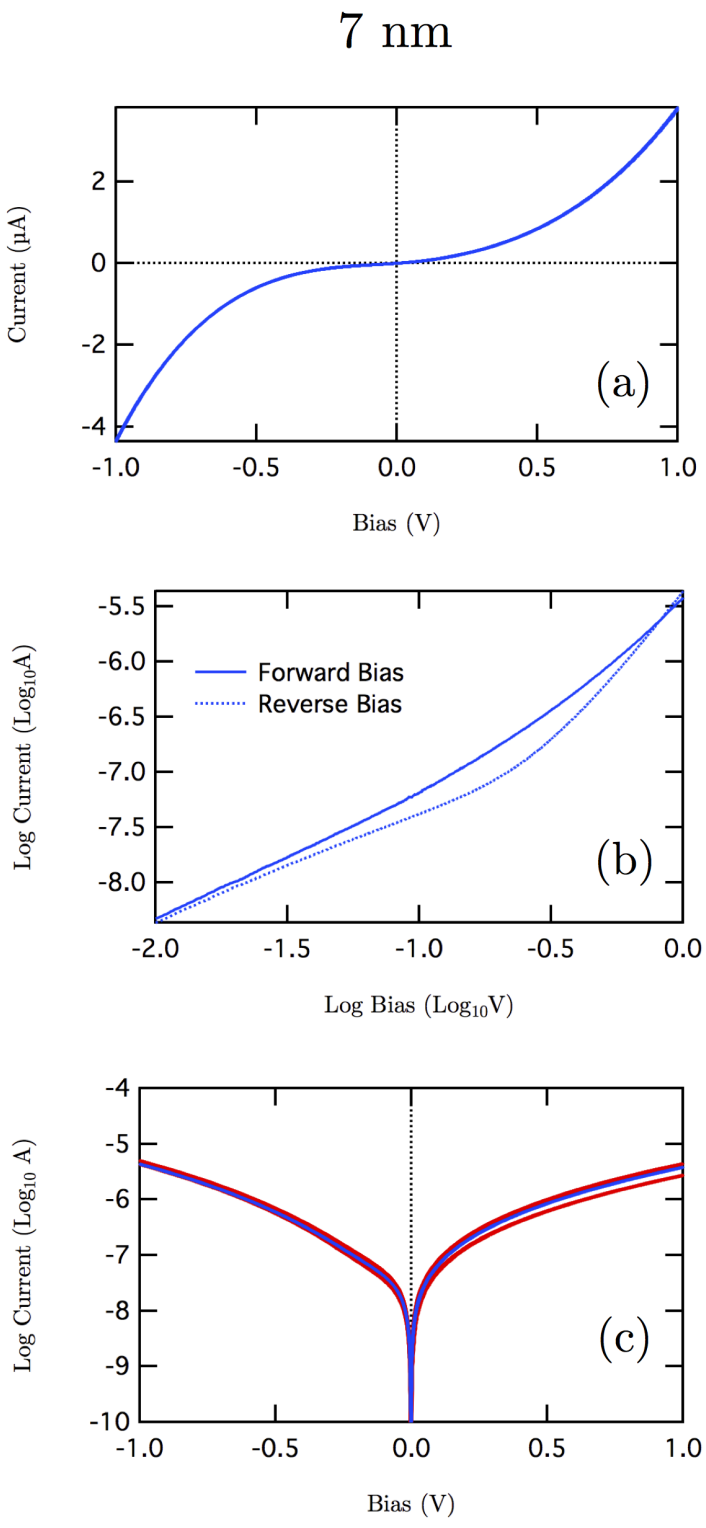

Figure 4.7: I-V curves of CPB devices with L_0 of 7 nm. A typical I-V curve in (a) linear and (b) log-log scale. (c) I-V curves for 8 devices on semi-log scale.

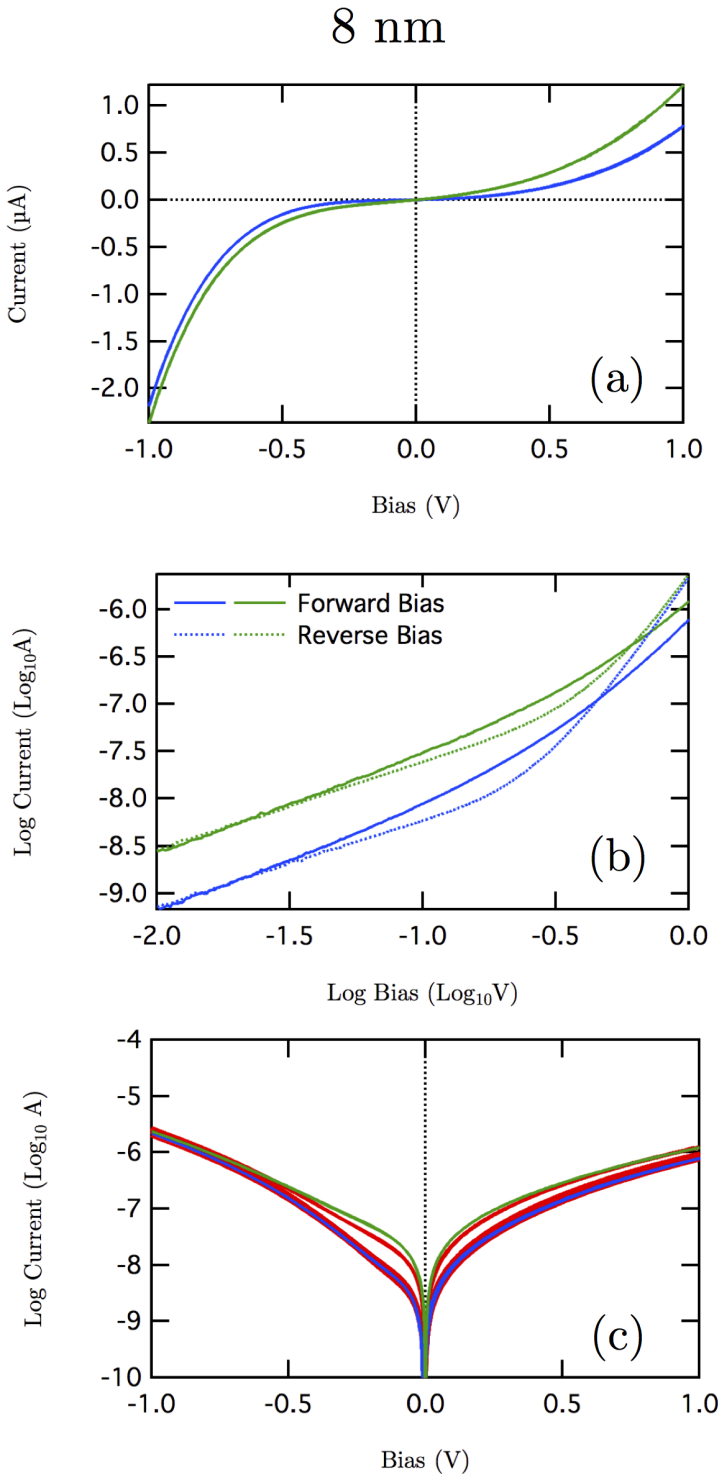

Figure 4.8: I-V curves of CPB devices with L_0 of 8 nm. A typical I-V curve in (a) linear and (b) log-log scale. (c) I-V curves for 16 devices on semi-log scale.

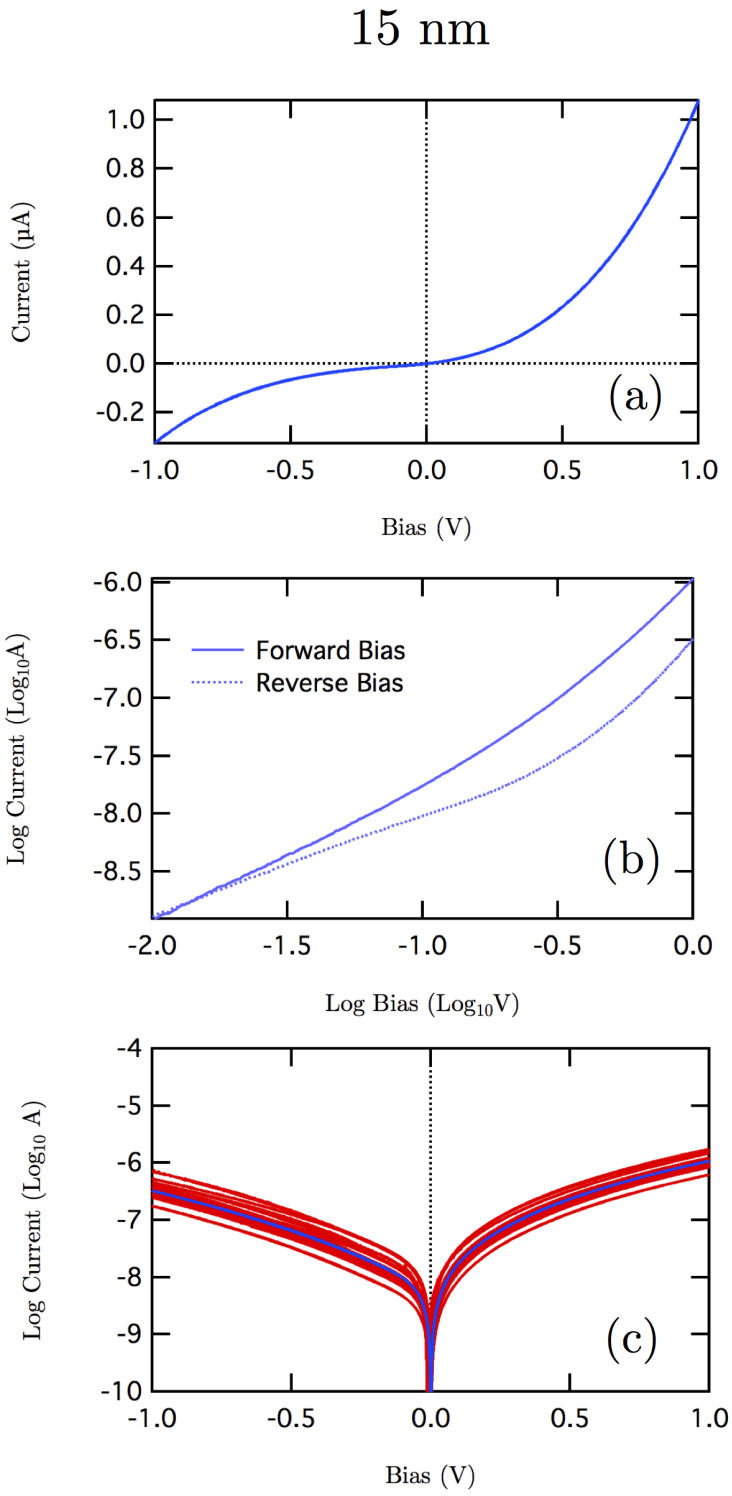

Figure 4.9: I-V curves of CPB devices with L_0 of 15 nm. A typical I-V curve in (a) linear and (b) log-log scale. (c) I-V curves for 19 devices on semi-log scale.

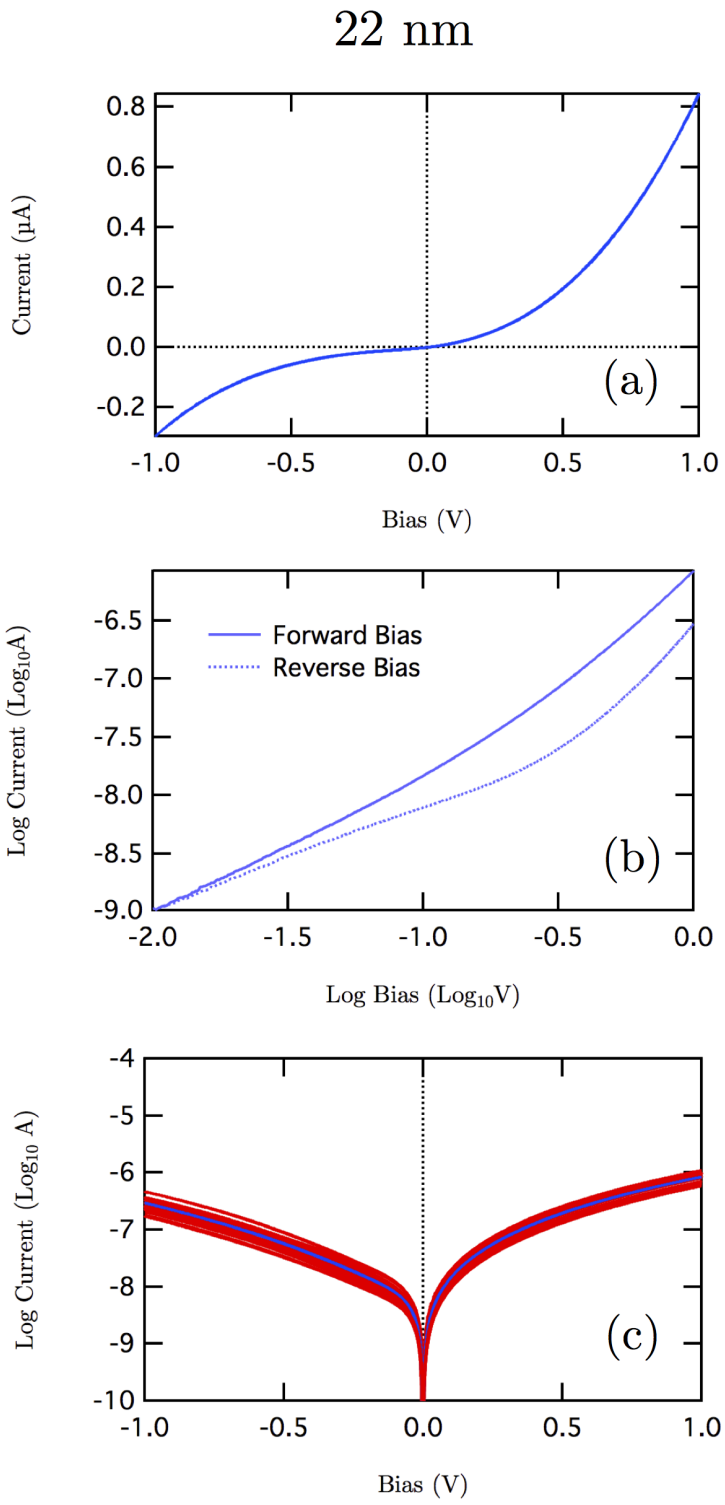

Figure 4.10: I-V curves of CPB devices with L_0 of 22 nm. A typical I-V curve in (a) linear and (b) log-log scale. (c) I-V curves for 22 devices on semi-log scale.

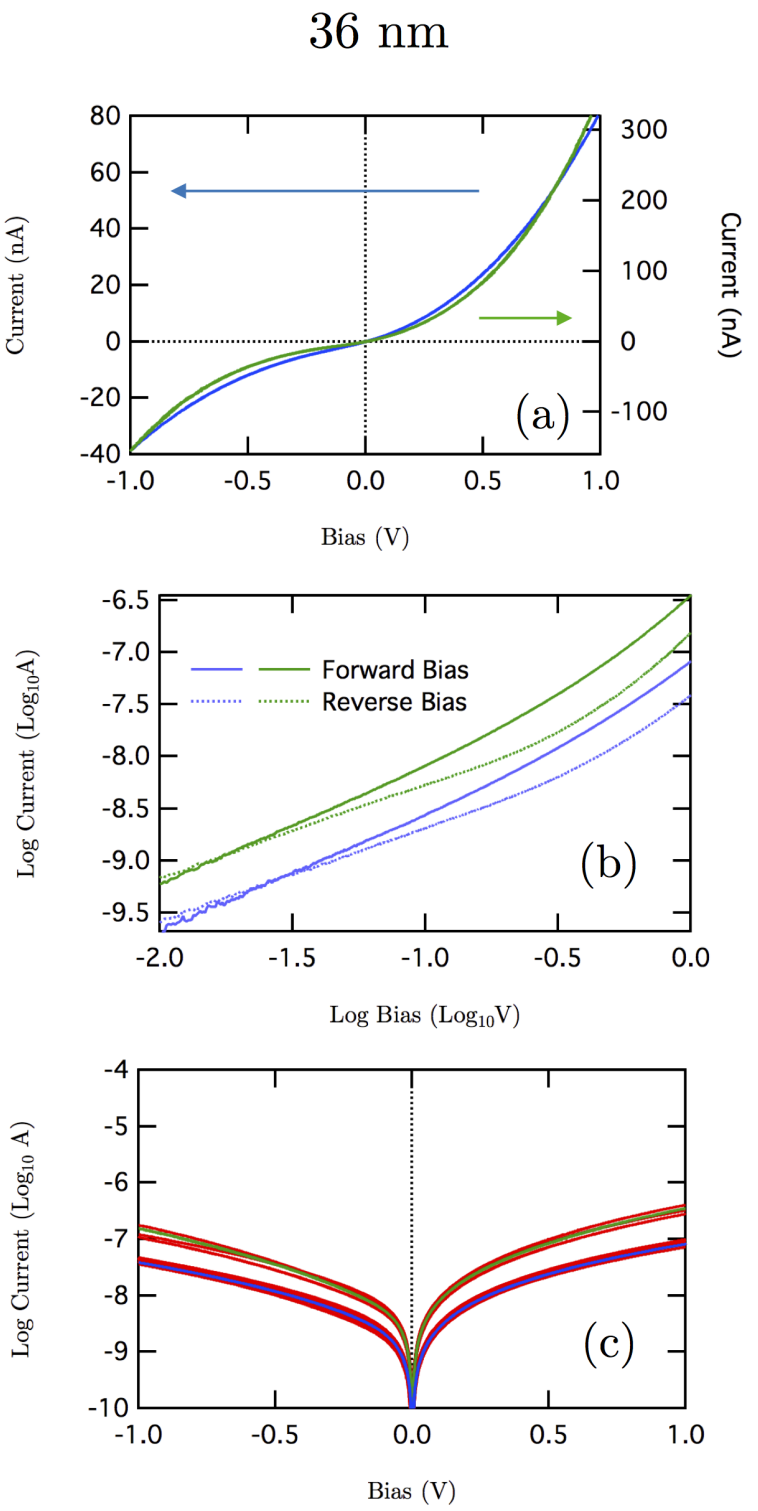

Figure 4.11: I-V curves of CPB devices with L_0 of 36 nm. A typical I-V curve in (a) linear and (b) log-log scale. (c) I-V curves for 16 devices on semi-log scale.

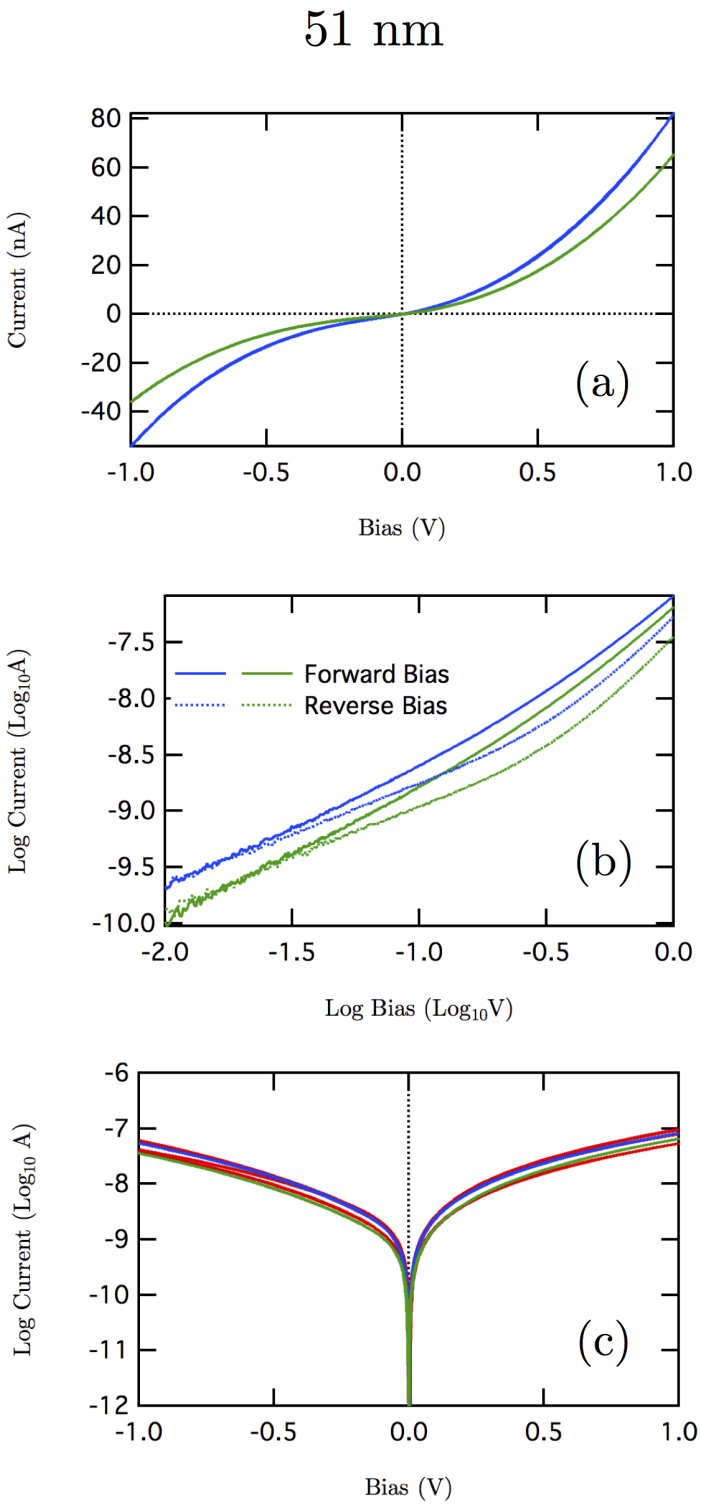

Figure 4.12: I-V curves of CPB devices with L_0 of 51 nm. A typical I-V curve in (a) linear and (b) log-log scale. (c) I-V curves for 8 devices on semi-log scale.

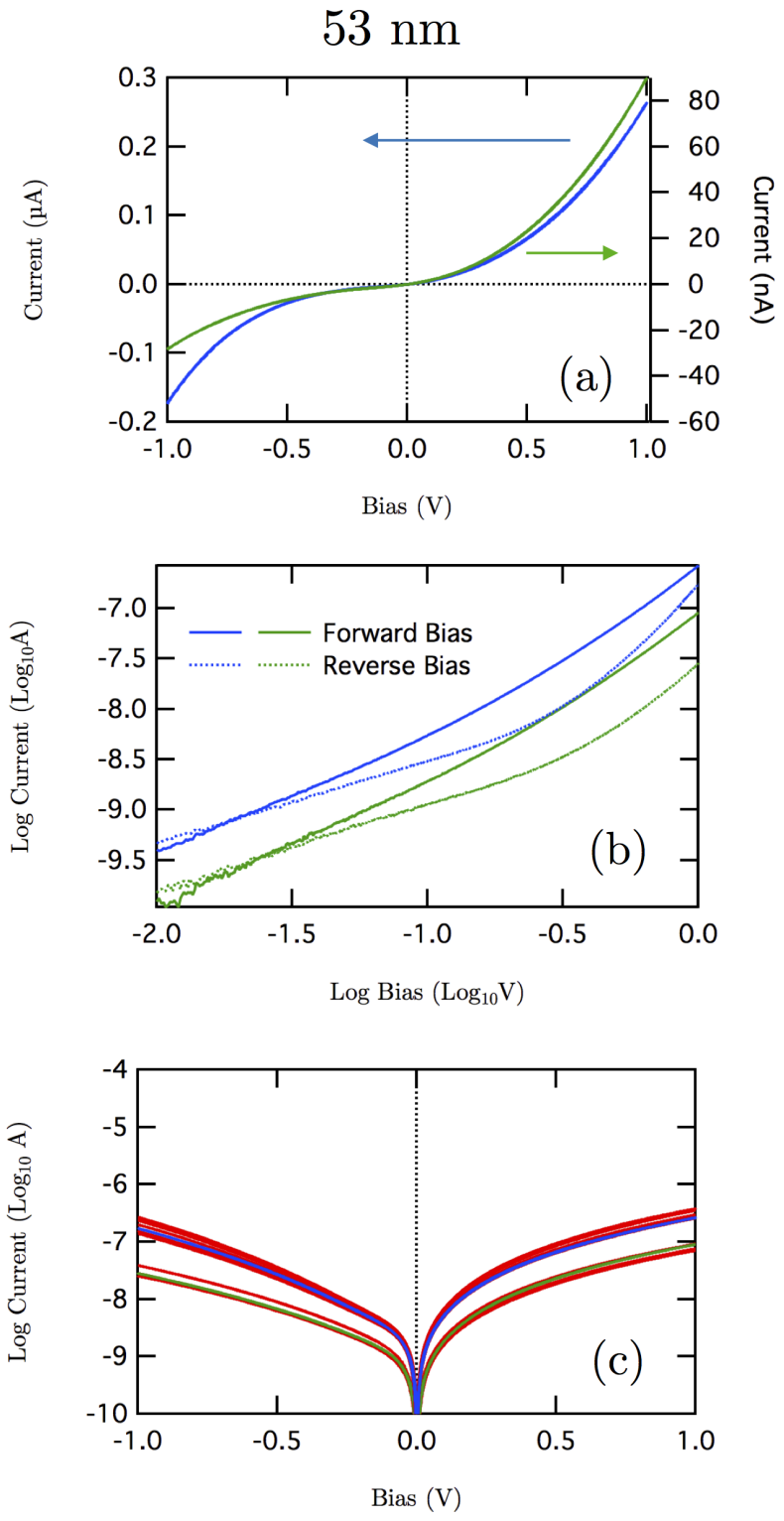

Figure 4.13: I-V curves of CPB devices with L_0 of 53 nm. A typical I-V curve in (a) linear and (b) log-log scale. (c) I-V curves for 12 devices on semi-log scale.

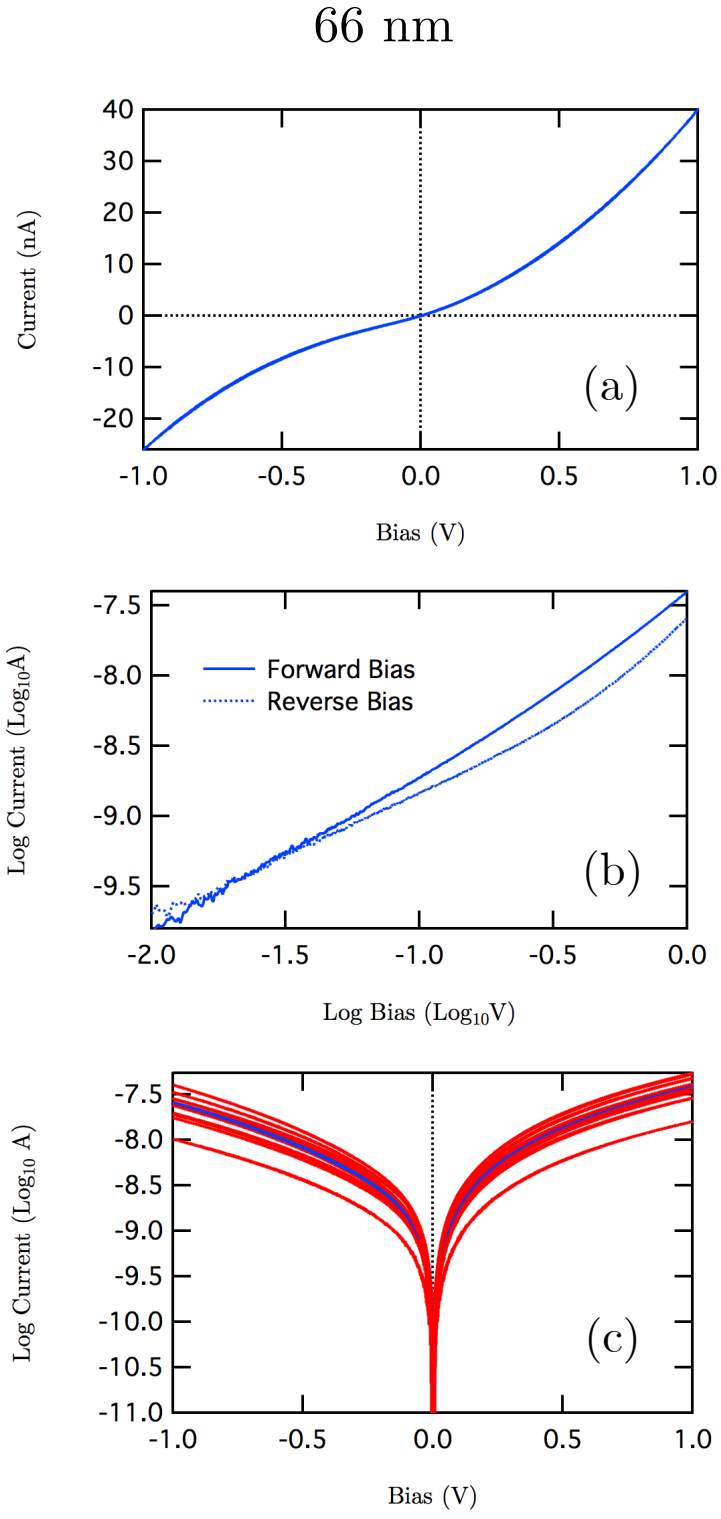

Figure 4.14: I-V curves of CPB devices with L_0 of 66 nm. A typical I-V curve in (a) linear and (b) log-log scale. (c) I-V curves for 15 devices on semi-log scale.

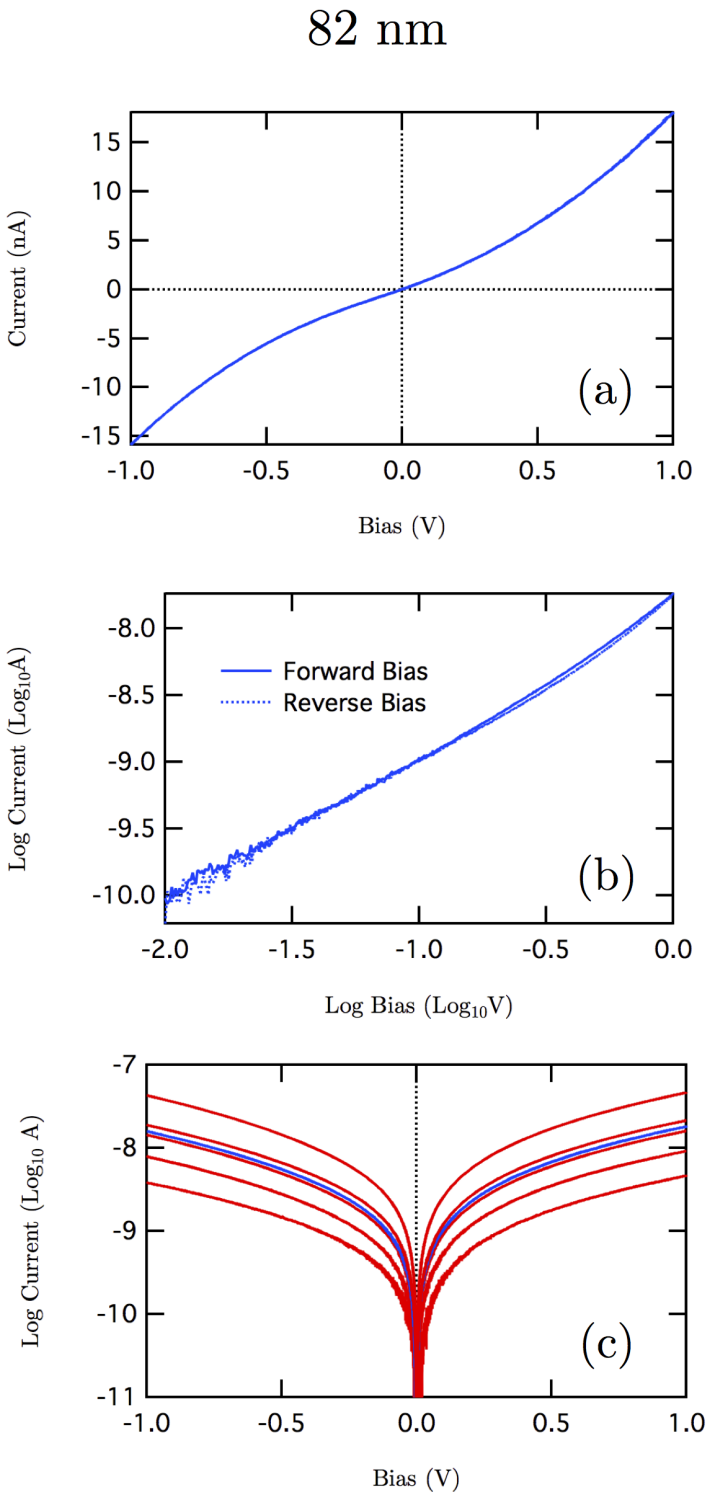

Figure 4.15: I-V curves of CPB devices with L_0 of 82 nm. A typical I-V curve in (a) linear and (b) log-log scale. (c) I-V curves for 14 devices on semi-log scale.

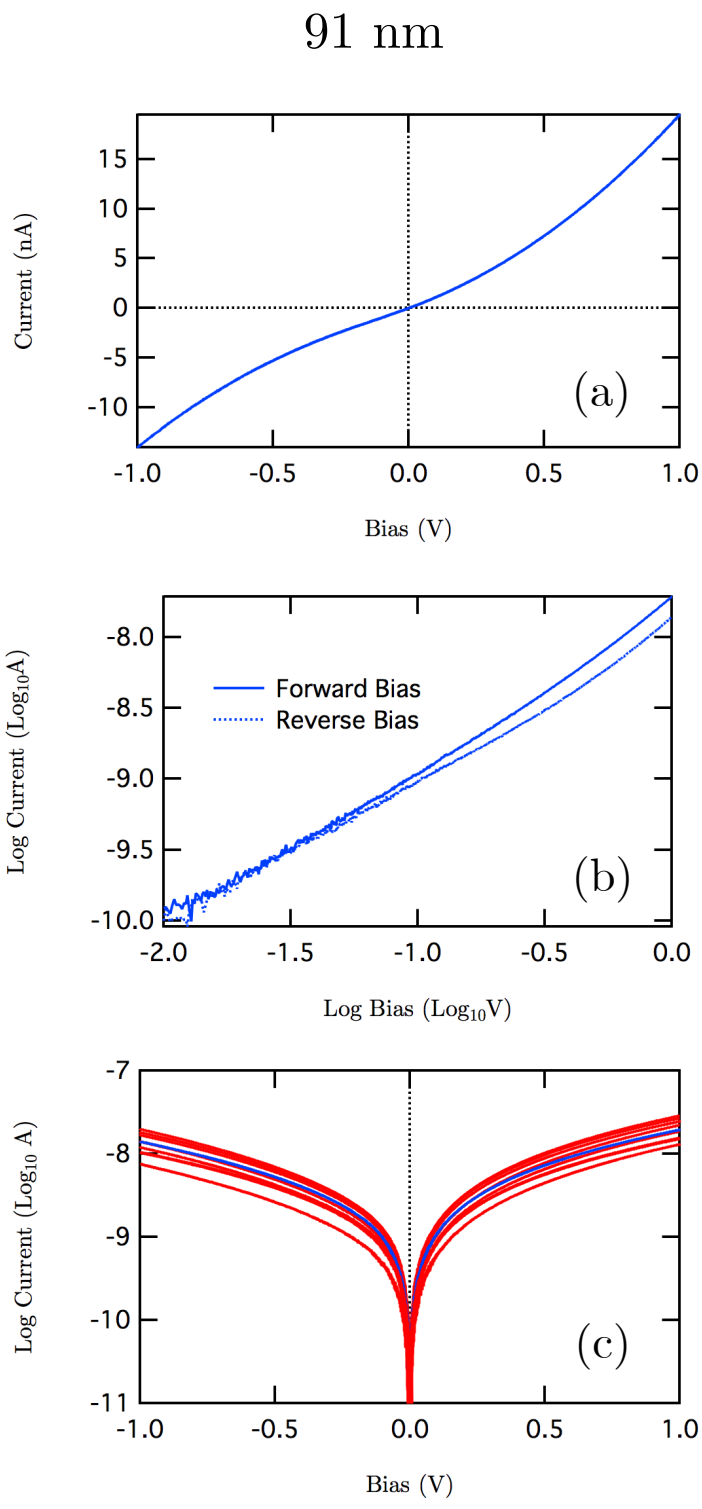

Figure 4.16: I-V curves of CPB devices with L_0 of 91 nm. A typical I-V curve in (a) linear and (b) log-log scale. (c) I-V curves for 9 devices on semi-log scale.

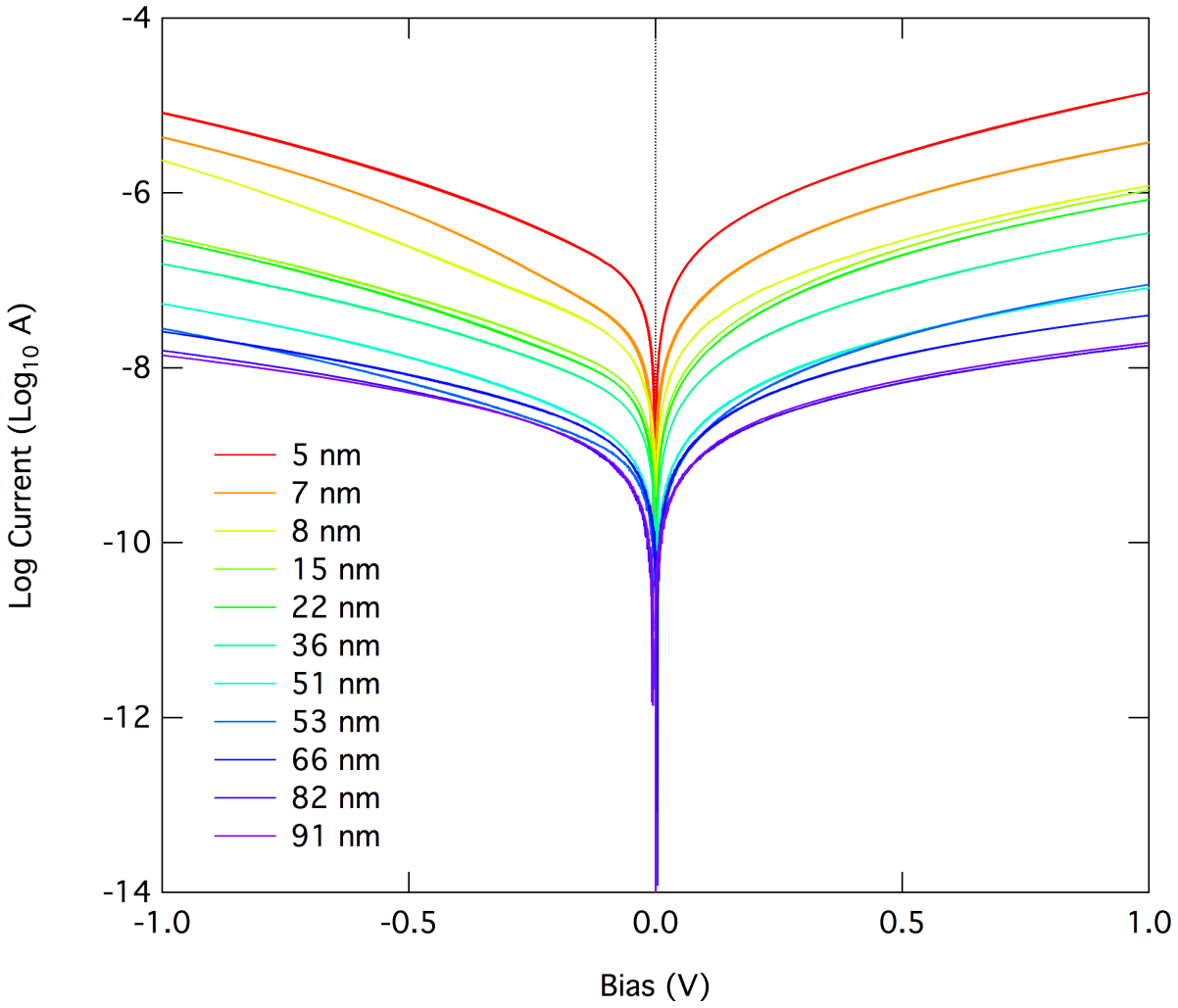

Figure 4.17: Comparison of I-V curves with L_0 from 5 to 91 nm.

The conductance, i.e. the magnitude of the current for a given voltage, decreases with increasing brush thickness (Figure 4.17). The differential conductance curves ($\Delta I/\Delta V$ vs. V) were calculated by linear fitting around every point in the I-V curve at a bias interval of ± 40 mV. Typical differential conductance curves from CPB devices of various thicknesses are shown in Figure 4.18a. The minimum of the differential conductance for all devices occurs at an offset from 0 V. This offset appears to show a slight dependence on brush thickness, which resembles the characteristic behavior of an interfacial dipole (Figure 4.18b).

A maximum resistance R_0 is determined for each device, i.e. the inverse of the minimum differential conductance. For CPB films with $L_0 > 8$ nm (Figure 4.2), R_0 exhibits linear

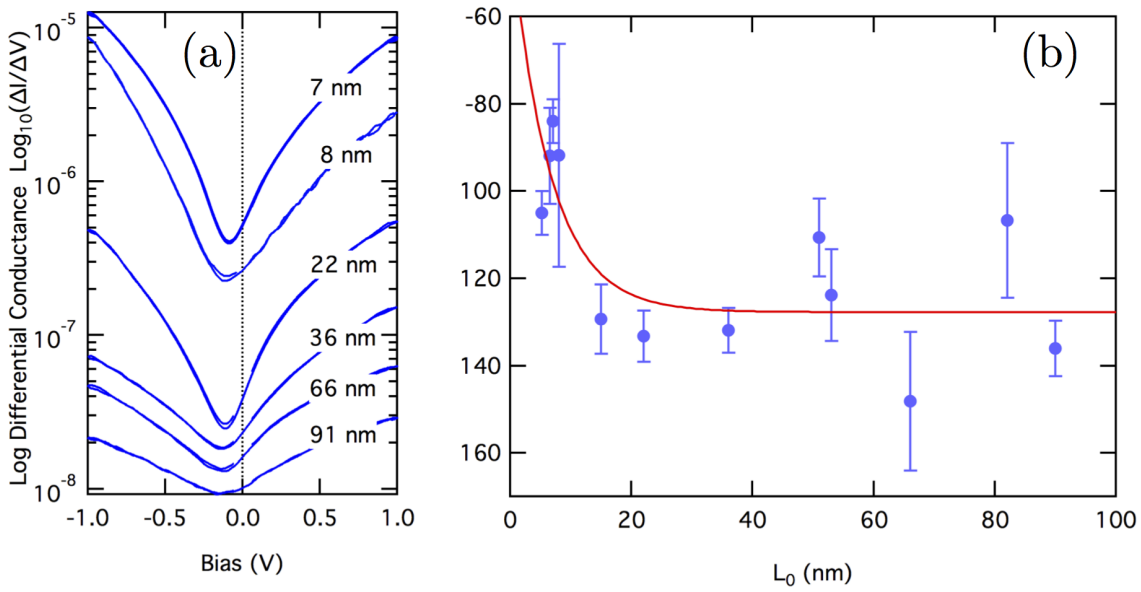

Figure 4.18: (a) Typical differential conductance curves with L_0 from 7 to 91 nm thick. (b) Average minimum conductance offset as a function of film thickness. The red line represents behavior characteristic of interfacial dipoles.

behavior with respect to L_0, consistent with diffusive transport processes outside of the tunneling regime (Figure 4.19a).[85] Below 8 nm a transition occurs, and R_0 no longer depends linearly on L_0 (Figure 4.19b). This transition is often observed in molecular wires, and indicates a transition from tunneling processes between electrodes to hopping transport through the film.[85] The behavior at low L_0 is exponential, as indicated by the line in Figure 4.19c, with a slope $\beta = 0.5$ nm^{-1}. Tunneling transport results in resistance with exponential length dependence, however the β values for tunneling through organic molecules are usually over 1 nm^{-1}. Figure 4.19c demonstrates again a clear transition between transport regimes occurring around 8 nm, with the line indicating linear behavior.

The offset of the conductance minimum observed in Figure 4.18, as well as UPS measurements, indicate the presence of a built in potential due to dipoles at the electrode-CPB interfaces. This potential must be accounted for when determining the bias (and therefore the electric field) across the sample. The forward and reverse bias of typical I-V curves are compared on log scale using an adjusted bias, $V_{adj} = V - V_d$, where V_d is the built in

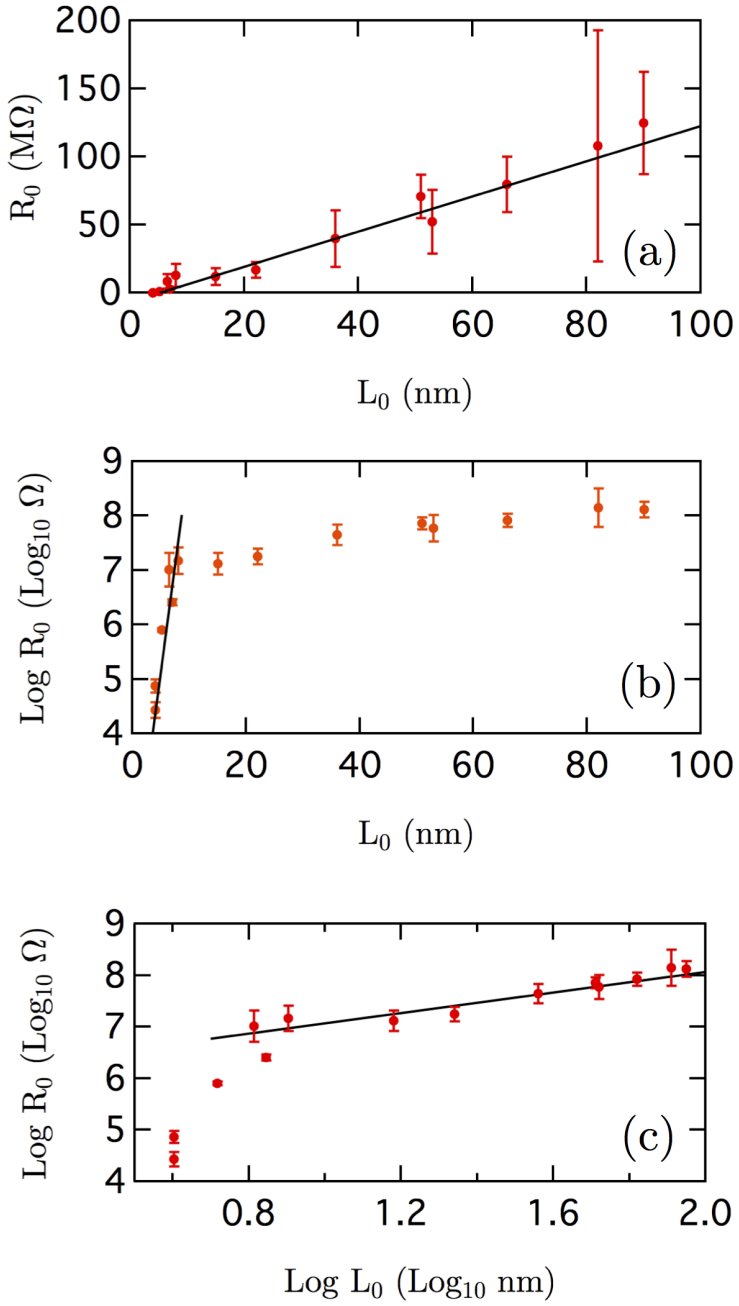

Figure 4.19: R_0 vs. L_0 for all CPB Devices. (a) Linear plot. The slope corresponds to 1 MΩ/nm. This resistance is adjusted by ta contact factor to yield a resistivity of 1.4 x 10^5 Ω-cm (discussed below). (b) Semi-log plot. The black line indicates exponential behavior with $\beta = 0.5$ nm^{-1} (based on device thickness d, not CPB thickness L_0). Expected β values for tunneling are > 1 nm^{-1}.[85] (c) Log-log plot. There is a clear departure from the linear dependence (line) at low thicknesses, indicating a transition in transport mechanism.

potential due to the presence of interfacial dipoles. Near zero bias, both the forward and reverse directions behave linearly (i.e. they have a slope of 1 on the log scale corresponding to the black lines in figures below), but as bias increases they become non-linear. The same asymmetry that appeared in the unadjusted I-V curves is still present. In thicker devices the forward bias "takes off" before the reverse bias, and the asymmetry favors the forward bias at $\sim$1 V. This asymmetry decrease as L_0 increases.

The I-V curves show asymmetric current response between the forward and reverse bias directions. By defining a current asymmetry as the ratio between the magnitudes of the forward and reverse current at the same magnitude of bias, the asymmetry of the I-V curves vs. the CPB thickness is shown in Figure 4.20. For L_0 <8 nm, the I-V curves exhibit large current in the reverse bias at 1 V. For L_0 >8 nm the larger current tends to be in the forward bias at 1 V, and the asymmetry asymptotically approaches 1 as L_0 increases. The current response in devices intrinsically depends on the electric field E across the device, and at a given bias V thicker devices will have lower current ($E \sim V/d$). As the field across a device approaches 0, the I-V behavior becomes linear, and therefore, as L_0 increases the asymmetry at 1V approaches 1.

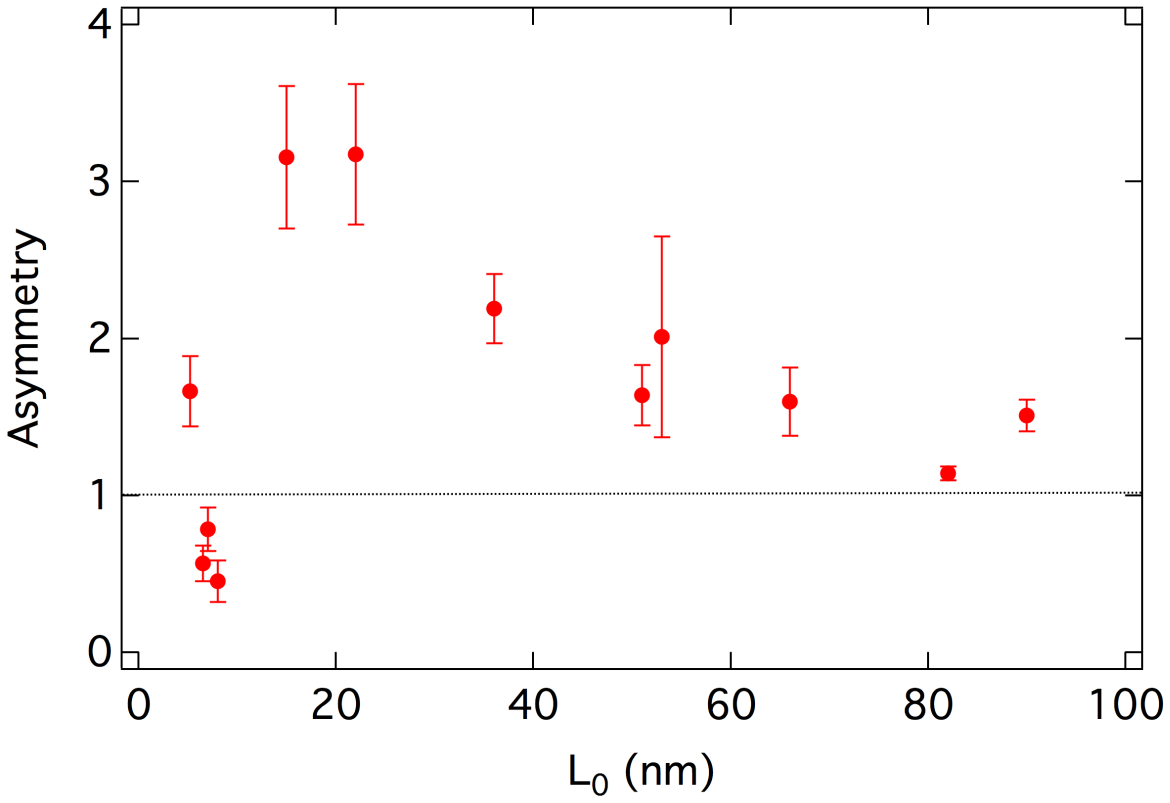

Figure 4.20: Asymmetry in I-V curves for CPB devices.

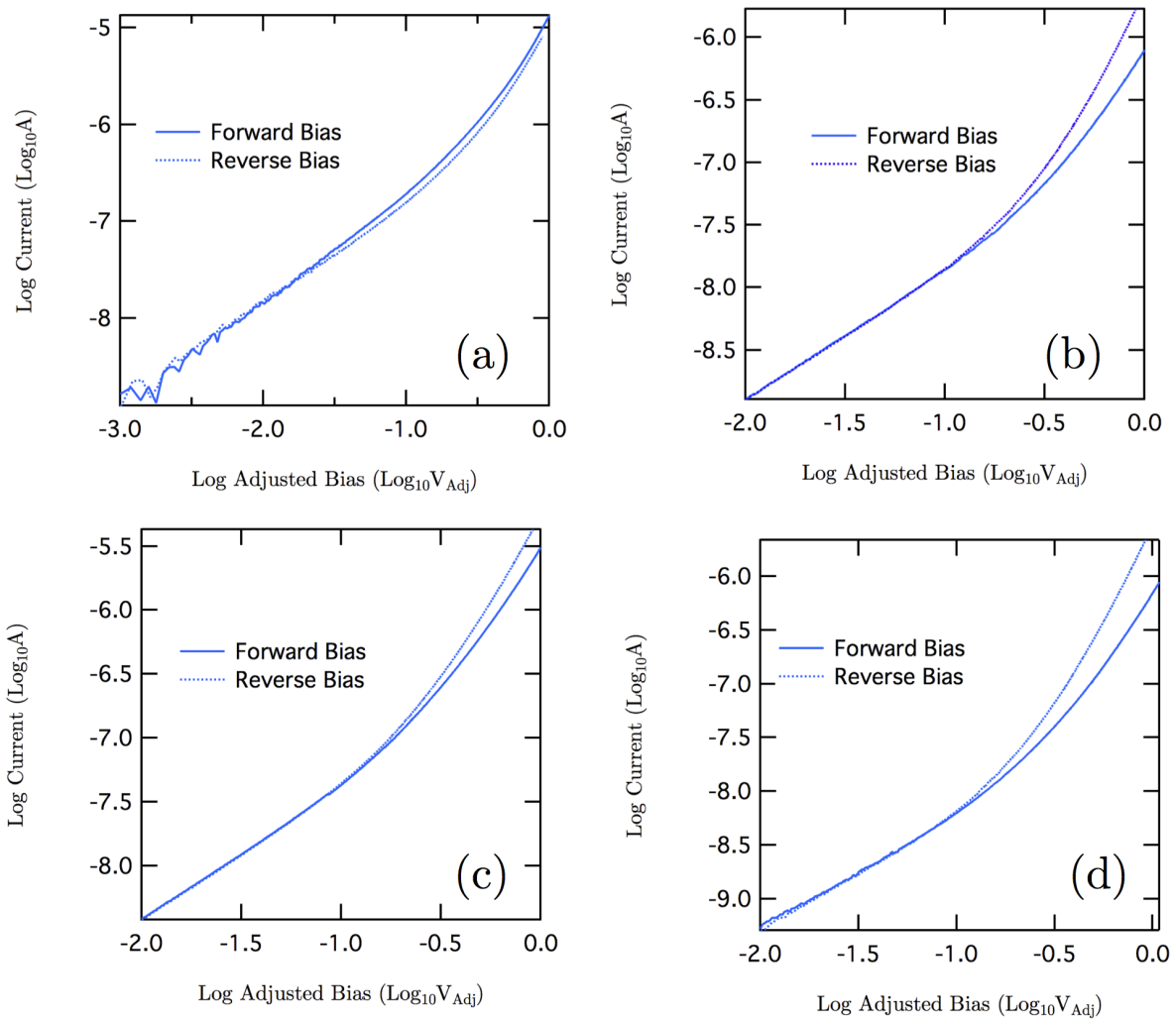

Figure 4.21: Low thickness I-V behavior for CPB devices ($I_{forward} < I_{reverse}$ at 1V). Log-log plots of current vs. bias for samples with L_0 of (a) 5 nm, (b) 6 nm, (c) 7 nm, and (d) 8 nm.

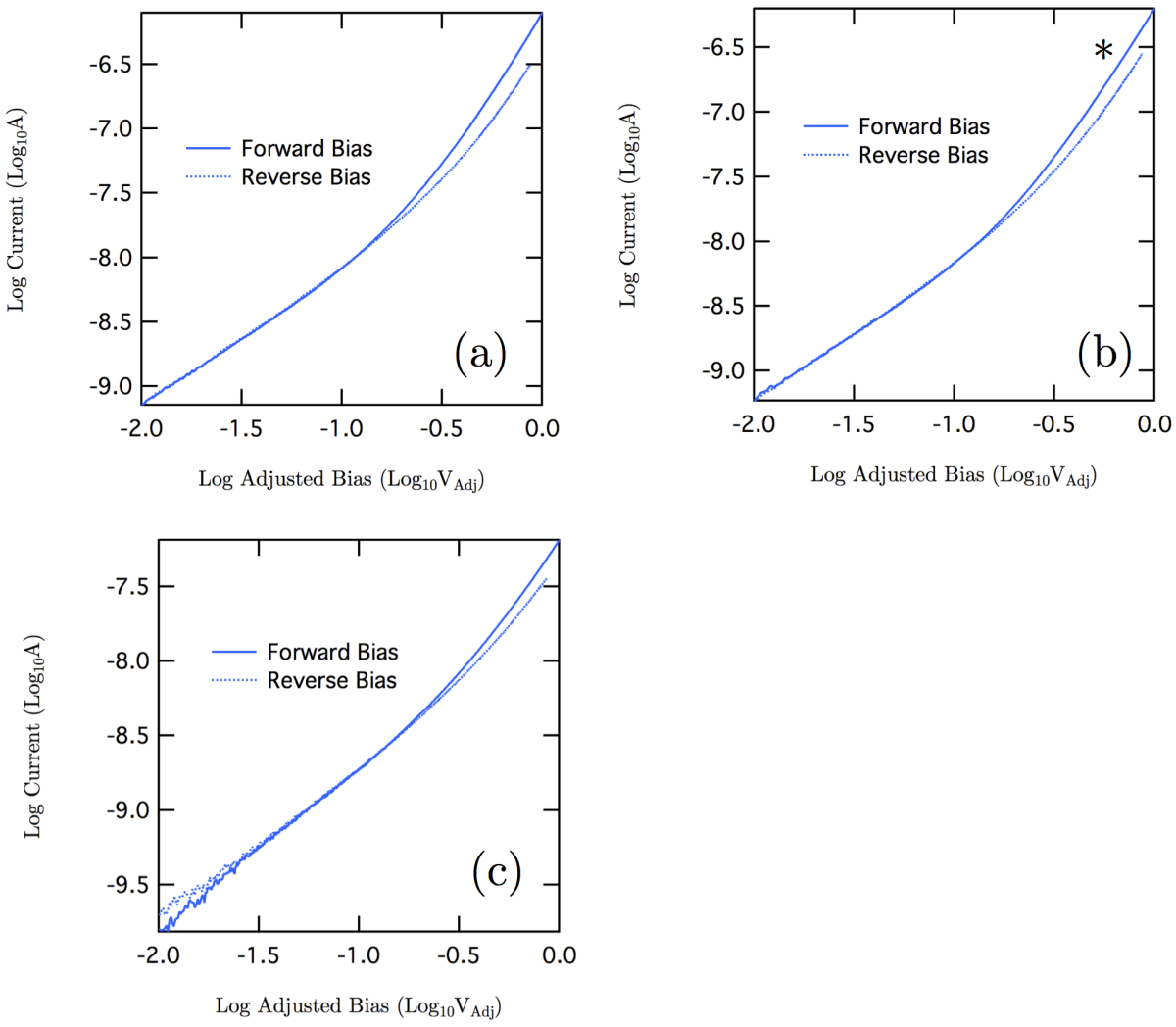

Figure 4.22: Intermediate thickness I-V behavior for CPB devices ($I_{forward} > I_{reverse}$ at 1V). Log-log plots of current vs. bias for samples with L_0 of (a) 15 nm, (b) 22 nm, and (d) 36 nm.

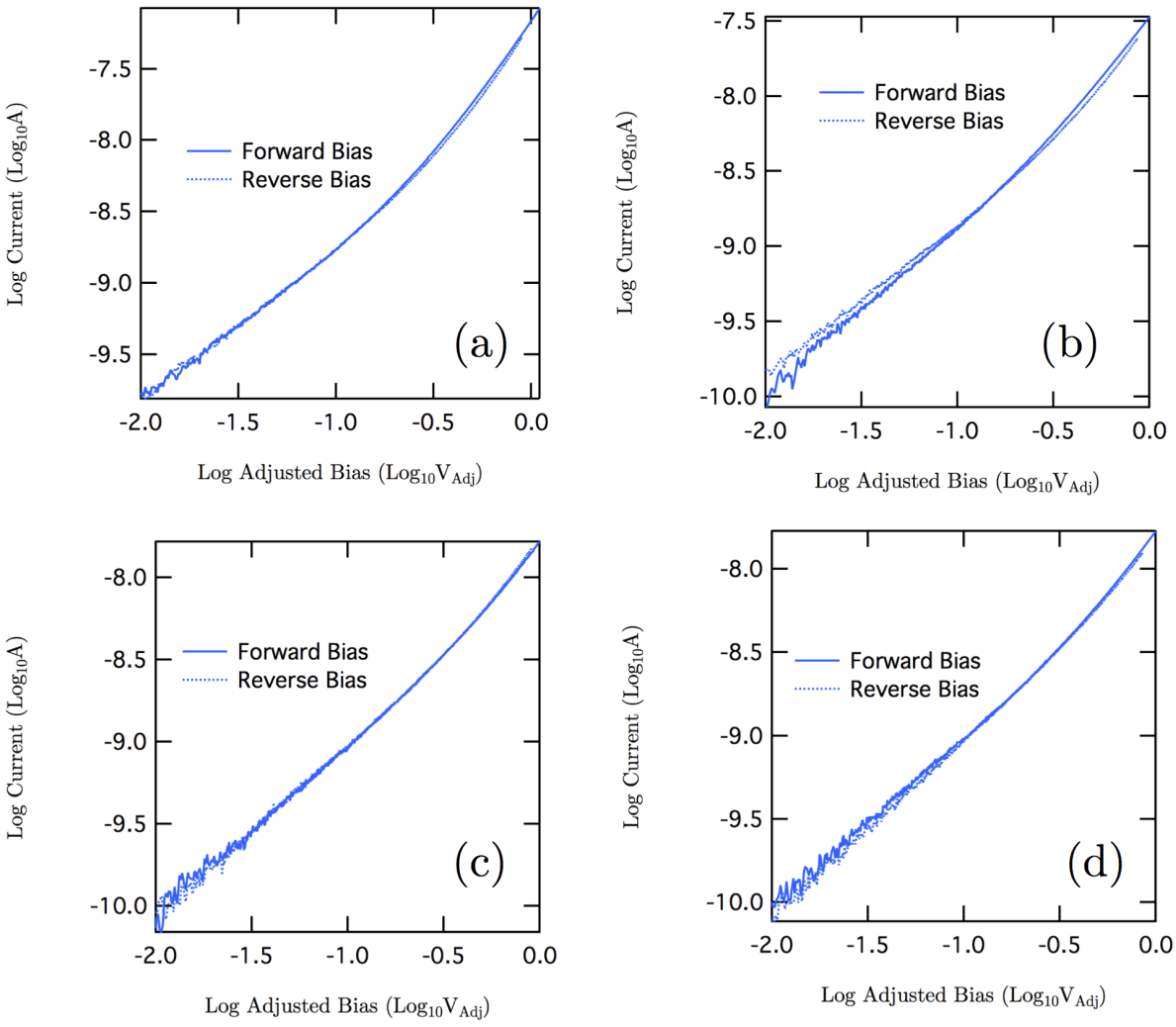

Figure 4.23: High thickness I-V behavior for CPB devices ($I_{forward} \sim I_{reverse}$ at 1V). Log-log plots of current vs. bias for samples with L_0 of (a) 51 nm, (b) 66 nm, (c) 82 nm, (d) 91 nm.

Section 4.2: I-V Behaviors

Near zero bias the CPB devices exhibit linear I-V behavior, and can be modeled using Ohm's law (i.e. $J = \sigma E$). Of interest is the resistivity, $\rho = 1/\sigma$, of CPBs at zero field, which can be compared to resistivities of similar materials. Resistivity can be obtained from the slope of a resistance vs. device thickness plot multiplied by the device contact area. For the CPB devices, the top electrode is not conformal with the brush surface, contacting only the tallest columns. The device thickness is therefore larger than the nominal brush thickness,

and the device contact area is less than the total electrode area. These factors must be considered and analyzed for resistivity to be calculated.

4.2.1: Polymer-Electrode Contact Analysis for CPB Devices

In most electrode-molecule-electrode devices, the contact between the electrodes and the active molecular layer is assumed to be conformal, and the distance between the top and bottom electrodes is assumed to be uniform, so electronic properties are determined under the assumption of an effective electrode area and a molecular layer thickness.[36,86,87] However, given the roughness of the P3MT brush film surface, conformal contact between the film and top electrode is undesirable, as charge transport would be shorted through the thinnest parts of the device instead of the tall columns on the surface of the films.

In order to understand electronic measurements on the KTP fabricated devices, the contact between the CPBs and the fabricated top Au electrodes and the CPB thickness within each devices must be examined. Because of the mechanical deformation of the Au electrode during the KTP process and the large widths present in the surface height distributions of the P3MT CPB films (Figures 3.10 and 3.11), the top Au electrode in the CPB devices is neither conformal with the CPB surface nor at a uniform distance from the bottom electrode. To account for the two effects a more general geometric contact factor is considered, in order to go beyond the widely used effective contact area.[86,88–90]

The shape of Au electrodes produced by photolithography is not a simple, flat, disk. Instead the top surface is more like a dome with an outer flat rim and edge wall (Figures 4.24 and 4.25). The disks have a relatively flat center, 185 ± 5 nm thick, gradually decreasing radially to as thin as 15 nm around the edge, and surrounded by an thin, tall, wall on the outer edges (black trace in Figure 4.25c). The large difference in thickness between the outer rim and the center, as well as the large thin edge wall, is evidently the result of a geometric shadowing effect between the photoresist pattern and the Au deposition angle. During the printing process, pads are deformed from their circular shape and 'curl up' on one side due

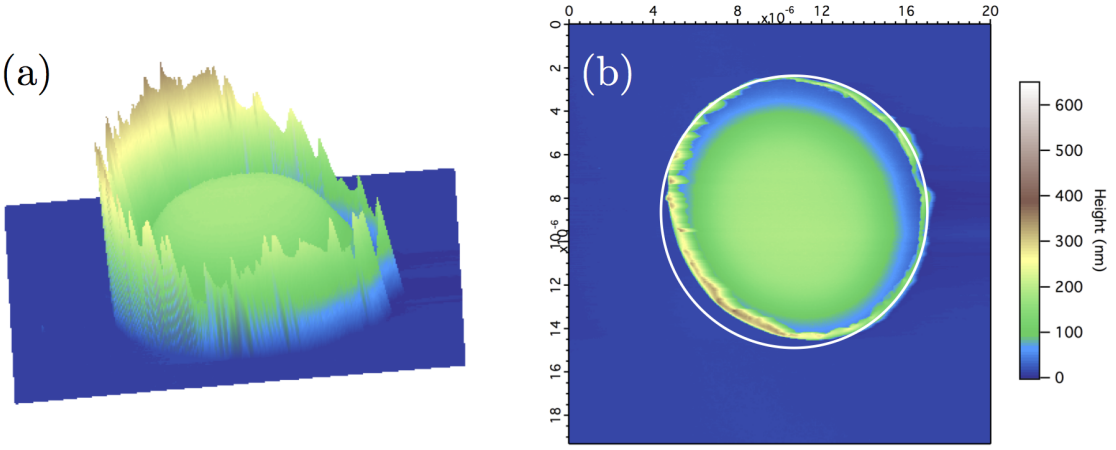

Figure 4.24: (a) A 3D rendered AFM height map of a KTP pad printed on a Si substrate. The edge walls of the pad are larger on one side, characteristic of all printed pads. (b) A top-down view of the pad rendered in (a). The pad is deformed from its circular shape (a white circle is drawn to guide the eye), with the edge wall growing largest where deformation occurs. This is due to the edge of the pad 'curling up' as the stamp is removed. In an array of printed pads, the highest side of the edge wall as well as deformation from the circular shape occur on the same side of all pads, due to the lift off process during printing.

to the printing process. Lifting off of the PDMS stamp during printing is done in a 'peeling' motion which preferentially lifts one side of each pad, causing a deformation from a circular shape and increasing the size of the "edge-wall" (Figure 4.24).

The bottoms of the as-fabricated Au electrodes are expected to be conformal to the donor Si substrates (as is typical with evaporated electrodes)[86] and thus flat. The KTP process that involves lift-off from the donor substrate and transfer to the CPB film causes the Au electrode to deform vertically (in contrast to the deformation caused the "peeling" motion during printing), leading to a buckled surface on the bottom of the electrode (Figure 4.25). These deformations are observed, to varying degrees, in ~60% of electrodes printed on CPB films and can be characterized as primarily bending and buckling, because other deformations of the Au electrode (in particular, a compressive change of thickness) would require a substantially greater force and stress than that used in KTP. This assumption

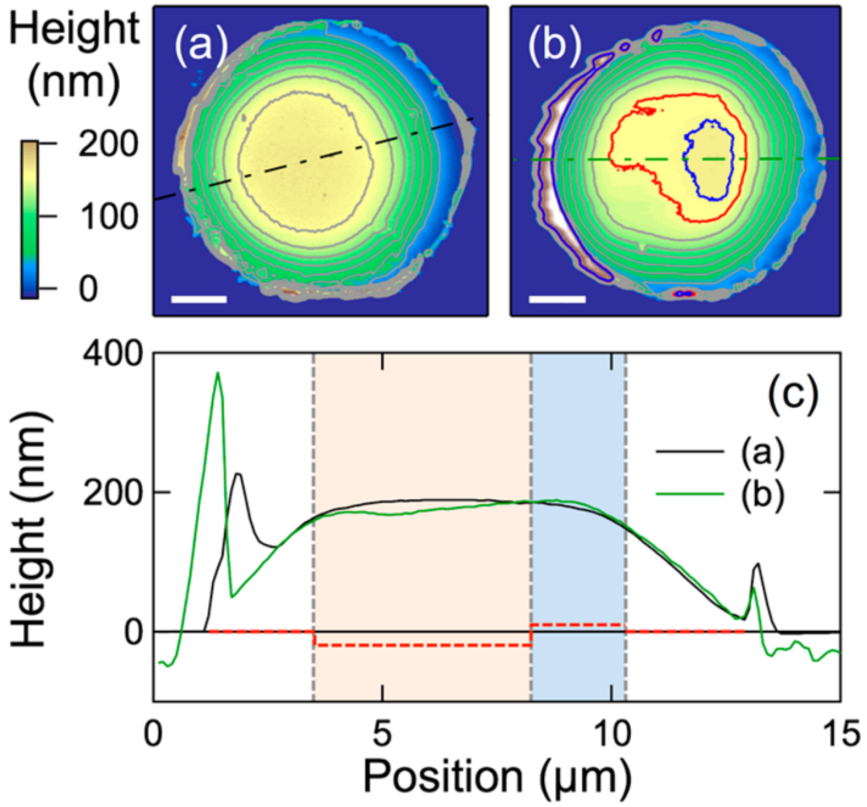

Figure 4.25: Representative AFM topography images of the KTP Au electrodes. (a) The undeformed, as-fabricated Au electrode on the donor Si substrate after HF etch and (b) a printed Au electrode on a 55 nm thick P3MT CPB film. In (a) and (b), the horizontal scale bars correspond to 2 μm, and the gray contours are spaced at 20 nm intervals. (c) Comparison between linescans of the as-fabricated (black) and the printed (green) Au electrodes (positions of linescans indicated by dot-dashed lines in (a) and (b)). Linescans are obtained along the high-symmetry axis of each pad. The zero height corresponds to the bottom of the as-fabricated electrode, while the red horizontal dashed lines approximate the bottom height of the deformed electrode. The blue and red contours in (b) correspond to deformed regions and to the light blue and pink shaded regions in c, respectively. Figure 5 in Ref [54], reproduced with permission.

that the KTP process does not cause a change in the thickness of the printed electrode is supported by the observation that none of the Au electrodes are deformed by KTP when printed onto flat Si substrates (Figure 4.26). Therefore, any deviations between the shape of the printed electrode surface (i.e. top of the electrode) and the as-fabricated counterpart caused by printing onto the rough CPB film are expected to be mirrored on the bottom of the printed electrode. The buckling is likely due to the tall columns in the brush, which can

rise >100 nm above the surrounding brush surface, comparable to the thickness of the KTP pads.

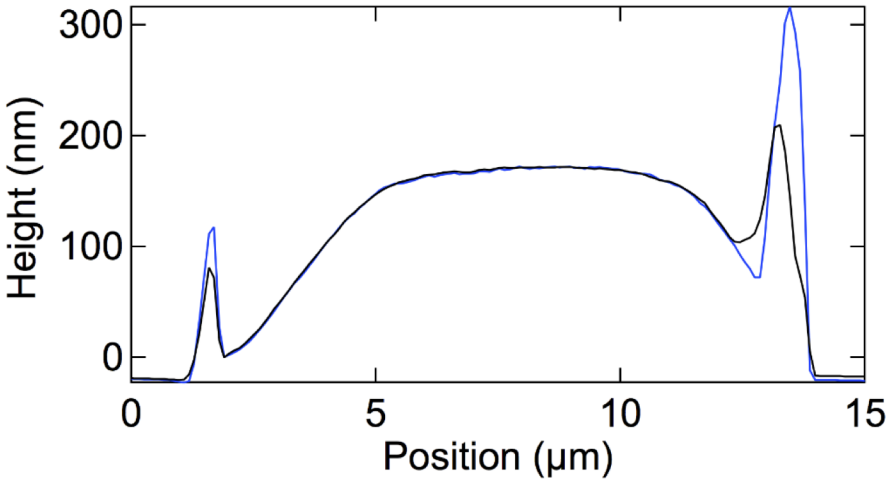

Figure 4.26: Representative comparison between AFM linescans of an as-fabricated (black) Au electrode and a Au electrode printed on a smooth Si wafer (blue) with an RMS roughness of 0.6 nm. The zero height corresponds to the reference point used to align the "master" undeformed electrode profile with the printed electrode profile. Within experimental uncertainty caused by thickness variation from electrode to electrode, there is no deformation in the electrode printed on flat Si compared to the as-fabricated electrode. Figure S14 in Ref [54], reproduced with permission.

Because of the aforementioned vertical deformation, the separation distance between the two electrodes in CPB devices varies from position to position within a given device (Figure 4.25c). To account for this variation, each deformed CPB device is divided into regions of parallel resistors, each with its own "regional" effective contact area (A_i) and thickness (i.e. separation between electrodes, L_i). The "regional" effective contact area A_i is generally smaller than the corresponding "regional" area of the electrode, owing to the surface roughness of the underlying CPB film, such that the total effective contact area of the device, $\Sigma_i A_i$, is far less than the area of the undeformed electrode, A_0.

For each device, the values of L_i were estimated from the deformed bottom height of the printed electrode (Figure 4.25c) to the ITO surface. Tall columns in the CPB film reach

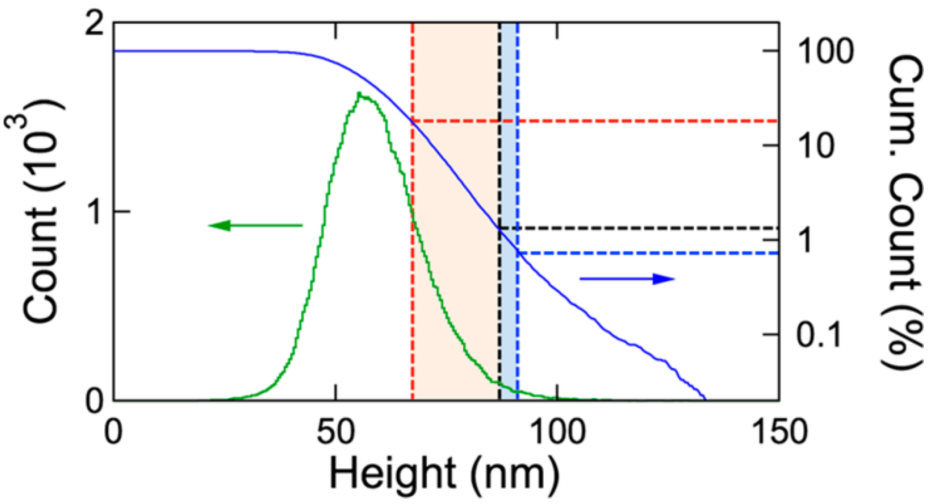

Figure 4.27: Typical surface height histogram (green) and corresponding normalized cumulative histogram (blue, cumulative from the highest point of the image) of a 55 nm thick P3MT CPB film and intersection with a deformed, printed Au electrode (shown in Figure 4.25). The zero height is at the surface of the ITO substrate. Vertical dashed lines correspond to the estimated "regional" heights of the bottom of the top electrode (L_i in the text). The horizontal dashed lines indicate the respective area fractions of the CPB film making contact with the top electrode (A_i in the text). The blue and red dashed lines correspond to the contacts of the deformed parts of the electrode from Figure 4.25, whereas the black dashed lines correspond to that of the undeformed part. Figure 6 in Ref [54], reproduced with permission.

heights above L_i and thus make contact with the top electrode. Given that the elastic modulus of the Au electrode (∼80 GPa) is likely to be much larger than that of P3MT (the elastic modulus of P3HT is ∼1 GPa),[91,92] the columns above L_i are assumed to compress down to the bottom of the Au electrode, while compression of the Au electrode is negligible. This assumption serves as an upper bound for the amount of contact between the CPB film and Au electrode, as any compression of the Au electrode that is ignored here would cause an increase in L_i and a decrease in the contact factor below.

Because only the tallest portion of the CPB films are in contact with the Au electrode, values of L_i are greater than the nominal film thickness, L_0. These tall columns represent a small fraction of the film surface area, causing the "regional" effective contact area A_i to depend on L_i. The surface height histogram and the corresponding cumulative histogram

were used to determine A_i for a given L_i (Figure 4.27). Specifically, A_i is the area fraction of the CPB film (horizontal dashed lines) that is above L_i (vertical dashed lines). Assuming that there is uniform resistivity (ρ) across all regions within each device, the resistance R consisting of parallel resistors is given by

$$R = \rho \frac{L_0}{A_0} \frac{1}{a}, \tag{4.1}$$

and

$$a = \sum_i \frac{A_i/A_0}{L_i/L_0}, \tag{4.2}$$

where a is the effective contact factor introduced as a correction to the nominal resistance of the device. The contact factor is an appropriate correction to device resistance as long as device resistivity is constant (i.e. the I-V behavior is linear. Resistivity is extracted from resistance vs length plots by taking the slope ($\frac{\rho}{A_0 a}$) and multiplying by A_0 * a. For devices with non-linear I-V behavior, resistivity has an electric field dependence, i.e. ρ becomes $\rho(E_i) = \rho(\frac{V}{L_i})$, and equations 4.1 and 4.2 become

$$R(V) = \frac{L_0}{A_0} \frac{1}{a(V)}, \tag{4.3}$$

and

$$a(V) = \sum_i \rho(\frac{V}{L_i}) \frac{A_i/A_0}{L_i/L_0}, \tag{4.4}$$

where V is the bias across the device. Unless the electric field dependence of resistivity is known the contact factor cannot be determined for devices with non-linear I-V behavior. For these devices, ρ generally monotonically increases with the field, and therefore as the field increases, the relative contribution to the contact factor from the thinnest regions of the device increases. For this reason, the device thickness d is defined as the thickness of

the thinnest region of the sample, which is often the region that contributes the most to the zero-field contact factor. Both d and L_0 were measured for many devices (Table 4.1), and the average device thickness d was found to be 1.5 $\pm$ 0.3 times greater than L_0.

CPB devices exhibit linear I-V behavior at low bias, and thus low fields, and so the contact factor determined by equations 4.1 and 4.2, named the "zero-field contact factor", is applicable to low field measurements. The zero-field contact factor was determined for KTP devices on CPB films. The analysis of many samples and devices indicates that the average value for the effective contact area (i.e. $\Sigma_i A_i/A_0$) is 2% and is independent of the CPB film thickness. The zero-field contact factor a is also independent of film thickness, with a log average value of -2.0 $\pm$ 0.6, corresponding to an average value of 1% with lower and upper bounds of 0.25% and 4% (Table 4.2). These findings are likely the result of the observed film thickness independent column density and cross-sectional area and the resulting mechanical properties of the columns, combined with the consistency of the KTP process.

Table 4.1: Comparison of nominal film thickness (L_0) and device thickness (d)

	CPB Thickness L_0 (nm)	Device Thickness d (nm)	Ratio d/L_0
	8	11	1.4
	8	12	1.5
	15	30	2
	15	31	2.1
	18	29	1.6
	32	41	1.3
	32	46	1.4
	56	81	1.4
	56	82	1.5
	68	84	1.2
	68	95	1.4
Average	-	-	1.5 $\pm$ 0.3

Table 4.2: Zero-field contact factor for KTP devices on CPB films

Brush Thickness	Effective Contact Area		Contact Factor	
	Percent (%)	Log(Percent)	Percent (%)	Log(Percent)
8	4.5	-1.3	3.5	-1.5
8	1.7	-1.8	1.1	-2.0
15	0.4	-2.5	0.2	-2.7
15	0.1	-3.0	0.04	-3.4
18	0.7	-2.2	0.4	-2.4
32	4.2	-1.4	3.1	-1.5
32	2.0	-1.7	1.5	-1.8
56	2.2	-1.7	1.7	-1.8
56	2.3	-1.6	1.6	-1.8
68	4.0	-1.4	3.3	-1.5
68	7.7	-1.1	6.0	-1.2
Average	2	-1.8 ± 0.5	1	-2.0 ± 0.6

4.2.2: Bulk Resistivity and Molecular Resistivity for P3MT CPBs

The bulk resistivity value along the P3MT CPB columns has been calculated to be 1.4 x 10^5 Ω-cm (lower and upper bounds of 0.4 and 5.6 x 10^5 Ω-cm, respectively) by using equations 4.1 and 4.2, $\frac{\rho}{A_0 a}$ = 1.0 M Ω/nm (slope of Figure 4.19a), A_0 = 120 μm^2, and a = 1%. This value is 2 orders of magnitude lower than the typical room temperature values for spuncast, atmospherically doped P3HT films measured using 4-point probe and Van der Pauw techniques. However, the latter in-plane, 4-terminal techniques are not compatible for studying vertical intramolecular transport through P3MT CPBs.[93] Note that since resistivity of P3MT CPB devices is determined from the slope of the resistance versus thickness plot, contact resistance and other interfacial effects (e.g. the size of the injection barrier at the interface) are factored out.

The intrinsic carrier concentration in poly(3-alkylthiophene)s has a weak dependence on the side chain structure,[94,95] so the observed large reduction in the bulk resistivity of P3MT CPBs provides evidence for a corresponding enhancement of mobility in the P3MT CPB films compared to spun-cast P3HT. Furthermore, improvements on the vertical chain alignment of P3MT chains through efforts to optimize synthetic parameters may lead to even higher

values of mobility in these films.

To compare the conduction along P3MT CPBs with single molecule/ensemble devices in which intramolecular hopping has been reported to dominate charge transport processes, the average resistance along individual polymer chains as a function of length (i.e. molecular resistivity) was estimated.

Molecular resistivity (ρ_{mol}) is a measure of the resistivity of molecular wires, and is calculated by treating each molecular wire in a device as a parallel resistor. Molecular resistivity is calculated by

$$\rho_{mol} = \rho N_c \tag{4.5}$$

where ρ is the bulk resistivity and N_c is the areal density of molecules/wires within the device. Convenient units for ρ_{mol} are GΩ/nm^{-2} per molecule. For the P3MT CPB films, we assume the monomer density of the bulk to be the same as that at the surface of the substrate. Cyclic voltammetry measurements show the chain grafting density to be 1.3 nm^{-2}, which is used as N_c to convert the bulk resistivity value to a molecular value of 180 GΩ/nm (with lower and upper bounds of 45 and 700 GΩ/nm, respectively) per P3MT molecule. Again, this estimate assumes that the polymer chain density stays constant during film growth and that the device thickness is equal to the polymer chain length, both of which would overestimate the value for molecular resistivity.

Although neither factor can be quantified at this time, Pd desorption during polymerization likely causes a reduction in chain density as the film grows (resulting in a lower N_c). The polymer chains in these films also likely undergo significant twisting and winding between the bottom and top electrodes, as they are significantly tilted away from vertical and disordered (from the spectroscopy experiments described above), so the polymer chain lengths within the columns are evidently much longer than the device thickness (again, as mentioned above the molecular weight of the P3MT polymer cannot be directly measured owing to its insolubility). Therefore, the estimated molecular resistivity value for P3MT should be con-

sidered as an upper bound. However, this value is already comparable to short, conjugated molecular wires that exhibit predominantly intramolecular charge transport (Table 4.3).

Table 4.3: Comparison of molecular resistivity

Molecule	Length Range (nm)	Molecules in Junction	Molecular Resistivity (GΩ / nm)	Reference
OPI	4.7 - 7.5	∼100	340	[96]
ONI	4.2 - 10.5	∼100	200	[51]
P3MT Brush	5 - 150	$\sim 10^6$	180	this work
Polyflourine	20	1	58	[97]
OPT	6 - 10	∼100	40	[53]

Section 4.3: I-V Behavior as Finite Bias

At finite biases, the devices deviate from the linear I-V behavior, and exhibit some asymmetry between the bias directions. The observed asymmetry arises from the CPB morphology and the asymmetry in the interfacial barriers between the CPB and the electrodes. Specifically, for the CPB devices, the bottom electrode is in contact with all of brush, while the top electrode only contacts ∼2% of them. This discrepancy in contact area between the two electrodes leads to asymmetry. In order to understand the origin of this asymmetry, an understanding of the injection barriers and the energy landscape within the brush, as seen by the charge carrier, is essential.

4.3.1: Energy Level Structure of CPB Devices

Due to the HOMO (-4.9 eV) and LUMO (-3.0 eV) energy levels of P3MT CPBs[98] and the work function of the ITO substrate (4.62 eV)[99] and Au electrode (∼ 5eV),[100] the CPB devices are expected to exhibit unipolar hole transport. The phosphonic acid monolayer is expected to create a thin (< 1nm), but a high injection barrier at the ITO interface.[99] The vacuum level alignment model predicts a CPB injection barrier height of ∼300 mV, though

the interfacial energy landscape is more complicated. Further experiments are necessary to elucidate the interfacial barriers between the CPB and the electrodes.

When the device is forward biased, holes are injected from the ITO into the CPB film. Conversely, when the device is reverse biased holes are injected into the brush from the Au electrode. However, only a small fraction of the brush is in contact with the Au electrode, so large regions of the device have a vacuum/air barrier separating the brush from the top electrode. This makes injection from the Au electrode into these regions difficult, and extraction of charge from these region into the Au electrode difficult as well. An energy diagram for holes within the devices is shown in Figure 4.28.

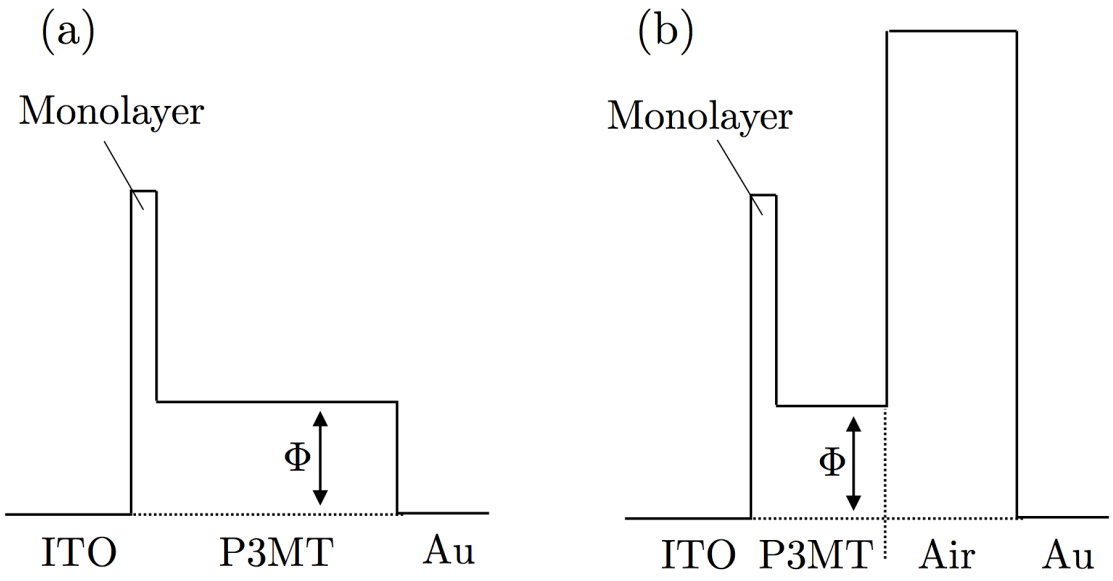

Figure 4.28: (a) Energy diagram for holes in the CPB columns. ϕ is the energy difference between the fermi level and the HOMO level of the CPB. Only ~2% of the top electrode is in contact with the brush, and so for regions of the brush that are not in contact with the Au electrode, the energy diagram looks like (b).

For the forward bias direction, holes that are injected into the CPB from the ITO electrode experience a large vacuum barrier for ~98% of the device (Figure 4.29). They can travel through the tall columns contacting the top electrode, or they can build up within the brush due to the presence of the large vacuum barrier. This charge build up does not

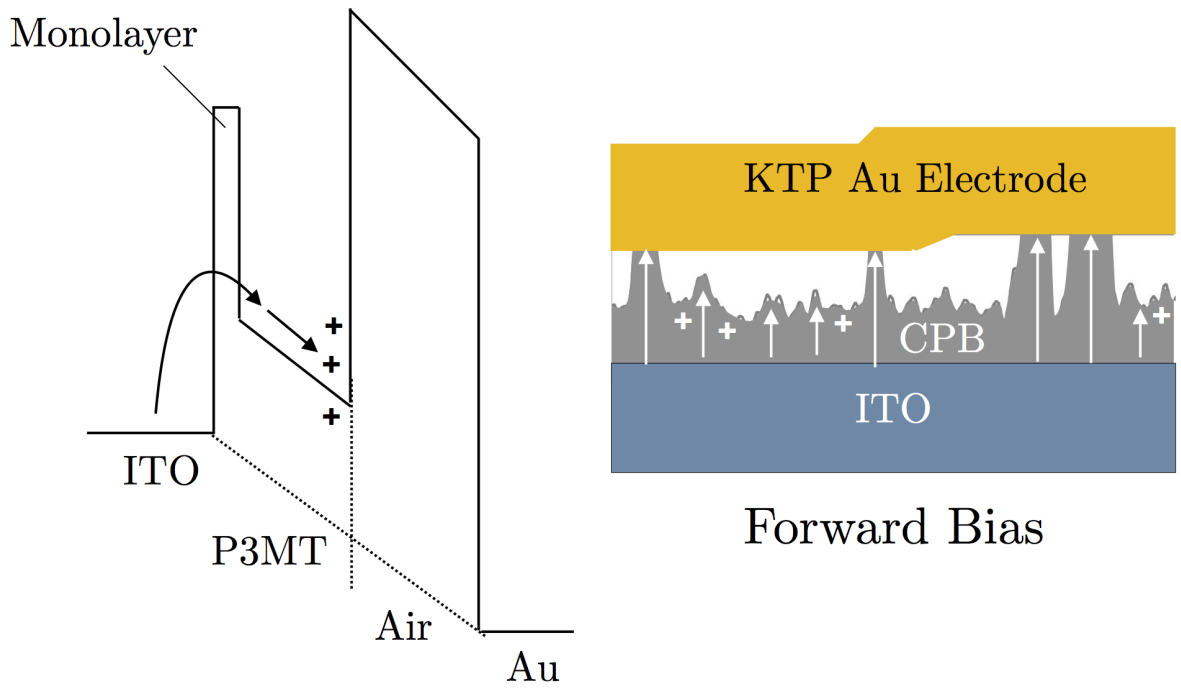

Figure 4.29: CPB device energy landscape as seen by holes under forward bias. Holes are injected from the ITO electrode into the CPB. Some of the holes travel through the tall columns to the Au electrode, while others build up within the brush due to a large vacuum barrier separating the CPB from the Au electrode.

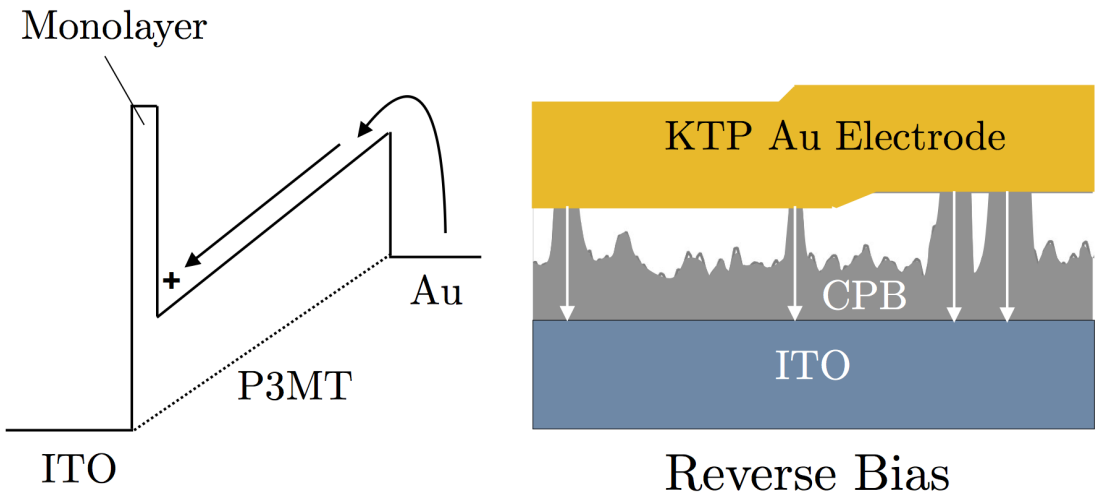

Figure 4.30: CPB device energy diagram as seen by holes under reverse bias. Holes are injected from the Au electrode into the tall columns and travel to the bottom ITO electrode.

occur to the same degree when charge is injected from the top electrode since there is not a large vacuum barrier preventing charge extraction at the ITO interface (Figure 4.30). The larger hysteresis in the forward bias direction supports the notion of charge buildup within the brush.

4.3.2: The Injection Limited Current Model

Due to the morphology induced charge buildup in CPB devices in the forward bias direction, the finite-bias I-V behavior of the devices is difficult to model. However, the reverse bias behavior does not exhibit the same charge buildup, and can be explained with the widely used injection limited current (ILC) model.[40] The current density (J) predicted by the injection limited current model is given by

$$J = 4\psi^2 N_0 q\mu E e^{(-\phi_B/kT)} e^{f^{1/2}}, \tag{4.6}$$

$$f = \frac{q^3 E}{4\pi\epsilon\epsilon_0 (kT)^2}, \tag{4.7}$$

$$\psi(f) = f^{-1} + f^{-1/2} - f^{-1}(1 + 2f^{1/2})^{1/2}, \tag{4.8}$$

where the parameters are respectively: ϵ_0 the vacuum permittivity, k the Boltzmann constant, $T$the temperature, q the elementary unit charge, ϵ the relative dielectric constant of the material, N_0 the charge carrier concentration, E the electric field, and ϕ_B the effective injection barrier.[40] To apply the ILC model to the I-V measurements equation, 4.9 is derived in Appendix B. The ILC model then becomes

$$I = \alpha V_{adj} \gamma(\frac{V_{adj}}{\eta}), \tag{4.9}$$

$$\alpha = \frac{A}{d} N_0 q \mu e^{(-\phi_b/kT)}, \tag{4.10}$$

$$\eta = \epsilon d, \tag{4.11}$$

where $V_{adj} = V - V_d$, α is a scaling prefactor, η is a "thickness factor" and γ is a function derived in Appendix B. As V_{adj} goes to 0, γ approaches to 1, and so α is equivalent to the minimum conductance found previously. As V_{adj} increases, the deviation from linear I-V behavior is described by γ and the thickness factor η (i.e. the device thickness and dielectric constant). While α cannot give more information than can be found by a linear fit of the I-V curves near zero field, the deviation described by γ can give additional information.

The ILC model (equation 4.9) was applied to both the forward and reverse bias of I-V measurements on CPB devices with α and η as free parameters. An ILC fit on a CPB device with a device thickness d of 33 nm is shown in Figure 4.31. While the reverse bias is well described by the ILC model, the forward bias deviates from the ILC behavior outside of the linear regime. The ILC model fails to describe the I-V behavior for devices with $d < 15$ nm (Figure 4.32). This is consistent with the observation that these devices are in a transition region, where charge transport is transitioning from tunneling to diffusive.

The thickness factor η depends on the device thickness d, and not nominal brush thickness L_0. On average, the thickness of each device are 1.5 times greater than the CPB film thickness (Table 4.1). Figure 4.33 shows the thickness factor ($\eta = \epsilon d$) vs. estimated device thickness d. The slope of a linear fit corresponds to ϵ, and gives a value of 2.5 ± 0.2, which is consistent with known values.[40] Thus the ILC model is self consistent, with the ILC derived thickness factor consistent with the expected thickness factor based on estimated device thickness and dielectric constant.

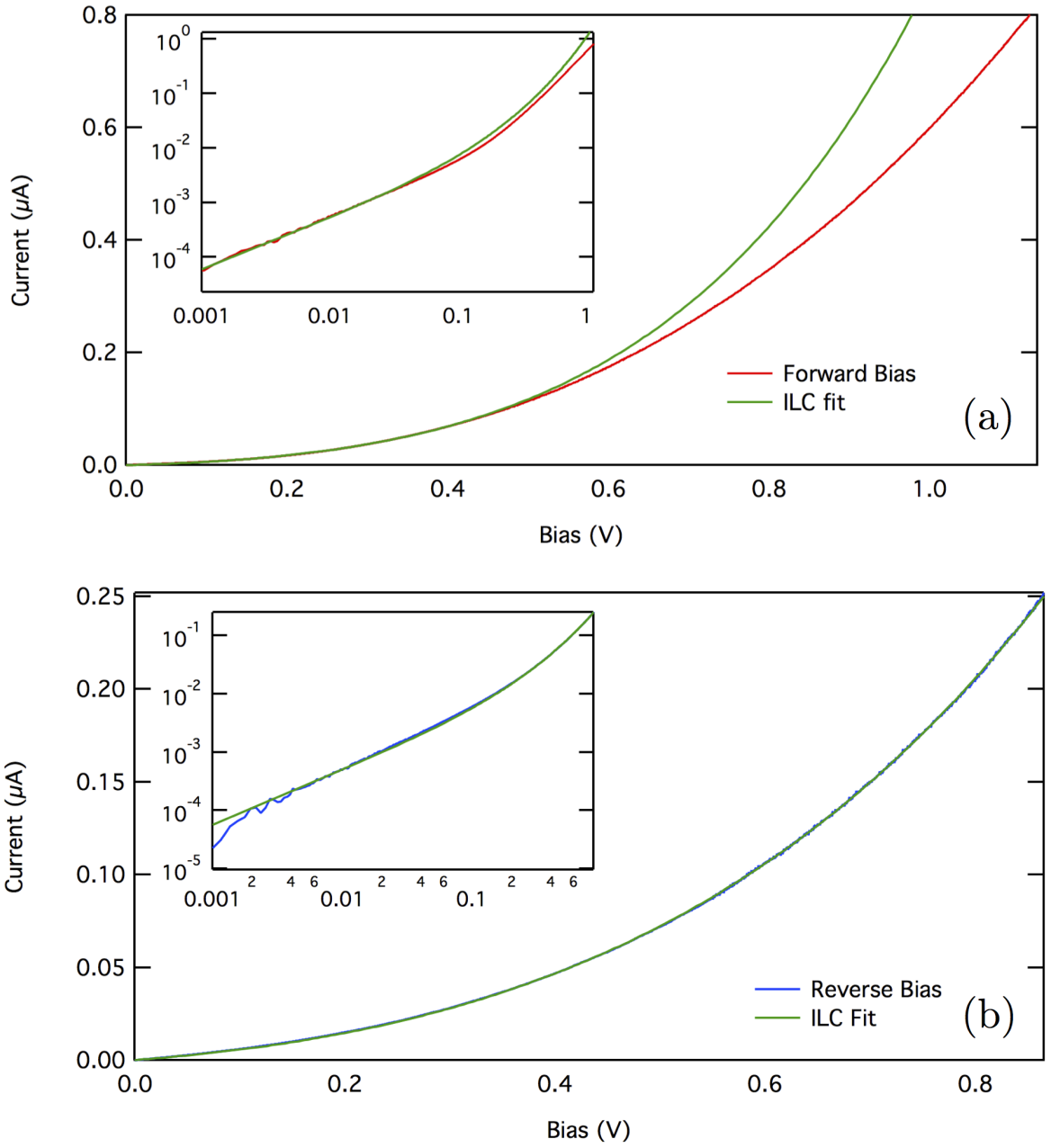

Figure 4.31: ILC fits for a CPB device with device thickness d of 33 nm (a) for the forward bias behavior and (b) ILC fit for the reverse bias direction. The insets shows the log scale. The fit is very good on the full range of data, up to ~ 1 V. The inset shows the same plot in log scale.

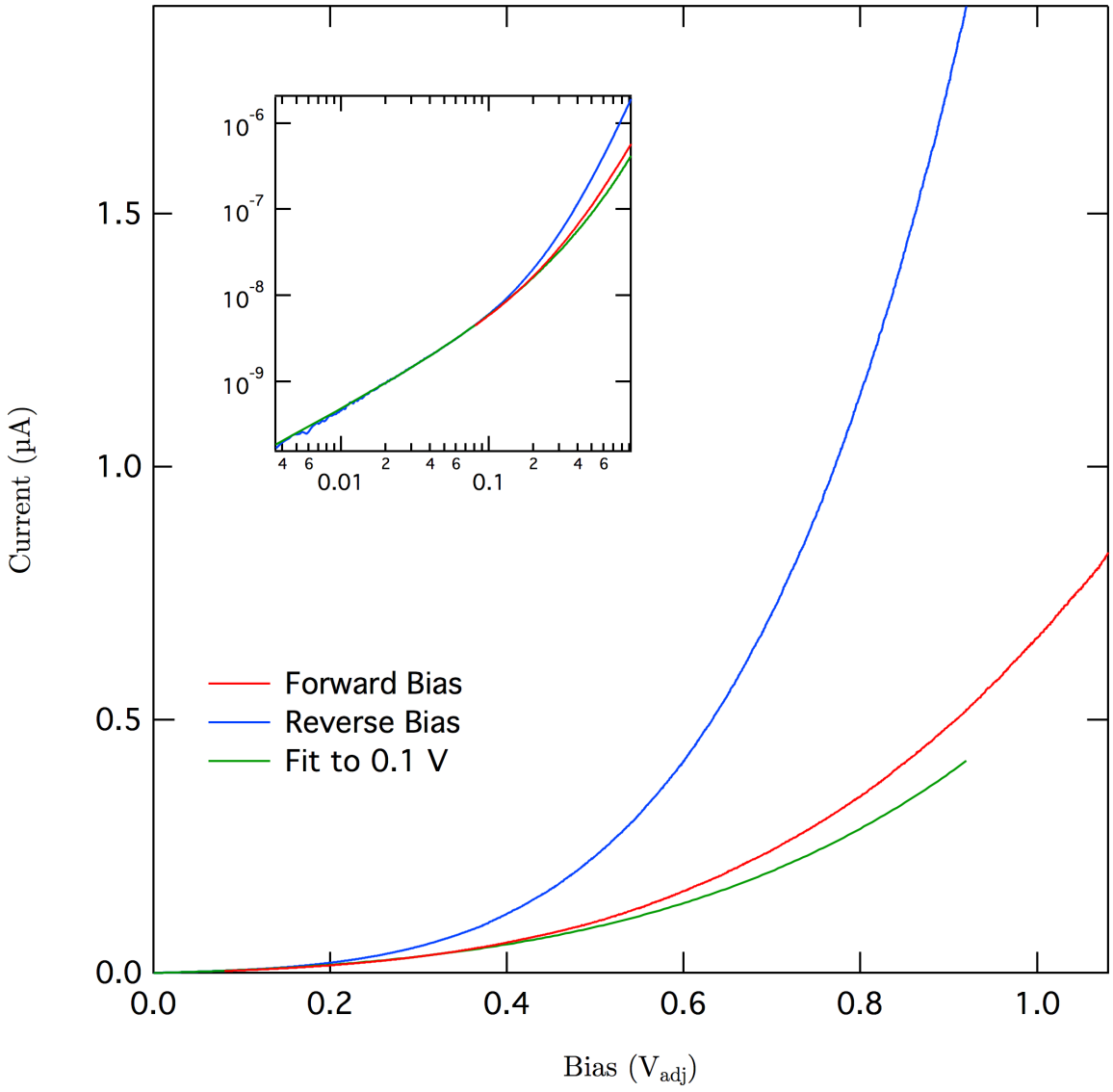

Figure 4.32: ILC fits for the reverse bias of a CPB device with a device thickness d of 12 nm. The inset shows the same plot in log scale. The fits for low bias do not explain behavior above $\sim$ 150 mV (green curve).

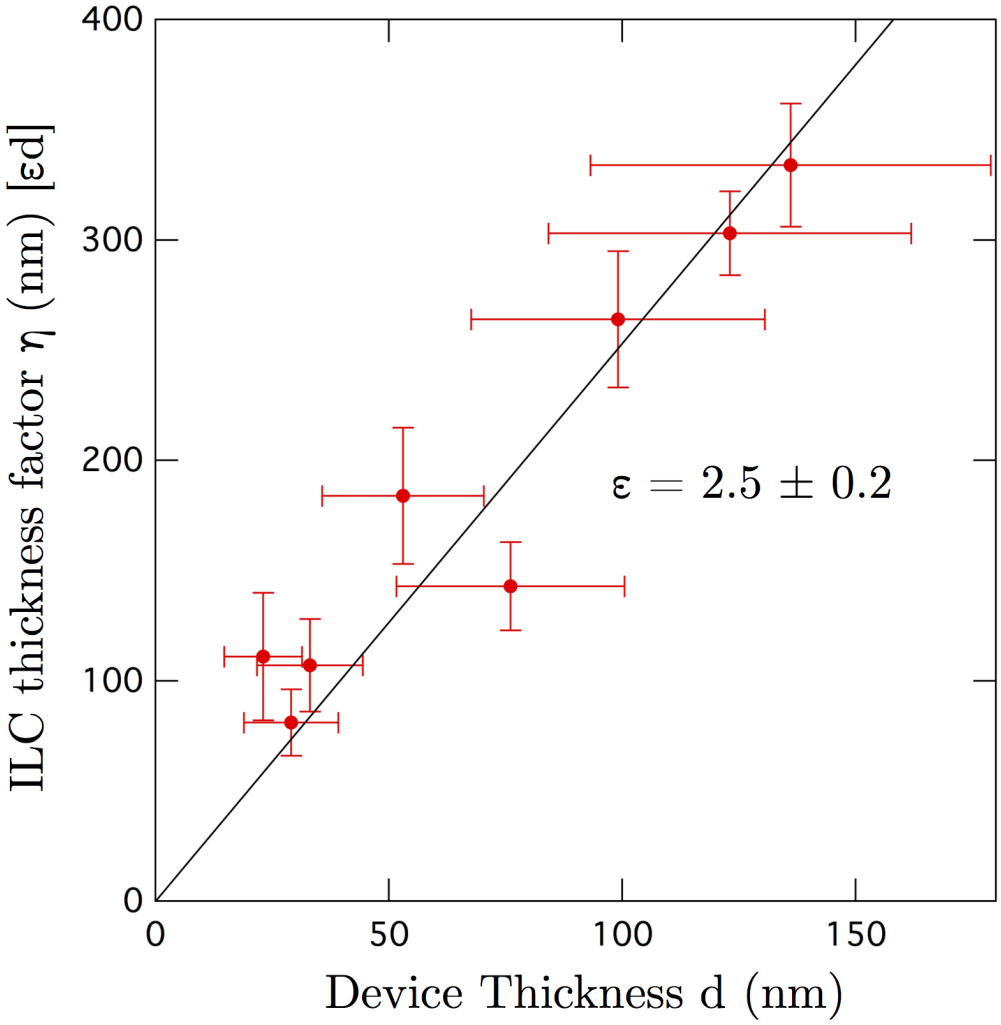

Figure 4.33: The extracted thickness parameter from the ILC model compared to device thickness d, determined from AFM pad topography analysis. The slope of the graph gives a reasonable estimate for ϵ.

Section 4.4: Summary

The observed reduction in the CPB bulk resistivity compared to that of spun cast counterparts, and the low molecular resistivity value in the P3MT CPB devices, support the notion that intramolecular charge transport processes are responsible for enhancing charge transport through CPB films. The primary enabling factor is that all of the P3MT molecules in contact with the top Au electrode are covalently bound to the bottom ITO electrode. Investigations to date have focused on characterizing intramolecular charge transport processes in molecular wires less than 10 nm long and in devices containing <100 molecules (often single molecules). This work on P3MT CPB devices has incorporated orders of magnitude more molecular wires reaching lengths well over 100 nm, demonstrating that the CPB devices constitute a novel and scalable platform for studying intramolecular transport phenomena.

The bias direction dependent transport behavior of CPB devices has been examined. When charge is injected from the top electrode the I-V behavior can be fit by the ILC model. However, when charge is injected from the bottom electrode, charge buildup appears to take place within the devices, and the ILC model is no longer sufficient to describe the charge transport behavior. This asymmetry is explained in terms of non-conformal electrodes and the columnar CPB surface. While the entire bottom electrode in each device is in contact with the CPB, the top electrode contacts only ∼2% of the CPB film (i.e. the tall columns). Charge injected into the columns from the top electrode has a "direct" path to the bottom electrode, but charge injected into the CPB from the bottom electrode builds up within the film.

CHAPTER 5: CONCLUSIONS

The morphology, and the structural and electrical properties of P3MT conjugated polymer brushes (CPBs) have been studied. Early in CPB film growth, the formation of columns is observed on the film surface. Analysis of the columns indicates that they exhibit a characteristic size and density that is independent of film thickness, whereas the column height distribution scales with film thickness. We expect that the column characteristics may be tuned by changing various synthetic parameters during polymerization. Electrical conduction through the columns have been studied using the electrode-CPB-electrode devices with Au electrodes printed on top of the CPB films.

The interface between the Au electrode and the CPB film has been examined in order to address the deformation of the Au electrodes during device fabrication. After correcting for the deformation of the top electrode using a contact factor, the bulk resistivity along the columns has been estimated to be about 100 times lower than the typical values for spun-cast, poly(3-alkylthiophene) films. Furthermore, the resistance along individual P3MT polymer chains in the conjugated polymer brush films has also been estimated to be comparable to the literature values for very short (<10 nm) molecular wires. These findings suggest the presence of enhanced intramolecular conduction along P3MT polymer chains, thus making conjugated polymer brush films a promising and unexplored platform to study the interplay among the synthetic conditions, film morphology, and structure, and intramolecular charge transport.

Finally, the I-V behavior of CPB devices has been studied. When charge is injected from the top electrode, the transport appears to follow the ILC model. However, when charge is injected from the bottom electrode, charge buildup occurs within the devices, and the ILC model is no longer appropriate. This ihas been explained by the presence of tall columns in

the CPB surface. Specifically, while the entire bottom electrode in each device is in contact with the CPB, the top electrode contacts only ∼2% of the CPB film (i.e. the tall columns). Charge injected into the columns from the top electrode has a "direct" path to the bottom electrode, but charge injected into the CPB from the bottom electrode builds up within the short columns that do not contact the top electrode.

APPENDIX A: COLUMN IDENTIFICATION ALGORITHM

```
Function columns_at_height(image, height)
    wave image
    variable height

    // initialization
    Duplicate/O image column_mask
    column_mask[] = 0
    Make/Free/N=(numpnts(image)) queue_x, queue_y
    queue_x[] = 0
    queue_y[] = 0
    variable r,c, counter = 0, columns = 0

    // main algorithm loop
    for(r=0; r<dimsize(image,0);r+=1)
        // print(r)
        for(c=0; c<dimsize(image,1);c+=1)
            if(image[r][c] < height || column_mask[r][c] > 0)
                continue
            endif

            columns = columns + 1
            column_mask[r][c] = columns
            queue_x[] = 0
            queue_y[] = 0
            counter = insert(counter, queue_x, queue_y, r, c)
```

```
// column flood-fill routine
do
    variable x = queue_x[0]
    variable y = queue_y[0]
    counter = pop(counter, queue_x, queue_y)

    if(x-1 > 0 && column_mask[x-1][y] == 0 && image
       [x-1][y] > height)
        column_mask[x-1][y] = columns
        counter = insert(counter, queue_x, queue_y,
            x-1, y)
    endif

    if(x+1 < dimsize(image,0) && column_mask[x+1][y
       ] == 0  && image[x+1][y] > height)
        column_mask[x+1][y] = columns
        counter = insert(counter, queue_x, queue_y,
            x+1, y)
    endif

    if(y-1 > 0 && column_mask[x][y-1] == 0 && image
       [x][y-1] > height)
        column_mask[x][y-1] = columns
        counter = insert(counter, queue_x, queue_y,
            x, y-1)
    endif
```

```
                if(y+1 < dimsize(image,1) && column_mask[x][y
                   +1] == 0 && image[x][y+1] > height)
                    column_mask[x][y+1] = columns
                    counter = insert(counter, queue_x, queue_y,
                        x, y+1)
                endif

            while(counter > 0)
        endfor
    endfor

    return columns
End
```

APPENDIX B: I-V ADAPTATION OF THE ILC MODEL

The ILC model[40] is given by

$$J = 4\psi^2 N_0 q\mu E e^{(-\phi_B/kT)} e^{f^{1/2}} \tag{B.1}$$

$$f = \frac{q^3 E}{4\pi\epsilon\epsilon_0 (kT)^2} \tag{B.2}$$

$$\psi(f) = f^{-1} + f^{-1/2} - f^{-1}(1 + 2f^{1/2})^{1/2} \tag{B.3}$$

where J is the current density, ϵ_0 is the vacuum permittivity, k is the Boltzmann constant, T is the temperature, q is the elementary unit charge, ϵ is the relative dielectric constant of the material, N_0 is the charge carrier concentration, E is the electric field, and ϕ_B is the effective injection barrier. As f approaches 0, $\psi(f)$ approaches 1/2 and $exp(f^{1/2})$ approaches 1. The ILC model then becomes

$$lim_{f\to 0} J(f) = N_0 q\mu e^{(-\phi_b/kT)} E = \sigma_{ILC} E \tag{B.4}$$

$$\sigma_{ILC} = N_0 q\mu e^{(-\phi_b/kT)} \tag{B.5}$$

where σ_{ILC} is the low-field conductivity. The presence of a Boltzmann factor in the conductivity is due to the high barrier that must be over come for charge to be injected from the electrodes into the CPB. The ILC model can be rewritten as

$$J = \sigma_{ILC} E \gamma'(f) \tag{B.6}$$

$$\gamma'(f) = 4\psi^2(f) e^{f^{1/2}} \tag{B.7}$$

where $\gamma'(f)$ is a function that describes the deviation from ohmic behavior at high fields.

To apply the ILC model to I-V measurements, the applied bias and measured current must be converted into a field and current density. The field within the device is assumed to be $E = (V - V_{bi})/d = V_{adj}/d$ where d is the device thickness, and the current density is given by $J = I/A$ where A is effective contact area of the electrode area. The ILC model becomes

$$I = \alpha V_{adj} \gamma(\frac{V_{adj}}{\eta}) \tag{B.8}$$

$$\alpha = \frac{A}{d}\sigma_{ILC} \tag{B.9}$$

$$\gamma(V/\eta) = \gamma'(\frac{cV}{\eta}) \tag{B.10}$$

$$c = \frac{q^3}{4\pi\epsilon_0(kT)^2} \tag{B.11}$$

$$\eta = \epsilon d \tag{B.12}$$

where α is a scaling prefactor and η is a "shape factor". α and η are the two free parameters in ILC fits of I-V curves.

BIBLIOGRAPHY

[1] (Apr. 2018) http://www.nobelprize.org/nobel_prizes/chemistry/laureates/2000/.

[2] (Apr. 2018) https://www.alliedmarketresearch.com/press-release/organic-electronics-market-is-expected-to-reach-79-6-billion-global-by-2020-allied-market-research.html.

[3] S. Tiwari and N. C. Greenham, "Charge mobility measurement techniques in organic semiconductors", Optical and Quantum Electronics **41**, 69 (2009).

[4] J. Terao, A. Wadahama, A. Matono, T. Tada, S. Watanabe, S. Seki, T. Fujihara, and Y. Tsuji, "Design principle for increasing charge mobility of ??-conjugated polymers using regularly localized molecular orbitals", Nature Communications **4**, 1691 (2013).

[5] H. Bässler and A. Köhler, "Charge transport in organic semiconductors", in *Unimolecular and supramolecular electronics i: chemistry and physics meet at metal-molecule interfaces*, edited by R. M. Metzger (Springer Berlin Heidelberg, Berlin, Heidelberg, 2012), pp. 1–65.

[6] S. Rughooputh, M. Nowak, S. Hotta, A. Heeger, and F. Wudl, "Soluble Conducting Polymers: the poly(3-alkylthienylenes)", Synthetic Metals **21**, 41 (1987).

[7] (Apr. 2018) http://polymerdatabase.com/polymer%20physics/MW%20Properties.html.

[8] M. Rubinstein and R. H. Colby, *Polymer Physics* (Oxford University Press: New York, 2003).

[9] P. A. Wiggins and P. C. Nelson, "Generalized theory of semiflexible polymers", Physical Review E - Statistical, Nonlinear, and Soft Matter Physics **73**, 1 (2006).

[10] I. Botiz and N. Stingelin, "Influence of molecular conformations and microstructure on the optoelectronic properties of conjugated polymers", Materials **7**, 2273 (2014).

[11] Y. Roiter and S. Minko, "AFM single molecule experiments at the solid-liquid interface: In situ conformation of adsorbed flexible polyelectrolyte chains", Journal of the American Chemical Society **127**, 15688 (2005).

[12] H. Kallmann and M. Pope, "Bulk Conductivity in Organic Crystals", Nature **186**, 31 (1960).

[13] H. Kuhn, "A quantum-mechanical theory of light absorption of organic dyes and similar compounds", The Journal of Chemical Physics **17**, 1198 (1949).

[14] C. K. Chiang, C. R. Fincher, Y. W. Park, A. J. Heeger, H. Shirakawa, E. J. Louis, S. C. Gau, and A. G. MacDiarmid, "Electrical conductivity in doped polyacetylene", Physical Review Letters **39**, 1098 (1977).

[15] A. G. MacDiarmid, R. J. Mammone, R. B. Kaner, S. J. Porter, R. Pethig, A. J. Heeger, and D. R. Rosseinsky, "The Concept of 'Doping' of Conducting Polymers: The Role of Reduction Potentials [and Discussion]", Philosophical Transactions of the Royal Society A: Mathematical, Physical and Engineering Sciences **314**, 3 (1985).

[16] T. M. Clarke and J. R. Durrant, "Charge photogeneration in organic solar cells", Chemical Reviews **110**, 6736 (2010).

[17] A. J. Mozer, N. S. Sariciftci, A. Pivrikas, R. Österbacka, G. Juška, L. Brassat, and H. Bässler, "Charge carrier mobility in regioregular poly(3-hexylthiophene) probed by transient conductivity techniques: A comparative study", Physical Review B - Condensed Matter and Materials Physics **71**, 1 (2005).

[18] W. Ten Hoeve, H. Wynberg, E. E. Havinga, and E. W. Meijer, "Substituted ..-undecithiophenes, the longest characterized oligothiophenes", Journal of the American Chemical Society **113**, 5887 (1991).

[19] F. Garnier, G. Horowitz, X. Peng, and D. Fichou, "Structural basis for high carrier mobility in conjugated oligomers", Synthetic Metals **45**, 163 (1991).

[20] R. Zuzok, W. Pukacki, and S. Roth, "Electronic Transport Properties: Stretch Oriented "New" Polyacetylene", Synthetic Materials **43**, 197 (1991).

[21] H. Letheby, "On the production of a blue substance by the electrolysis of sulphate of aniline", J. Chem. Soc. **15**, 161 (1862).

[22] C. W. Tang and S. A. VanSlyke, "Organic electroluminescent diodes", Applied Physics Letters **51**, 913 (1987).

[23] H. Koezuka, A. Tsumura, and T. Ando, "Field-effect transistor with polythiophene thin film", Synthetic Metals **18**, Proceedings of the International Conference of Science and Technology of Synthetic Metals, 699 (1987).

[24] G. Yu, J. Gao, J. C. Hummelen, F. Wudl, and A. J. Heeger, "Polymer Photovoltaic Cells: Enhanced Efficiencies via a Network of Internal Donor-Acceptor Heterojunctions", Science **270**, 1789 (1995).

[25] V. Coropceanu, J. Cornil, D. A. da Silva Filho, Y. Olivier, R. Silbey, and J. L. Brédas, "Charge transport in organic semiconductors", Chemical Reviews **107**, 926 (2007).

[26] M. L. Jones, D. M. Huang, B. Chakrabarti, and C. Groves, "Relating Molecular Morphology to Charge Mobility in Semicrystalline Conjugated Polymers", Journal of Physical Chemistry C **120**, 4240 (2016).

[27] C. Rolin, E. Kang, J. H. Lee, G. Borghs, P. Heremans, and J. Genoe, "Charge carrier mobility in thin films of organic semiconductors by the gated van der Pauw method", Nature Communications **8**, 1 (2017).

[28] H. Sirringhaus, "25th anniversary article: Organic field-effect transistors: The path beyond amorphous silicon", Advanced Materials **26**, 1319 (2014).

[29] X. Gao and Z. Zhao, "High mobility organic semiconductors for field-effect transistors", Science China Chemistry **58**, 947 (2015).

[30] S. Galindo, A. Tamayo, F. Leonardi, and M. Mas-Torrent, "Control of Polymorphism and Morphology in Solution Sheared Organic Field-Effect Transistors", Advanced Functional Materials **27**, 1 (2017).

[31] B. Wu, Z. Wu, Q. Yang, F. Zhu, T. W. Ng, C. S. Lee, S. H. Cheung, and S. K. So, "Improvement of Charge Collection and Performance Reproducibility in Inverted Organic Solar Cells by Suppression of ZnO Subgap States", ACS Applied Materials and Interfaces **8**, 14717 (2016).

[32] J. C. Blakesley, F. A. Castro, W. Kylberg, G. F. A. Dibb, C. Arantes, R. Valaski, M. Cremona, J. S. Kim, and J. S. Kim, "Towards reliable charge-mobility benchmark measurements for organic semiconductors", Organic Electronics: physics, materials, applications **15**, 1263 (2014).

[33] R. H. Baughman and L. W. Shacklette, "Conductivity as a function of conjugation length: theory and experiment for conducting polymer complexes", Phys. Rev. B **39**, 5872 (1989).

[34] Y.-K. Lan, C. H. Yang, and H.-C. Yang, "Theoretical investigations of electronic structure and charge transport properties in polythiophene-based organic field-effect transistors", Polymer International **59**, 16 (2010).

[35] B. O'Connor, R. J. Kline, B. R. Conrad, L. J. Richter, D. Gundlach, M. F. Toney, and D. M. DeLongchamp, "Anisotropic structure and charge transport in highly strain-aligned regioregular poly(3-hexylthiophene)", Advanced Functional Materials **21**, 3697 (2011).

[36] V. Skrypnychuk, G. J. A. Wetzelaer, P. I. Gordiichuk, S. C. Mannsfeld, A. Herrmann, M. F. Toney, and D. R. Barbero, "Ultrahigh Mobility in an Organic Semiconductor by Vertical Chain Alignment", Advanced Materials **28**, 2359 (2016).

[37] P. Prins, F. C. Grozema, J. M. Schins, S. Patil, U. Scherf, and L. D. A. Siebbeles, "High intrachain hole mobility on molecular wires of ladder-type poly(p-phenylenes)", Physical Review Letters **96**, 1 (2006).

[38] A. Kokil, K. Yang, and J. Kumar, "Techniques for characterization of charge carrier mobility in organic semiconductors", Journal of Polymer Science, Part B: Polymer Physics **50**, 1130 (2012).

[39] Z. B. Wang, M. G. Helander, M. T. Greiner, J. Qiu, and Z. H. Lu, "Analysis of charge-injection characteristics at electrode-organic interfaces: Case study of transition-metal oxides", Physical Review B - Condensed Matter and Materials Physics **80**, 1 (2009).

[40] "Charge injection and recombination at the metal-organic interface", Chemical Physics Letters **299**, 115 (1999).

[41] M. Bokdam, D. Akr, and G. Brocks, "Fermi level pinning by integer charge transfer at electrode-organic semiconductor interfaces", Applied Physics Letters **98**, 2009 (2011).

[42] M. Oehzelt, N. Koch, and G. Heimel, "Organic semiconductor density of states controls the energy level alignment at electrode interfaces", Nature Communications **5**, 1 (2014).

[43] A. Crispin, X. Crispin, M. Fahlman, M. Berggren, and W. R. Salaneck, "Transition between energy level alignment regimes at a low band gap polymer-electrode interfaces", Applied Physics Letters **89** (2006) 10.1063/1.2396899.

[44] H. Vazquez, F. Flores, and A. Kahn, "Induced Density of States model for weakly-interacting organic semiconductor interfaces", Organic Electronics **8**, Coupled States of Excitons, Photons, and Plasmons in Organic Structures, 241 (2007).

[45] Q. Bao, O. Sandberg, D. Dagnelund, S. Sand??n, S. Braun, H. Aarnio, X. Liu, W. M. Chen, R. ??sterbacka, and M. Fahlman, "Trap-Assisted recombination via integer charge transfer states in organic bulk heterojunction photovoltaics", Advanced Functional Materials **24**, 6309 (2014).

[46] R. L. McCreery and A. J. Bergren, "Progress with molecular electronic junctions: Meeting experimental challenges in design and fabrication", Advanced Materials **21**, 4303 (2009).

[47] A. Vilan, D. Aswal, and D. Cahen, "Large-Area, Ensemble Molecular Electronics: Motivation and Challenges", Chemical Reviews **117**, 4248 (2017).

[48] D. Xiang, X. Wang, C. Jia, T. Lee, and X. Guo, "Molecular-Scale Electronics: From Concept to Function", Chemical Reviews **116**, 4318 (2016).

[49] M. Ratner, Nature Nanotechnology ().

[50] J. Simmons, "Generalized Formula for the Electric Tunnel Effect between Similar Electrodes Separated by a Thin Insulating Film", Journal of Applied Physics **34**, 1793 (1963).

[51] L. Luo, S. H. Choi, and C. D. Frisbie, "Probing hopping conduction in conjugated molecular wires connected to metal electrodes", Chemistry of Materials **23**, 631 (2011).

[52] D. J. Wold and C. D. Frisbie, "Fabrication and Characterization of Metal - Molecule - Metal Junctions by Conducting Probe Atomic Force Microscopy", J Am Chem Soc **123**, 5549 (2001).

[53] L. Luo and C. D. Frisbie, "Length-dependent conductance of conjugated molecular wires synthesized by stepwise "click" chemistry", Journal of the American Chemical Society **132**, 8854 (2010).

[54] I. A. VonWald, M. M. Moog, T. W. LaJoie, J. D. Yablonski, D. M. DeLongchamp, J. Locklin, F. Tsui, and W. You, "Morphology, Structure, and Enhanced Intramolecular Conduction in Ultralong Conjugated Polymer Brushes", The Journal of Physical Chemistry C, acs.jpcc.8b00033 (2018).

[55] A. Halperin, M. Tirrell, and T. P. Lodge, "Tethered chains in polymer microstructures", in *Macromolecules: synthesis, order and advanced properties* (Springer Berlin Heidelberg, Berlin, Heidelberg, 1992), pp. 31–71.

[56] G. Odian, "Principles of polymerization. 4th edition", in (John Wiley and Sons Inc.: Hoboken, 2004).

[57] T. W. LaJoie, "Conjugated Polymer Brushes as Molecular Wires in Electronic Devices: Synthesis, Device Design, and Characterization. Ph. D. Dissertation", (2015).

[58] H. Komber, V. Senkovskyy, R. Tkachov, K. Johnson, A. Kiriy, W. T. S. Huck, and M. Sommer, "Ring Walking versus Trapping of Nickel(0) during Kumada Catalyst Transfer Polycondensation Using Externally Initiated Electron-Accepting Thiophene-Benzothiadiazole-Thiophene Precursors", Macromolecules **44**, 9164 (2011).

[59] Z. J. Bryan and A. J. McNeil, "Conjugated polymer synthesis via catalyst-transfer polycondensation (CTP): Mechanism, scope, and applications", Macromolecules **46**, 8395 (2013).

[60] N. Doubina, J. L. Jenkins, S. A. Paniagua, K. A. Mazzio, G. A. MacDonald, A. K.-Y. Jen, N. R. Armstrong, S. R. Marder, and C. K. Luscombe, "Surface-Initiated Synthesis of Poly(3-methylthiophene) from Indium Tin Oxide and its Electrochemical Properties", Langmuir **28**, 1900 (2012).

[61] H. N. Eric, S. S. Kyle, B. J. A., S. G. R., and L. Jason, "Palladium-Mediated Surface-Initiated Kumada Catalyst Polycondensation: A Facile Route Towards Oriented Conjugated Polymers", Macromolecular Rapid Communications **33**, 2115.

[62] N. Marshall, S. K. Sontag, and J. Locklin, "Surface-initiated polymerization of conjugated polymers", Chem. Commun. **47**, 5681 (2011).

[63] S. K. Sontag, G. R. Sheppard, N. M. Usselman, N. Marshall, and J. Locklin, "Surface-Confined Nickel Mediated Cross-Coupling Reactions: Characterization of Initiator Environment in Kumada Catalyst-Transfer Polycondensation", Langmuir **27**, 12033 (2011).

[64] A. Roy, T. L. Bougher, R. Geng, Y. Ke, J. Locklin, and B. A. Cola, "Thermal conductance of poly(3-methylthiophene) brushes", ACS Applied Materials & Interfaces **8**, 25578 (2016).

[65] A. T. Kleinschmidt, S. E. Root, and D. J. Lipomi, "Poly(3-hexylthiophene) (p3ht): fruit fly or outlier in organic solar cell research?", J. Mater. Chem. A **5**, 11396 (2017).

[66] *Tethered chains in polymer microstructures* (CRC Press, Boca Raton, FL, 2007), pp. 31–71.

[67] R. Elsenbaumer, K. Jen, and R. Oboodi, "Processible and environmentally stable conducting polymers", Synthetic Metals **15**, Proceedings of the Workshop on Conductive Polymers, 169 (1986).

[68] N. Marshall, S. K. Sontag, and J. Locklin, "Substituted Poly(p-phenylene) Thin Films via Surface-Initiated Kumada-Type Catalyst Transfer Polycondensation", Macromolecules **43**, 2137 (2010).

[69] N. Elgrishi, K. J. Rountree, B. D. McCarthy, E. S. Rountree, T. T. Eisenhart, and J. L. Dempsey, "A Practical Beginner's Guide to Cyclic Voltammetry", Journal of Chemical Education **95**, 197 (2018).

[70] M. Urien, G. Wantz, E. Cloutet, L. Hirsch, P. Tardy, L. Vignau, H. Cramail, and J. P. Parneix, "Field-effect transistors based on poly(3-hexylthiophene): Effect of impurities", Organic Electronics: physics, materials, applications **8**, 727 (2007).

[71] L. S. Wielunski, S. Katalinic, B. Lee, M. Connors, E. Garfunkel, L. C. Feldman, and V. Podzorov, "Ion-scattering analysis of self-assembled monolayers of silanes on organic semiconductors", Nuclear Instruments and Methods in Physics Research, Section B: Beam Interactions with Materials and Atoms **268**, 1889 (2010).

[72] M. M. Erwin, J. McBride, A. V. Kadavanich, and S. J. Rosenthal, "Effects of impurities on the optical properties of poly-3-hexylthiophene thin films", Thin Solid Films **409**, 198 (2002).

[73] M. Mayer, "SIMNRA, a simulation program for the analysis of NRA, RBS and ERDA", AIP Conference Proceedings **541**, 541 (1999).

[74] M. M. Ling and Z. Bao, "Thin film deposition, patterning, and printing in organic thin film transistors", Chemistry of Materials **16**, 4824 (2004).

[75] C. Liu, Y. Xu, and Y. Y. Noh, "Contact engineering in organic field-effect transistors", Materials Today **18**, 79 (2015).

[76] Y. Olivier, D. Niedzialek, V. Lemaur, W. Pisula, K. Mullen, U. Koldemir, J. R. Reynolds, R. Lazzaroni, J. Cornil, and D. Beljonne, "25th anniversary article: High-mobility hole and electron transport conjugated polymers: How structure defines function", Advanced Materials **26**, 2119 (2014).

[77] T. Yamamoto, D. Komarudin, M. Arai, B. L. Lee, H. Suganuma, N. Asakawa, Y. Inoue, K. Kubota, S. Sasaki, T. Fukuda, and H. Matsuda, "Extensive studies on pi-stacking of poly(3-alkylthiophene-2,5-diyl)s and poly(4-alkylthiazole-2,5-diyl)s by optical spectroscopy, NMR analysis, light scattering analysis, and X-ray crystallography", Journal of the American Chemical Society **120**, 2047 (1998).

[78] I. Jan, "Nika: software for two-dimensional data reduction", Journal of Applied Crystallography **45**, 324 (2012).

[79] S. K. Sinha, E. B. Sirota, S. Garoff, and H. B. Stanley, "X-ray and neutron scattering from rough surfaces", Phys. Rev. B **38**, 2297 (1988).

[80] V. W. Stone, A. M. Jonas, B. Nysten, and R. Legras, "Roughness of free surfaces of bulk amorphous polymers as studied by x-ray surface scattering and atomic force microscopy", Phys. Rev. B **60**, 5883 (1999).

[81] R. Lin, M. Galili, U. J. Quaade, M. Brandbyge, T. Bjornholm, A. Esposti, F. Biscarini, and K. Stokbro, "Spontaneous dissociation of a conjugated molecule on the Si(100) surface", **117**, 321 (2002).

[82] M. C. Gurau, D. M. Delongchamp, B. M. Vogel, E. K. Lin, D. A. Fischer, S. Sambasivan, and L. J. Richter, "Measuring molecular order in poly(3-alkylthiophene) thin films with polarizing spectroscopies", Langmuir **23**, 834 (2007).

[83] J. Krim and J. O. Indekeu, "Roughness exponents: a paradox resolved", Phys. Rev. E **48**, 1576 (1993).

[84] M. A. Meitl, Z. T. Zhu, V. Kumar, K. J. Lee, X. Feng, Y. Y. Huang, I. Adesida, R. G. Nuzzo, and J. A. Rogers, "Transfer printing by kinetic control of adhesion to an elastomeric stamp", Nature Materials **5**, 33 (2006).

[85] S. Ho Choi, B. Kim, and C. D. Frisbie, "Electrical resistance of long conjugated molecular wires.", Science (New York, N.Y.) **320** (2008) 10.1126/science.1156538.

[86] F. C. Simeone, H. J. Yoon, M. M. Thuo, J. R. Barber, B. Smith, and G. M. Whitesides, "Defining the value of injection current and effective electrical contact area for egain-based molecular tunneling junctions", Journal of the American Chemical Society **135**, 18131 (2013).

[87] H. Jeong, D. Kim, D. Xiang, and T. Lee, "High-Yield Functional Molecular Electronic Devices", ACS Nano **11**, 6511 (2017).

[88] L. Merces, R. F. De Oliveira, D. H. S. De Camargo, and C. C. B. Bufon, "Long-Range Coherent Tunneling in Physisorbed Molecular Ensembles", Journal of Physical Chemistry C **121**, 16673 (2017).

[89] J. R. Niskala and W. You, "Metal-molecule-metal junctions via PFPE assisted nanotransfer printing (nTP) onto self-assembled monolayers", Journal of the American Chemical Society **131**, 13202 (2009).

[90] J. R. Niskala, W. C. Rice, R. C. Bruce, T. J. Merkel, F. Tsui, and W. You, "Tunneling characteristics of Au-alkanedithiol-Au junctions formed via nanotransfer printing (nTP)", Journal of the American Chemical Society **134**, 12072 (2012).

[91] A. A. Volinsky, N. R. Moody, and W. W. Gerberich, "Nanoindentation of Au and Pt/Cu thin films at elevated temperatures", Journal of Materials Research **19**, 2650 (2004).

[92] O. Awartani, B. I. Lemanski, H. W. Ro, L. J. Richter, D. M. De Longchamp, and B. T. OConnor, "Correlating stiffness, ductility, and morphology of polymer Fullerene films for solar cell applications", Advanced Energy Materials **3**, 399 (2013).

[93] A. N. Caruso, D. Q. Feng, Y. B. Losovyj, D. L. Schulz, S. Balaz, L. G. Rosa, A. Sokolov, B. Doudin, and P. A. Dowben, "Defect contributions to conductivity in poly(3-hexylthiophene)?", Physica Status Solidi (B) Basic Research **243**, 1321 (2006).

[94] F. S. Kim and S. A. Jenekhe, "Charge transport in poly(3-butylthiophene) nanowires and their nanocomposites with an insulating polymer", Macromolecules **45**, 7514 (2012).

[95] B. Ecker, J. C. Nolasco, J. Pallares, L. F. Marsal, J. Posdorfer, J. Parisi, and E. Von Hauff, "Degradation effects related to the hole transport layer in organic solar cells", Advanced Functional Materials **21**, 2705 (2011).

[96] C. E. Smith, S. O. Odoh, S. Ghosh, L. Gagliardi, C. J. Cramer, and C. D. Frisbie, "Length-Dependent Nanotransport and Charge Hopping Bottlenecks in Long Thiophene-Containing pi-Conjugated Molecular Wires", Journal of the American Chemical Society **137**, 15732 (2015).

[97] L. Lafferentz, F. Ample, H. Yu, S. Hecht, C. Joachim, and L. Grill, "Conductance of a single conjugated polymer as a continuous function of its length", Science **323**, 1193 (2009).

[98] R. Geng, "Spin Injection and Spin Transport in Organic Spin Valves",

[99] I. VonWald, Personal Communication, May 1, 2018.

[100] S. Braun, W. Osikowicz, Y. Wang, and W. R. Salaneck, "Energy level alignment regimes at hybrid organic-organic and inorganic-organic interfaces", Organic Electronics **8**, 14 (2007).